



Graffiti of a zeolite (Photo taken from Mineralogisch-Petrologisches Institut und Museum der Universität Bonn, Poppelsdorfer Schloß, D-53115 Bonn).

Theoretical Investigation of Static and Dynamic Properties of Zeolite ZSM-5 Based Amorphous Material

Inauguraldissertation zur Erlangung des Doktorgrades
der Mathematisch-Naturwissenschaftlichen Fakultät
der Universität zu Köln

vorgelegt von
Atashi Basu Mukhopadhyay
aus Kanchrapara

Köln 2004

Berichterstatter: Prof. Dr. M. Dolg
Prof. Dr. U. K. Deiters
Tag der mündlichen Prüfung: 13.07.04

Acknowledgments

This thesis is the result of three years of work whereby I have been supported by many people. It is a pleasant aspect that I have now the opportunity to express my gratitude for all of them.

The first person I would like to thank is my direct supervisor Prof. Dr. Michael Dolg. His overly enthusiasm and integral view on research has made a deep impression on me. I owe him lots of gratitude for being an excellent supervisor and a good friend.

I would like to thank my other supervisor Prof. Dr. Christina Oligschleger who kept an eye on the progress of my work. I would like to thank Christa, for our many discussions and providing me with suggestions and tips that helped me a lot in staying at the right track.

I would also like to thank the other members of my PhD committee Prof. Dr. U. K. Deiters and Prof. Dr. U. Ruschewitz who took effort in reading and providing me with valuable comments on this thesis.

I am grateful to Deutsche Forschungsgemeinschaft for financial support through SFB 408. I thank the Forschungszentrum Jülich for generous grant of computer time on CRAY T3E systems (Project No. k2710000).

I acknowledge the theoretical chemistry group at Köln for contribution to the development of this work. Dr. Michael Hanrath helped me with the library routines for my programs. His lectures and discussions on advanced quantum-chemical topics were quite informative. Dr. Johannes Weber and Frau Birgitt Börsch-Pulm helped me with the computers. Dr. Xiaoyan Cao gave a lot of suggestions which helped me to adjust to the new environment when I came from India. I would like to thank my other colleagues, i.e., Mr. Martin Böhler, Ms. Rebecca Fondermann, Mr. Sombat Kettrat, Mr. Joachim Friedrich, Mr. Jun Yang, Mr. Marc Burkatzki and Mr. Alexander Schnurpfeil for providing friendly atmosphere in office.

I would like thank people at theoretical chemistry group, Bonn and specially for giving me my favorite room as my office (facing towards east and with lots of sunshine) where I had completed around 80% of my doctoral work before moving to Köln. I would like to thank Prof. Dr. S. D. Peyerimhoff for providing intellectually stimulating atmosphere. Many thanks to Mr. Jens Meikelburger for being patient with me and sorting out all computer related problems. I would like to thank Dr. Bernd Nestmann and Prof. Dr. Miljenko Peric for being wonderful friends. Special thanks to my other colleagues, i.e., Frau Claudia Kronz, Dr. Jan Franz, Mr. Werner Reckien, Dr. Thomas Beyer, Dr. Boris Schäfer-Bung, Dr. Vincent Brems and Mr. Jan Haubrich for making me feel at home at the institute. I would also like to thank my other colleagues at FH Rhein-Sieg, Rheinbach.

Apart from work, special thanks to many of my friends at Bonn and NCL, Pune. I also want to say thank-you to my parents and my brother for their understanding and faith in me. Thanks to my in-laws for their support.

Last, but not the least, I would like to thank my husband Kausik for love, patience and encouragement. Without your letters, mails and phone-calls I could not have survived these three and a half years away from you.

My Family

Contents

1	Introduction	1
1.1	Amorphous Materials	2
1.2	Amorphous Materials Derived From Zeolite	4
1.2.1	Zeolites	4
1.2.2	Zeolite-based amorphous materials	5
1.3	About this Work	6
I	Theoretical Background	9
2	Classical Molecular Dynamics	11
2.1	From the Schrödinger Equation to Classical Molecular Dynamics	11
2.2	Equations of Motion	14
2.2.1	Lagrange equations of motion	14
2.2.2	Hamilton equations of motion	15
2.3	General Procedure for Molecular Dynamics	15
2.4	Interaction Potential	16
2.4.1	Short-range potential	17
2.4.2	Long-range potential	20
2.5	Integrators	21
2.5.1	Verlet integrator	22
2.5.2	Leap Frog integrator	23
2.5.3	Velocity Verlet integrator	24
2.6	Simulations in Different Ensembles	24
2.6.1	Sampling from an ensemble	24
2.6.2	Common statistical ensembles	25
2.6.3	Molecular dynamics at constant temperature	27
2.6.4	Molecular dynamics at constant pressure	30
2.7	Periodic Boundary Conditions	32

3	Large-Scale Optimization	35
3.1	Basic Approach to Large-Scale Optimization	35
3.2	Basic Descent Structure of Local Methods	37
3.3	Nonderivative Methods	38
3.4	Gradient Methods	38
3.4.1	Steepest descent method	38
3.4.2	Conjugate gradient method	40
3.4.3	Newton-Raphson method	42
4	Solid State Properties	45
4.1	Structural Properties	45
4.1.1	Diffraction by crystals	45
4.1.2	Investigation of structures of non-crystalline solids	47
4.2	Vibrational Properties	49
4.2.1	Phonons	49
4.2.2	Properties under harmonic approximation	51
4.2.3	Anomalies in amorphous systems	53
4.3	Elastic Constants	54
4.3.1	Elastic strains and stresses	55
4.3.2	Stress components	56
4.3.3	Elastic compliance and stiffness constants	56
5	Quantum Chemical Treatment of Solids	59
5.1	Overview of Quantum Chemical Methods	59
5.1.1	The Hartree-Fock method	59
5.1.2	Electron correlation methods	60
5.1.3	Density functional theory	64
5.2	Ab Initio Treatment of Periodic System	66
5.2.1	The finite-cluster approaches	66
5.2.2	Bloch-orbital-based approach	68
5.2.3	Wannier-orbital-based approach	69
II	Applications	73
6	Structural Properties	75
6.1	Computational Details	75
6.1.1	Interaction potential	75
6.1.2	Preparation of amorphous configurations	76
6.2	Short-Range Order	78
6.3	Connectivity of the Elementary Units	79
6.4	Extent of Amorphization	86

6.4.1	Defect in coordination number	86
6.4.2	Internal surface area	89
6.4.3	Ring analysis	92
7	Vibrational Properties	97
7.1	Vibrational Density of States	97
7.2	Analysis of the Vibrational Modes	101
7.2.1	Element specific motion with respect to bonds	101
7.2.2	Relative contribution of motions of structural subunits to DOS	102
7.2.3	Mode localization	108
7.2.4	Phase quotient	110
7.3	Effect of Extent of Amorphization on Vibrational DOS	111
7.4	Low-Frequency Vibrational Excitations	113
8	Relaxation Properties	121
8.1	Time Evolution on the Energy Landscape	123
8.2	Structure and Mode of Relaxations	123
8.3	Correlation between Jumps	128
8.4	Heterogeneity	129
9	Two-Fold Rings in Silicates	133
9.1	Applied Methods and Technical Details	135
9.1.1	Finite-Cluster approach/A simple approach	136
9.1.2	Incremental approach	136
9.2	Structure and Stability of Two-Fold Ring	137
10	Summary and Outlook	145
	References	149
	Abstract	161
	Kurzzusammenfassung	163
	List of Publications	165
	Lebenslauf	167
	Erklärung	169

List of Figures

1.1	P, T diagram of ordered and disordered states of a typical pure compound.	2
1.2	Path of formation of vitreous and amorphous solids.	3
2.1	Flow chart of a MD program.	15
3.1	The method of steepest descent.	39
3.2	The method of conjugate directions.	41
4.1	The Brillouin zones for a two-dimensional square lattice.	49
4.2	Phonon dispersion relation.	51
6.1	Zeolite ZSM-5 viewed along y-axis.	77
6.2	Total and pair-distribution function.	82
6.3	Bond angle distribution.	83
6.4	Model for the connectivity of tetrahedra.	84
6.5	Cross section of ZSM-5 (crystalline) and its amorphous derivatives.	87
6.6	Distribution of coordination numbers of O and Si atoms.	88
6.7	Internal surface area vs. percentage of energy crystallinity.	90
6.8	Distribution of ringsize.	93
7.1	Vibrational density of states of zeolite-based amorphous structure.	99
7.2	Averaged element specific-contribution to the total vibrational DOS.	101
7.3	The specific heat versus the temperature.	102
7.4	Distribution of element-specific weighted-average angles between the atomic displacement eigenvectors and the bonds.	105
7.5	The total and partial vibrational DOS obtained by the projection of the relative atomic displacements onto the vibrational vectors of the Si-O-Si and SiO ₄ subunits.	107
7.6	Participation ratios of the crystalline and amorphous systems.	109
7.7	Radius of gyration versus frequency	110
7.8	Weighted phase quotient verses frequency.	111
7.9	Vibrational DOS for different PEC versus frequency.	112

7.10	Reduced DOS and maximum of Reduced DOS for ZSM-5-based partially amorphous structures.	114
7.11	Phonon dispersion curves for the silicious ZSM-5.	115
7.12	The active atoms of the modes of BP region.	118
7.13	Participation ratios of modes in BP region.	119
8.1	Element-specific diffusion constants.	122
8.2	Changes in the potential energy and displacement per atom during aging.	124
8.3	Participation ratios against jump distance at different temperatures.	125
8.4	The dimensions of the jumps.	126
8.5	The distribution of correlations between the successive jumps at different temperature.	128
8.6	Element-specific plot of the van Hove correlation functions.	130
8.7	The non-Gaussianity parameter for Si and O.	131
9.1	Model of W-silica.	134
9.2	Variation in the potential energy surface with respect to the area of <i>a-b</i> plane.	135
9.3	Convergence of the cohesive energy per Si ₂ O ₄ unit of W-silica.	138
9.4	Convergence of the lattice parameter and Si-O distance of W-silica.	140
9.5	Finite clusters of a chain of W-silica and α -quartz.	141

List of Tables

6.1	Force-field parameters for BKS potential.	76
6.2	Bond distances and bond angles for the bridged unit in edge-shared SiO ₄ tetrahedra.	85
6.3	Atomic/ionic radii for O and Si depending on the coordination number.	89
6.4	Ring analysis for ZSM-5 based amorphous material.	94
7.1	Vibrational vectors for Si-O-Si subunits assuming O at rest.	103
7.2	Vibrational vectors for SiO ₄ subunits assuming Si at rest.	104
7.3	Partial contributions of the eigenmodes of the Si-O-Si and SiO ₄ subunits.	108
7.4	Ring analysis, degree of puckering and participation ratios of modes for ZSM-5 based amorphous material.	116
7.5	Distribution of the CNs for the 10 % most active atoms in BP region.	117
7.6	Contributions of the vibrational motions exhibited by the active subunit.	120
8.1	The average dimensionalities and average radii of gyration.	126
8.2	Relaxation with respect to bond changes.	127
8.3	Contributions of the relaxations exhibited by Si-O-Si and SiO ₄ subunits by the projectional analysis.	127
9.1	Geometries of two-membered rings in W-silica.	139
9.2	Increments to the correlation energy per unit cell.	142
9.3	Cohesive energies per SiO ₂ unit in α -quartz.	142
9.4	Relative energy of a Si ₂ O ₄ unit with respect to α -quartz.	143

Abbreviations

AO	Atomic Orbital
a.u.	Atomic Unit
BF	Bloch Function
BKS	Beest, Kramer and van Santen
BP	Boson Peak
BZ	Brillouin Zone
CC	Coupled Cluster
CCSD	Coupled Cluster with Single and Double excitations
CI	Configuration Interaction
CISD	Configuration Interaction truncated to Singles and Doubles substitution
CN	Coordination Number
CO	Crystal Orbitals
DFT	Density Functional Theory
DOS	Density of States
FCI	Full Configuration Interaction
fs	Femtosecond
GGA	Generalized Gradient Approximation
GTF	Gaussian Type Function
FWHM	Full Width at the Half Maximum
HF	Hartree-Fock
IR	Infrared
ISA	Internal Surface Area
KS	Kohn-Sham
LDA	Local Density Approximation
MC	Monte Carlo
MD	Molecular Dynamics
MP	Møller-Plesset
NGP	Non-Gaussianity Parameter
ns	Nanosecond
PBC	Periodic Boundary Condition
PEC	Percentage of Energy Crystallinity
ps	Picosecond

QM/MM	Quantum Mechanics and Molecular Mechanics
RDF	Radial Distribution Function
RSPT	Rayleigh-Schrödinger Perturbation Theory
TDSCF	Time-Dependent Self-Consistent Field
THz	Terra Hertz
SCF	Self-Consistent-Field
SDCG	Steepest-Descent-Conjugate-Gradient
XRD	X-Ray Diffractogram

Chapter 1

Introduction

“Amorphous material *per se*, are not new: the iron-rich silicious glassy materials recovered from the moon by the Apollo missions are some billions of years old, and man has been manufacturing glassy materials for thousands of years. What is new, however is the *scientific study* of amorphous materials and there has been an explosion of interest recently as more new materials produced in an amorphous form, some of which have considerable technological promise.”

S. R. Elliott, *Physics of Amorphous Materials* (1984).

1.1 Amorphous Materials

"Amorphous" meaning "structureless" describes all those states of matter whose properties do not show a preferential direction unlike crystals. The range of disordered structures is far wider than that of crystalline phases, as seen from Fig. 1.1 (representing a phase diagram of a typical pure compound). By increasing pressure and temperature under conditions which sufficiently delay spontaneous transition into the crystalline state, amorphous solids can be continuously transformed into melts, and the latter can further be transformed into the gaseous state if the critical temperature is exceeded. It is not possible, however to change from the ordered crystalline phase to one of the disordered states of aggregation without provoking discontinuous variation of certain variables of state, such as volume, enthalpy or entropy.

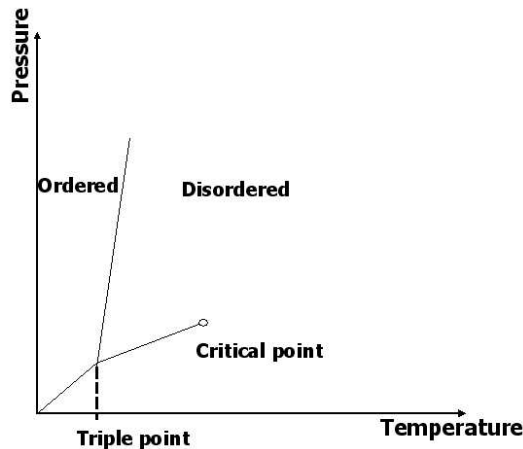


Figure 1.1: P, T diagram of ordered and disordered state of a typical pure compound (Adapted from Ref. [2]).

The methods of X-ray, neutron and electron diffraction are helpful in distinguishing the amorphous substances from those that are crystalline. Instead of the distinct discrete diffraction maxima occurring for crystalline substances, only a few circular fringes are observed in amorphous solids. These circular fringes indicate a non-random distribution of interatomic distances, in other words, a degree of order that has been carried over to the amorphous state. Hence, amorphous substances, like crystals, are usually characterized by certain areas of *short-range order*. These often correspond to the structural units of crystalline states, or at least are associated with them through a clear relationship in terms of chemical structure. As distance increases, the diversity of structural configurations also increases rapidly owing to a certain variability in bond lengths, and especially in bond angles mainly due to the twisting of units relative to each other, through partial rotation about the axes of chemical bonds. Hence, a *long-range order*, as in crystals, does not exist in amorphous substances.

The world of *quasi-crystalline* solids occupies a position between crystalline and amorphous matter. These materials seem to represent a fundamentally different phase of solids, exhibiting symmetries that are impossible for ordinary solids. They exhibit the long-range orientational order rather than the translational one. This quasi-periodicity leads to well-defined X-ray diffraction pattern.

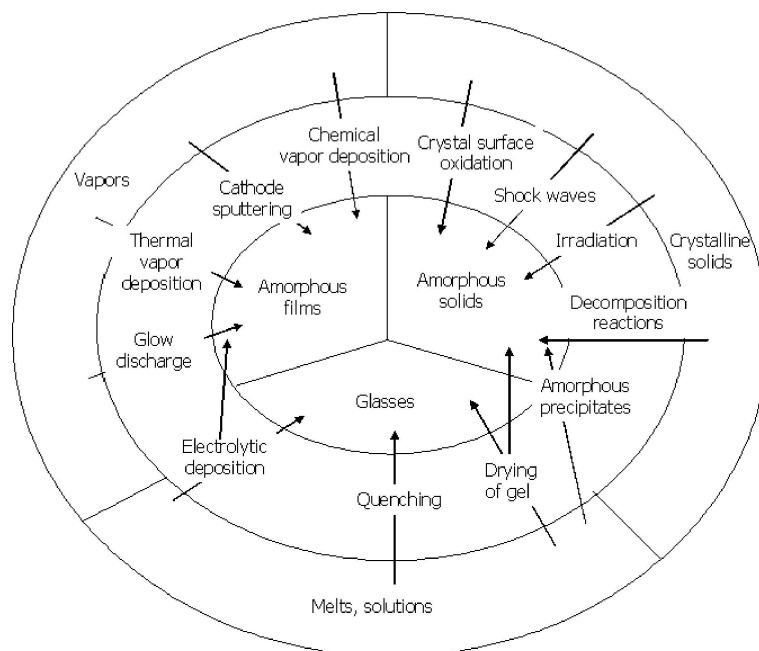


Figure 1.2: Path of formation of vitreous and amorphous solids from melts or solution, vapors and crystalline states of substances (Adapted from Ref. [2]).

Amorphous solids can be obtained from the liquid state, i.e., from a melt or solution, or from the gas phase, provided that the formation of a periodic arrangement of units through the process of nucleation and crystallization is prevented. On the other hand, by supplying energy to crystalline solids they can be converted to the amorphous state directly without passing through the liquid or gaseous phases. A collection of the methods are summarized in Fig. 1.2. Refer to Ref. [1, 2] for further details. Glasses, a special class of non-crystalline solids, are obtained by sufficiently rapid quenching of melts [3, 4, 5] or by drying of gels from solutions [6]. The process of precipitation of solutions often leads to amorphous precipitates [7]. Electrolytic separation using a high current density also gives rise to the formation of amorphous layers [8]. With regards to the methods starting from the gaseous phase, the most important of these are thermal evaporation and condensation in high vacuum [9], cathode sputtering [10] and deposition of amorphous layers in chemical and glow discharge processes [11]. Amorphous films or layers can also be generated by direct oxidation of crystals at the surface [12]. Crystalline solids are also converted to amorphous solids by the influence

of mechanical treatment [13], shock waves [14] or intense radiation with neutrons or ions [15].

1.2 Amorphous Materials Derived From Zeolite

1.2.1 Zeolites

The word *zeolite* is Greek in origin, coming from the words "zein" and "lithos" meaning to boil and rock. It was first used by the Swedish chemist and mineralogist A. F. Cronstedt in his paper announcing the discovery of a new class of tectosilicates [16]. There was little interest in zeolites until the late 1930's when the modern founder of zeolite chemistry, R. M. Barrer began the characterization of zeolite structure and chemistry [17]. His work gave details of the first method of laboratory synthesis of zeolites from silicate alumina gels, the changes that occur upon ion exchange and their use as environmental friendly, shape selective catalysts. These discoveries sparked huge interest in the synthesis of shape selective zeolite catalysts in companies such as Union Carbide and Mobil.

Chemically, zeolites are microporous solid-state crystalline materials having channels, cages and windows of molecular dimensions. The zeolite framework consists of an infinite array of corner-sharing TO_4 tetrahedra. The tetrahedral atom T can be a wide range of combinations of elements, e.g., Si and Al, B and Si, Ga and Si, etc. In cases where the T atoms cause a charge imbalance in the system, the charge neutrality is maintained by the incorporation of protons or extra-framework cations. The cations usually occupy sites of relatively low coordination number in the structure and as a consequence, are easy to ion-exchange. Although the tetrahedra are quite rigid, there is considerable flexibility in the bond angles about the O atom (bond angle ranges from 125° to close to 180° throughout the many known zeolite structures).

Zeolites are normally synthesized hydrothermally from basic reaction gels at temperatures between 60°C and 200°C under an autogenous pressure. Most of the highly siliceous zeolites are formed in the presence of organic bases known as templates, introduced in the early 1960's [18]. These ranges from simple hydrated cations to complex organic amines and crown ethers.

Due to their unique porous properties, zeolites are used in a variety of applications, with a global market of several million tons per annum. Following lists main applications of zeolites.

(i) *Heterogenous catalysis*: One of the most important applications of zeolites is in the field of industrial catalysis. There are several factors which dictate the catalytic properties of zeolites. Firstly, their large internal surface area (typically $300\text{-}700\text{ m}^2/\text{g}$ or more than 98% of the total surface area) provides a high concentration of active sites, usually the Brønsted acid sites found in protonated zeolites. These are generally located as bridging hydroxyl group. The high thermal stability of many zeolite struc-

tures makes them ideal for use in an industrial environment where many processes operate in conditions of high temperature and pressure. The shape selective properties of zeolites also control the results of many reactions inside the pore, either by allowing reactant or product molecules to selectively diffuse through the channels, or by the stabilization of the transition states.

(ii) *Adsorption and separation*: The shape-selective properties of zeolites are also the basis for their use in molecular adsorption. The ability preferentially to adsorb certain molecules, while excluding others, has opened up a wide range of molecular sieving applications. The size and shape of pores and also chemical nature of diffusing molecules control the access into the zeolite, e.g., as in the purification of *para*-xylene by silicalite. Cation-containing zeolites are extensively used as desiccants due to their high affinity for water. These also find application in gas separation, where molecules are differentiated on the basis of their electrostatic interactions with the metal ions.

(iii) *Ion exchange*: The presence of loosely bound extra-framework cations in the zeolite structure allows efficient ion exchange to occur in aqueous solution. This is exploited in many commercial applications. For example, Na Zeolite-A is used to soften water by exchanging Na^+ from the zeolite with Ca^{2+} in hard water. This is also a major component of concentrated washing powder formulations, where it replaces sodium tripolyphosphate to reduce the environmentally hazardous phosphate concentration. Another important use of zeolites as ion-exchangers has been as radioactive decontaminants. Clinoptilolite, for example, was used extensively after the Chernobyl nuclear disaster to absorb radioactive ions such as ^{90}Sr and ^{137}Cs from the water supply.

1.2.2 Zeolite-based amorphous materials

Zeolites undergo amorphization by mechanical [19, 20], high-pressure [21] and thermal [22] treatments. They also become amorphous when they are exposed to high-radiation doses and electron irradiation [23, 24]. Zeolite-based amorphous materials are also proposed to be important for technological applications.

In order to quantify extent of amorphization, experimentalists use the percentage of X-ray diffractogram (XRD) crystallinity [28] based on the ratio of the major peak intensities of the sample relative to those of a highly crystalline reference material, i.e.,

$$\% \text{ XRD crystallinity} = \frac{\text{sum of peak intensities of sample}}{\text{sum of peak intensities of reference}} \times 100. \quad (1.1)$$

Pore size and shape, Si/Al ratio or other modifications such as extra-framework cation exchange, isomorphous substitution, pore blockage, elimination of external sites etc., are varying parameters for determining the product selectivity of zeolitic catalysis [26]. One of the reactions that has received considerable attention over the last decade is the skeletal isomerization of 1-butene to yield isobutene. The interest in this reaction arises from the fact that the branched alkene can subsequently be reacted

with methanol for the synthesis of methyl-tertiary-butyl ether [27]. It was shown that ZSM-5 and ferrierite-based ZSM-5 materials with XRD crystallinity level as low as 2% exhibited superior catalytic performance (higher selectivities and yields) in this skeletal isomerization reactions compared to their conventional highly crystalline analogue. This was attributed to be a consequence of decreased zeolite pore lengths that are presumably present in these amorphous materials [28]. Another industrially relevant reaction is the conversion of light alkanes into aromatic compounds which offers a useful route into high octane fuels [29, 30]. ZSM-5 type materials have been used for this type of reactions [31]. Recently, Zn and Ga incorporated novel aluminosilicates, comprising ZSM-5-based structures having XRD crystallinities ranging from substantially amorphous (XRD crystallinity lower than 30%) to the partially crystalline (XRD crystallinity between 30% and 70%) and their highly crystalline (XRD crystallinity higher than 70%) ZSM-5 analogues were studied [25]. Experiments show that the optimum activity and the BTX (benzene, toluene and xylenes) selectivity are found for XRD crystallinity in the range 50%-85%.

Reversible cation exchange property is the basis for using zeolites in the selective removal of radionuclides from high-level liquid nuclear waste. Amorphous forms derived from zeolites are proposed to be better back fill material for heavy metals [24]. For example, amorphized zeolite Na-Y loses approximately 95% of its ion exchange capacity for Cs due to loss of exchangeable cation sites and/or blockage of access to exchangeable cation sites. The Cs-exchanged zeolite Na-Y phase has a slightly higher thermal stability than the unexchanged zeolite Na-Y. A desorption study indicated that the amorphization of Cs loaded Na-Y zeolite enhances the retention capacity of exchangeable Cs ions due to closure of structural channels.

1.3 About this Work

This thesis deals with the simulation of amorphous forms derived from zeolite. Experimental studies of mechanical treatment on zeolites show that amorphization causes remarkable changes in vibrational IR spectra and XRDs [19, 20]. This implies that the amorphization process, i.e., the transformation from long-range to short-range ordering of the framework, is caused by structural changes at the molecular level. Thus, studies of structural and dynamic aspects in these amorphous zeolite-based systems and their correlation to microscopic properties presents a fascinating challenge. Hence, understanding the dependence of physical and chemical properties on the microstructure is critical for designing new materials suitable for specific applications.

This work features as one of the projects under Sonderforschungsbereich 408 at the University of Bonn, which deals with the investigation of structure and properties of inorganic amorphous materials. All silica ZSM-5, i.e., *silicalite* was chosen as a model system for the preparation of the amorphous state, since it is experimentally a well studied system. Details of structure of zeolite silicalite (silicious ZSM-5) is presented

in chapter 6 (section 6.1.2). Despite of the significant interest of chemists to investigate the chemical properties of the zeolite ZSM-5-based amorphous materials [28, 25], the investigation of detailed structural and dynamic properties are lacking. To the best of our knowledge this work is the first theoretical investigation on these lines.

The derivation of a detailed microscopic structure of any non-crystalline system represent a big scientific challenge even today. Special experimental techniques need to be employed. Even when such techniques are used, only a limited amount of local structural information is generally obtainable, and the construction of structural models can be a most useful route to a further understanding of the structure, particularly the medium-range order. The absence of translational symmetry and the requirement to treat rather large model clusters cut out from the infinite system makes the study of amorphous materials using the available *ab initio* methods of quantum chemistry and solid state physics a very difficult, if not an unmanageable task. Whereas these approaches rely on the finite or periodic character of the investigated systems, a large number of real systems does not fall into these two categories but rather shows only a partially crystalline or even completely amorphous character. In such cases simulation techniques like molecular dynamics (MD) and Monte Carlo (MC) have become widely used tools to explore complicated amorphous systems. MC methods are applied to explore configuration space, i.e, to search for minimum energy structures and to establish their properties as well as to study relaxation from a global point of view. However, sometimes the move-classes may be unphysical and do not give reliable insight into the microscopic dynamics of the systems. MD is widely used to construct models of the amorphous state by rapid quenching of structures at high temperature and analyzing the dynamics of the model on a microscopic scale. The success of MD depends crucially on the quality of the interaction potentials used to determine the energy and the forces between interacting particles. The advantage of MD over MC is that it gives a route to study dynamic properties of systems.

In this thesis we have studied the structural (chapter 6) and dynamic (vibrations and relaxations, chapter 7 & 8) properties mainly on the basis of MD simulations. Our simulations show presence of small percentage of edge-sharing connectivity of SiO₄ tetrahedra depending on the extent of amorphization. We used wavefunction-based *ab initio* methods for determining stability and structure of these unusual features (chapter 9). We choose W-silica as a model system for edge-sharing tetrahedra silicate system and compared our results with existing theoretical results.

The organization of the thesis is as follows:

- Part I: Theoretical Background → Basics of MD, local-optimization methods, modeling of solid-state and electron-correlation treatment of solid-state as needed in context of this thesis.
- Part II: Applications → Results concerning structural, vibrational and relaxational properties of amorphous form derived from zeolite ZSM-5.

Part I

Theoretical Background

Chapter 2

Classical Molecular Dynamics

2.1 From the Schrödinger Equation to Classical Molecular Dynamics

The dynamical evolution of the wavefunction with time is given by the *time-dependent* Schrödinger equation:

$$i\hbar \frac{\partial}{\partial t} \Phi(\{\mathbf{r}_i\}, \{\mathbf{R}_I\}; t) = H \Phi(\{\mathbf{r}_i\}, \{\mathbf{R}_I\}; t) \quad (2.1)$$

in its position representation with the standard non-relativistic Hamiltonian,

$$H = - \sum_I \frac{\hbar^2}{2M_I} \nabla_I^2 - \sum_i \frac{\hbar^2}{2m_e} \nabla_i^2 + \sum_{i<j} \frac{e^2}{|\mathbf{r}_i - \mathbf{r}_j|} - \sum_{I,i} \frac{e^2 Z_I}{|\mathbf{R}_I - \mathbf{r}_i|} + \sum_{I<J} \frac{e^2 Z_I Z_J}{|\mathbf{R}_I - \mathbf{R}_J|} \quad (2.2a)$$

$$= - \sum_I \frac{\hbar^2}{2M_I} \nabla_I^2 - \sum_i \frac{\hbar^2}{2m_e} \nabla_i^2 + V_{n-e}(\{\mathbf{r}_i\}, \{\mathbf{R}_I\}) \quad (2.2b)$$

$$= - \sum_I \frac{\hbar^2}{2M_I} \nabla_I^2 + H_e(\{\mathbf{r}_i\}, \{\mathbf{R}_I\}) \quad (2.2c)$$

for electronic and nuclear degrees of freedom. The total wave function $\Phi(\{\mathbf{r}_i\}, \{\mathbf{R}_I\}; t)$ depends on \mathbf{R}_I and \mathbf{r}_i , the nuclear and electronic coordinates, respectively. An elegant derivation of the classical molecular dynamics derived by Tully [32,33,34] is presented below. In order to separate the nuclear and electronic contributions to the wavefunction a product ansatz

$$\Phi(\{\mathbf{r}_i\}, \{\mathbf{R}_I\}; t) \approx \Psi(\{\mathbf{r}_i\}; t) \chi(\{\mathbf{R}_I\}; t) \exp \left[\frac{i}{\hbar} \int_{t_0}^t dt' \tilde{E}_e(t') \right] \quad (2.3)$$

is introduced, where the nuclear and the electronic wavefunctions are separately normalized to unity at every instant of time.

Inserting the ansatz Eq. (2.3) into Eq.(2.1) yield (after multiplying from the left by $\langle \Psi |$ and $\langle \chi |$ and imposing $d\langle H \rangle / dt \equiv 0$) the following equations,

$$i\hbar \frac{\partial \Psi}{\partial t} = - \sum_i \frac{\hbar^2}{2m_e} \nabla_i^2 \Psi + \left\{ \int d\mathbf{R} \chi^*(\{\mathbf{R}_I\}; t) V_{n-e}(\{\mathbf{r}_i\}, \{\mathbf{R}_I\}) \chi(\{\mathbf{R}_I\}; t) \right\} \Psi \quad (2.4)$$

$$i\hbar \frac{\partial \chi}{\partial t} = - \sum_I \frac{\hbar^2}{2M_I} \nabla_I^2 \chi + \left\{ \int d\mathbf{r} \Psi^*(\{\mathbf{r}_i\}; t) H_e(\{\mathbf{r}_i\}, \{\mathbf{R}_I\}) \Psi(\{\mathbf{r}_i\}; t) \right\} \chi. \quad (2.5)$$

Eq. (2.4) and Eq. (2.5) are the basic equations of the mean-field time-dependent self-consistent field (TDSCF) method, where the fast moving electrons move in an average field of the slow moving nuclei and *vice versa*.

Following Messiah, the nuclear wavefunction can be factored into amplitude and phase terms,

$$\chi(\{\mathbf{R}_I\}; t) = A(\{\mathbf{R}_I\}; t) \exp[iS(\{\mathbf{R}_I\}; t)/\hbar] \quad (2.6)$$

where A and S are real-valued [35]. Substituting Eq. (2.6) into Eq. (2.5) and separating the real and imaginary parts, the TDSCF equation for nuclei becomes

$$\frac{\partial A}{\partial t} + \sum_I \frac{1}{2M_I} (\nabla_I A)(\nabla_I S) + \sum_I \frac{1}{2M_I} A (\nabla_I S)^2 = 0 \quad (2.7)$$

and

$$\frac{\partial S}{\partial t} + \sum_I \frac{1}{2M_I} (\nabla_I S)^2 + \int d\mathbf{r} \Psi^* H_e \Psi = \hbar^2 \sum_I \frac{1}{2M_I} \frac{\nabla_I A}{A}. \quad (2.8)$$

Eq. (2.7) describes the flow of probability on the potential energy surface determined by the velocity field $\nabla_I S$. For the derivation of classical molecular dynamics consider Eq. (2.8). In the classical limit this becomes

$$\frac{\partial S}{\partial t} + \sum_I \frac{1}{2M_I} (\nabla_I S)^2 + \int d\mathbf{r} \Psi^* H_e \Psi = 0. \quad (2.9)$$

Eq. (2.9) is known as quantum Hamilton-Jacobi equation, which is identical to the equation in Hamilton-Jacobi formulation of classical mechanics [35, 36]

$$\frac{\partial S}{\partial t} + H(\{\mathbf{R}_I\}, \{\nabla_I S\}) = 0 \quad (2.10)$$

with the classical Hamilton function

$$H(\{\mathbf{R}_I\}, \{\mathbf{P}_I\}) = T(\{\mathbf{P}_I\}) + V(\{\mathbf{R}_I\}) \quad (2.11)$$

defined in terms of generalized coordinates $\{\mathbf{R}_I\}$ and their conjugate momenta $\{\mathbf{P}_I\}$. T and V refer to the classical kinetic energy and the potential energy, respectively. $S(t)$ is the 'classical action', i.e., $S(t) = \int^t L(t')dt'$ and

$$\mathbf{P}_I \equiv \nabla_I S, \quad (2.12)$$

where $L(t')$ is the classical Lagrangian. Considering the Newtonian equation of motion $\dot{\mathbf{P}}_I = -\nabla_I V(\{\mathbf{R}_I\})$, the Eq. (2.9) becomes

$$\frac{d\mathbf{P}_I}{dt} = -\nabla_I \int d\mathbf{r} \Psi^* H_e \Psi \quad (2.13)$$

or

$$M_I \ddot{\mathbf{R}}_I(t) = -\nabla_I \int d\mathbf{r} \Psi^* H_e \Psi \quad (2.14)$$

$$= -\nabla_I V_e^E(\{\mathbf{R}_I(t)\}). \quad (2.15)$$

Thus the nuclei move according to the classical mechanics in an effective potential V_e^E due to electrons and its motion is a function of only the nuclear positions at time t .

However the nuclear wavefunction still occurs in the TDSCF equation for the electronic degrees of freedom. In the classical limit Eq. (2.4) becomes a time-dependent wave function for the electrons

$$i\hbar \frac{\partial \Psi}{\partial t} = -\sum_i \frac{\hbar^2}{2m_e} \nabla_i^2 \Psi + V_{n-e}(\{\mathbf{r}_i\}, \{\mathbf{R}_I\}) \Psi \quad (2.16)$$

$$= H_e(\{\mathbf{r}_i\}, \{\mathbf{R}_I\}) \Psi(\{\mathbf{r}_i\}, \{\mathbf{R}_I\}; t) \quad (2.17)$$

which evolve self-consistently as the classical nuclei are propagated via Eq. (2.14). The approach relying on solving Eq. (2.14) together with Eq. (2.17) is called *Ehrenfest molecular dynamics*.

A further simplification can be invoked by restricting the wavefunction Ψ to be the ground state wavefunction Ψ_0 of H_e at each instant of time. In this limit the nuclei move according to Eq. (2.14) on a Born-Oppenheimer potential energy surface

$$V_e^E = \int d\mathbf{r} \Psi_0^* H_e \Psi_0 \equiv E_0(\{\mathbf{R}_I\}) \quad (2.18)$$

which can be obtained by solving the *time-independent* electronic Schrödinger equation

$$H_e \Psi_0 = E_0 \Psi_0, \quad (2.19)$$

for the ground state only.

To perform classical trajectory calculations on the global potential energy surface, it is conceivable to decouple the task of generating the nuclear dynamics from the task of generating the potential energy surface. In a first step E_0 is computed for many nuclear configurations by solving Eq. (2.19). In a second step, these data points are

fitted to an analytical functional form to yield a global potential energy surface [37], from which analytical gradients can be obtained. In the third step, the Newtonian equation of motion Eq. (2.15) is solved on this surface for many different initial conditions. However, calculation of the global potential energy surface is the limiting step for large systems. There are $3N - 6$ internal degrees of freedom that span the global potential energy surface of an unconstrained N -body system. Using for simplicity 10 discretization points per coordinate implies that of the order of 10^{3N-6} electronic structure calculations are needed. Thus, computational workload increases roughly like $\sim 10^N$ with increasing system size. This is also referred to as the *dimensionality bottleneck* of calculations that rely on global potential energy surfaces [38]. One traditional way out of this dilemma is to approximate the global potential energy surface

$$V_e^E \approx V = V_e^{approx}(\{\mathbf{R}_I\}) = \sum_I^N v_1(\{\mathbf{R}_I\}) + \sum_{I<J}^N v_2(\{\mathbf{R}_I, \mathbf{R}_J\}) + \dots \quad (2.20)$$

in terms of a truncated expansion of many-body contributions [39, 40]. Hence, the electronic degrees of freedom are replaced by the interaction potentials v_n and are not featured as explicit degrees of freedom in the equations of motion. From the above derivation the essential assumption underlying the classical molecular dynamics (MD) become clear: the electrons follow adiabatically the classical nuclear motion and can be integrated out so that the nuclei evolve on single Born-Oppenheimer potential energy surface, which is in general approximated in terms of few-body interactions. For details of above derivation also refer Refs. [41, 42, 43].

2.2 Equations of Motion

Consider system of N particles interacting via a potential V as in Eq. (2.20). While the Newton's second law suffices for the dynamics of the atoms, there exist various other forms to write equations of motion.

2.2.1 Lagrange equations of motion

Consider the Lagrangian function $L(\mathbf{R}, \dot{\mathbf{R}})$ as a function of generalized coordinates and their time derivative with Lagrange equations

$$\frac{d}{dt} \left(\frac{\partial L}{\partial \dot{\mathbf{R}}_I} \right) - \frac{\partial L}{\partial \mathbf{R}_I} = 0, \quad I = 1, \dots, N \quad (2.21)$$

Considering $L = \frac{1}{2} \sum_I M_I \dot{\mathbf{R}}_I^2 - V(\mathbf{R}_I)$, Eq. (2.21) becomes Newtonian equation of motion.

$$M_I \ddot{\mathbf{R}}_I = \mathbf{F}_I, \quad (2.22)$$

$$\text{where } \mathbf{F}_I = \nabla_I L = -\nabla_I V \quad (2.23)$$

is the force on atom I.

2.2.2 Hamilton equations of motion

An alternative formulation of the equations of motion is the Hamilton form. Replacing the generalized velocities $\dot{\mathbf{R}}_I$ in the Lagrange formulation by generalized momenta $\mathbf{P}_I = \partial L / \partial \dot{\mathbf{R}}_I$ and considering the Hamiltonian $H = H(\mathbf{R}, \mathbf{P}, t)$, one obtains equations of motion

$$\dot{\mathbf{R}}_i = \frac{\partial H}{\partial \mathbf{P}_i} \quad (2.24)$$

$$\dot{\mathbf{P}}_i = -\frac{\partial H}{\partial \mathbf{R}_i}, \quad (2.25)$$

where the Hamiltonian is defined as

$$H(\mathbf{R}, \mathbf{P}) = \sum_I \dot{\mathbf{R}}_I \mathbf{P}_I - L(\mathbf{R}, \dot{\mathbf{R}}). \quad (2.26)$$

For Cartesian coordinates, Hamilton equations become

$$\dot{\mathbf{R}}_I = \mathbf{P}_I / M \quad (2.27)$$

$$\dot{\mathbf{P}}_i = -\nabla_I V = \mathbf{F}_I. \quad (2.28)$$

If H has no explicit time-dependence, then $\dot{H} = 0$ and H , the total energy is a conserved quantity.

2.3 General Procedure for Molecular Dynamics

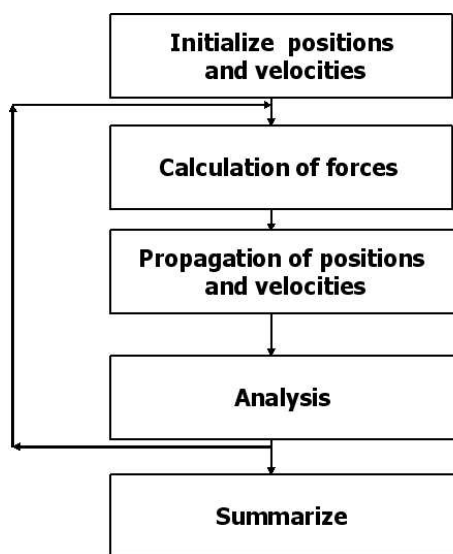


Figure 2.1: Procedure for molecular dynamics.

In MD one calculates explicitly the forces between the atoms and the motion is computed with a suitable numerical integration method using Newton's equation of motion [39, 43, 44, 45, 46, 47]. Fig. 2.1 summarizes the MD procedure in the form of a flow chart. The starting conditions are the positions and the velocities of the constituent atoms. The starting geometry can be taken from a known crystal structure or from a previous simulation. The velocities can be generated from a previous run or by using random numbers and later scale to the desired temperature. The Maxwell-Boltzmann distribution is rapidly established by molecular collisions typically within few hundreds of time steps. Calculation of atomic forces in a MD simulation is usually the most expensive operation. If there are N atoms in the system, there will be at most $N(N-1)/2$ unique atom pairs, each with an associate force to compute. For the force calculation at least for the short-range potential, the use of a cut-off applied at a certain interatomic separation allows more efficiency in computing the forces. For simulating the bulk of the system periodic boundary conditions are applied.

A production period in which trajectory of the atoms are stored follows after an equilibration period. In the equilibration period the system is coaxed towards the desired thermodynamic state point. In the production period the properties of the bulk material are drawn out of the mass of trajectory data and this is known as ensemble averaging.

The basic machineries for a program for a MD simulation are:

- (i) As already mentioned, a model for interaction between system constituents is needed. Often it is assumed that the particles interact only pair-wise, which is exact for non-polarizable particles with fixed partial charges. This assumption greatly reduces the computational effort.
- (ii) An integrator is needed, which propagates particle positions and velocities from time t to $t + dt$. It is a finite difference scheme which moves trajectories discretely in time. The time-step dt has to be chosen properly to guarantee stability of the integrator, i.e., there should be no drift in the system's energy.
- (iii) A statistical ensemble has to be chosen, where thermodynamic quantities like pressure, temperature or the number of particles are controlled.

2.4 Interaction Potential

In classical simulations the atoms are most often described by point-mass like centers which interact through pair- or many-body interaction potentials. Hence, a highly complex description of electron dynamics is abandoned and an effective picture is adopted where the main features like the hard core of a particle, electric multi-poles or internal degrees of freedom of a molecule are modeled by a set of parameters and (most often) analytical functions which depend on the mutual positions of particles in configuration. Since the parameters and the functions give a complete information of the system's energy as well as the force acting on each particle, the combination

of parameters and functions is also called *force field*. Different types of force fields were developed during the last decade. For example the most popular ones are MM3 [48], MM4 [49], Dreiding [50], SHARP [51], VALBON [52], UFF [53], CFF95 [54], AMBER [55], CHARMM [56], OPLS [57] and MMFF [58].

There exist major differences among interaction potentials. The first distinction is to be made between pair- and multi-body potentials. In a system with no constrains, the interaction is most often described by pair-potentials, which is simple to implement. In the cases where multi-body potentials come into play, the counting of interaction partners becomes increasingly more complex and dramatically slows down the execution of the program. The next difference is with respect to the spatial extent of the potential classifying it into short- and long-range interactions. If the potential drops down to zero faster than R^{-d} , where R is the separation between two particles and d the dimension of the problem, it is called short-ranged, otherwise it is long-ranged.

2.4.1 Short-range potential

Bonded interactions model rather strong chemical bonds, and are not created or broken during a simulation. For this reason, these interactions may be evaluated by running through a *fixed list* of groups of particle numbers, where each group represents a bonded interaction between two or more particles. The three most widely used bonded interactions are the covalent interaction, the bond-angle interaction and the dihedral interaction.

The covalent interaction is a bonded interaction between two particles I and J with the interaction potential

$$V_{covalent}(R_{IJ}) = \frac{1}{2}K_b(R_{IJ} - b_0)^2. \quad (2.29)$$

This interaction may be thought of as a very stiff linear spring between I and J . The spring has a natural length b_0 with a spring constant K_b .

The bond-angle interaction is a three particle interactions between I, J, K , with the interaction potential

$$V_{bond-angle}(\Theta) = \frac{1}{2}K_\Theta(\Theta - \Theta_0)^2, \quad (2.30)$$

with

$$\Theta = \arccos\left(\frac{\mathbf{R}_{IJ} \cdot \mathbf{R}_{KJ}}{R_{IJ}R_{KJ}}\right). \quad (2.31)$$

This interaction may be thought of as a torsion spring between the lines I, J and K, J . The spring has a natural angle Θ_0 with spring constant K_Θ .

The dihedral-angle interaction is a four particle interaction between I, J, K, L . Two often used expressions for this kind of potentials are

$$V_{dihedral}(\phi) = K_\phi(1 + \cos(n\phi - \delta)) \quad (2.32)$$

and

$$V_{dihedral}(\phi) = \frac{1}{2}K_\phi(\phi - \phi_0)^2, \quad (2.33)$$

where δ and ϕ_0 are constants.

Besides these internal degrees of freedom of molecules which may be modeled with short-range interaction potentials, it is also important to consider the *excluded volume* of the particles and the *non-bonded interactions*. A finite diameter of a particle may be represented by a steep repulsive potential acting at very short distances. This is either described by an exponential function or an algebraic form, $\propto R^{-n}$, where $n \geq 9$. Another source of short-range interaction is the van der Waals interaction. For a neutral molecule these are London forces arising from the induced dipole interactions. Fluctuations of the electron distribution of a particle give rise to fluctuating dipole moments, which on average compensate to zero. But the instantaneous created dipoles induce dipoles also on neighboring particles which attract each other as R^{-6} . The two commonly used forms of the resulting interactions are the Buckingham potential

$$V_{\alpha\beta}^B(R_{IJ}) = A_{\alpha\beta} \exp(-B_{\alpha\beta}R_{IJ}) - \frac{D_{\alpha\beta}}{R_{IJ}^6} \quad (2.34)$$

and the Lennard-Jones potential

$$V_{\alpha\beta}^{LJ}(R_{IJ}) = 4\epsilon_{\alpha\beta} \left[\left(\frac{\sigma_{\alpha\beta}}{R_{IJ}} \right)^{12} - \left(\frac{\sigma_{\alpha\beta}}{R_{IJ}} \right)^6 \right]. \quad (2.35)$$

The indices α, β indicate the species of the particles and parameters A, B, D in Eq. (2.34) and ϵ, σ in Eq. (2.35) are parameters for inter- and intra-species interactions. For the Lennard-Jones potential the parameters have a simple physical interpretation: ϵ is the minimum potential energy, located at $R = 2^{1/6}\sigma$ and σ is the diameter of the particle and when $R < \sigma$ the potential becomes repulsive. Often the Lennard-Jones potential gives a reasonable approximation as a true potential. However, from *ab initio* calculations it is found that an exponential type repulsive potential is more appropriate. The Lennard-Jones potential has a very steep repulsive potential part and is not suitable for dense systems. The too steep repulsive part often leads to an overestimation of the pressure in the system.

The short-range interactions offer the possibility to take into account only neighbored particles up to a certain distance for the calculation of interactions. In that way a cutoff radius R_C is introduced beyond which mutual interactions between the particles are neglected. Due to this truncation, simulations can provide only a portion of those properties, such as the internal energy and pressure, that are directly related to the potential. Simulation results for such properties must be corrected for long-range interactions ($R > R_C$) that are neglected. Truncating the potential at R_C introduces a similar truncation into the force which, in turn, causes small impulses on atoms I and J whenever their separation distance R_{IJ} crosses R_C . Consequently, instead of a strictly constant total energy E , we may observe small fluctuations in E . These fluctuations

have little effect on the values computed for equilibrium properties, and of course, the effect can be made negligible by simply increasing R_C at the expense of increased computer time for the simulation. As an approximation one may introduce a *shifted-force potential* and *long-range corrections* to the potential.

2.4.1.1 Shifted-force potential

The step change in the potential $V(R)$ and force $F(R)$ at R_C can be removed by shifting $F(R)$ vertically so that the force goes continuously to zero at R_C . Hence, a shifted force $F_s(R)$ is defined [59] by

$$F_s(R) = \begin{cases} -\frac{dV}{dR} + \Delta F & R \leq R_C \\ 0 & R > R_C \end{cases} \quad (2.36)$$

where ΔF is the magnitude of the shift,

$$\Delta F = -F(R_C) = \left(\frac{dV}{dR}\right)_{R_C}. \quad (2.37)$$

The shifted potential $V_s(R)$ corresponding to $F_s(R)$ can be derived from

$$F_s(R) = -\frac{dV_s(R)}{dR} \quad (2.38)$$

or

$$\int_0^{V_s} dV_s = -\int_\infty^R F_s(R) dR. \quad (2.39)$$

Substituting Eq. (2.36) into Eq. (2.39) and integrating gives

$$V_s(R) = \begin{cases} V(R) - V(R_C) - [R - R_C] \left(\frac{dV}{dR}\right)_{R_C} & R \leq R_C \\ 0 & R > R_C \end{cases} \quad (2.40)$$

The shifted-force correction removes the energy fluctuations that occur because of the truncations of V and F .

2.4.1.2 Long-range correction

One may introduce *long-range corrections* to the potential in order to compensate for the neglect of explicit calculations. The whole potential may then be written as

$$V = \sum_{I < J}^N V(R_{IJ} | R_{IJ} < R_C) + V_{lrc}. \quad (2.41)$$

The long-range correction is thereby given as

$$V_{lrc} = 2\pi N \rho_0 \int_{R_C}^{\infty} R^2 g(R) V(R) dR \quad (2.42)$$

where ρ_0 is the number density of the particles in the system and $g(R) = \rho(R)/\rho_0$ is the radial distribution function. For computational reasons, $g(R)$ is most often only calculated up to R_C . However beyond $R > R_C$ the system is assumed to be uniform. This amounts to the mean-field approximation for the long-range portion of the potential. Thus at a fixed number density, the long-range correction is merely a constant that is added.

2.4.2 Long-range potential

In the case of long-range potentials, like the Coulomb potential, interactions between all the particles in the system must be taken into account, if treated without any approximation. Consider a classical system of N bodies with charges q_i and masses m_i at position vectors \mathbf{r}_i interacting via a Coulombic potential V . The equations of motion are

$$m_i \frac{d^2 \mathbf{r}_i}{dt^2} = -q_i \nabla_i V \quad \text{for } i = 1, 2, 3, \dots, N \quad (2.43)$$

where

$$V(r_i) = \sum_{j \neq i}^N \frac{q_j}{|\mathbf{r}_i - \mathbf{r}_j|}. \quad (2.44)$$

These lead to an $O(N^2)$ problem, which is computationally quite expensive for large systems. For systems with open boundary conditions this method is straightforwardly implemented and reduces to a double sum over all pairs of particles. In the case where periodic boundary conditions are applied, the interactions not only within the particles in the central cell are important but also those with all periodic images must be taken into account. And hence, a lattice sum has to be evaluated and the potential is expressed as:

$$V_s(r_i) = \sum_{\mathbf{n}} ' \sum_{j=1}^N \frac{q_j}{|\mathbf{r}_{ij} + \mathbf{n}|} \quad (2.45)$$

where $\mathbf{r}_{ij} = \mathbf{r}_i - \mathbf{r}_j$ and $\mathbf{n} = (i_x, i_y, i_z)L$, with $i_\alpha = 0, \pm 1, \pm 2 \dots \pm \infty$. The prime in the summation of \mathbf{n} indicates that $i = j$ term is omitted for the primary cell $\mathbf{n} = 0$. The summation over image boxes as in Eq. (2.45) makes the $O(N^2)$ problem to $N_{box} \times N^2$ operations! This sum is also a conditionally convergent series. A method to overcome this limitation was introduced by Ewald [60]. The characterization of convergence is given in Refs. [61,62]. In the Ewald summation technique the potential is recasted into the sum of two rapidly converging series: one in real space; the other in reciprocal, or k -space:

$$V_E(r_i) = \sum_{\mathbf{n}} ' \sum_{j=1}^N q_j \frac{\text{erfc}(\alpha |\mathbf{r}_{ij} + \mathbf{n}|)}{|\mathbf{r}_{ij} + \mathbf{n}|} + \frac{4\pi}{L^3} \sum_{\mathbf{k} \neq 0} \sum_{j=1}^N q_j \exp\left(\frac{-|k|^2}{4\alpha^2}\right) \exp\{\mathbf{i}\mathbf{k} \cdot (\mathbf{r}_{ij})\} - \frac{2\alpha}{\pi^{1/2}} q_i, \quad (2.46)$$

where $\operatorname{erfc}(x) = \frac{2}{\sqrt{\pi}} \int_0^x \exp(-t^2) dt$. The term α governs the relative convergence rates of the two main series. The last term is a "self-potential" which cancels an equivalent contribution in the k -space sum. A physical interpretation of this decomposition of the lattice sum given in Eq. (2.46) follows. Each point charge in the system is viewed as being surrounded by a Gaussian charge distribution of equal magnitude and opposite sign with charge distribution

$$\rho(r) = A \exp(-\alpha^2 r^2) \quad (2.47)$$

This introduced charge distribution screens the interaction between neighboring point-charges, effectively limiting them to a short-range. Consequently, the sum over all charges and their images in real space converges rapidly. To counteract this induced Gaussian distribution, a second Gaussian charge distribution is added and the sum is performed in the reciprocal space using Fourier transformation. The choice of charge distribution is actually not too critical and mainly influences the convergence of the series. Refer to Ref. [64] where the Ewald sum has been cast with various non-Gaussian charge distributions.

The equivalent expression for the force (or more correctly the electric field) can be obtained by direct differentiation with respect to the vector between the reference particle i and particle j :

$$\begin{aligned} F(\mathbf{r}_i) &= -\frac{\partial V_E(r_i)}{\partial \mathbf{r}_{ij}} \\ &= \sum_{\mathbf{n}} ' \sum_{j=1}^N \frac{q_j \mathbf{r}_{ij, \mathbf{n}}}{r_{ij, \mathbf{n}}^3} \left[\operatorname{erfc}(\alpha r_{ij, \mathbf{n}}) + \frac{2\alpha r_{ij, \mathbf{n}}}{\pi^{1/2}} \exp(-\alpha^2 r_{ij, \mathbf{n}}^2) \right] \\ &\quad + \frac{4\pi}{L^3} \sum_{\mathbf{k} \neq 0} \sum_j q_j \frac{\mathbf{k}}{k^2} \exp\left(\frac{-k^2}{4\alpha^2}\right) \sin(\mathbf{k} \cdot \mathbf{r}_{ij}). \end{aligned} \quad (2.48)$$

In the above expression $\mathbf{r}_{ij, \mathbf{n}} \equiv \mathbf{r}_{ij} + \mathbf{n}$. Refer to Refs. [61, 62, 64, 65, 63] for more details on lattice sums through Ewald summation.

2.5 Integrators

For a given potential model which characterizes the physical system, it is the integrator which is responsible for the accuracy of the simulation. The integrator is the routine which actually moves the atoms, depending on the current forces and velocities. The basic criteria for a good integrator for molecular simulations are as follows:

- (i) It must show good conservation of energy and momentum and small perturbations should not lead to instabilities. It must be time-reversible.
- (ii) It should permit the use of a relatively long time step in order to propagate the

system efficiently through the phase space.

(iii) It should require little computer memory.

(iv) It should be fast, ideally requiring only one energy evaluation per time step.

(v) It should duplicate the classical trajectory as closely as possible.

Any finite-difference integrator is an approximation for a system developing continuously in time. These methods are explicit and use the information available at time t to predict the system's coordinates and velocities at time $t + dt$, where dt is a short time interval. These methods are based on a Taylor expansion of the position at time $t + dt$:

$$\mathbf{r}(t + dt) = \mathbf{r}(t) + \mathbf{v}(t)dt + \frac{\mathbf{a}(t)}{2}dt^2 + \dots, \quad (2.49)$$

where $\mathbf{v}(t)$ is the first derivative of the position $\mathbf{r}(t)$, $\mathbf{a}(t)$ is the second derivative of the position etc.

A finite-difference method leads to two types of errors: *truncation error* and *round-off error*. Truncation error refers to the accuracy with which a finite-difference method approximates the true solution to a differential equation. When a finite-difference equation is written in Taylor series form as in Eq. (2.49), the truncation error is measured by the first non-zero term that has been omitted from the series. In contrast, the round-off error encompasses all errors that result from the implementation of the finite-difference algorithm. For example, the round-off error is affected by the number of significant figures kept at each stage of the calculations which are actually performed, and by any approximations used in evaluating square roots, exponentials and so on.

In the following different types of integration schemes are presented.

2.5.1 Verlet integrator

The most basic and most common integration algorithm is the Verlet integrator, which is based on the expansion of position in a Taylor series. For a small enough time step dt the expansion gives

$$\mathbf{r}(t + dt) = \mathbf{r}(t) + \mathbf{v}(t)dt + \frac{\mathbf{F}(t)}{2m}dt^2 + \dots \quad (2.50)$$

In the same way the expansion may be performed for $dt \rightarrow -dt$, which gives

$$\mathbf{r}(t - dt) = \mathbf{r}(t) - \mathbf{v}(t)dt + \frac{\mathbf{F}(t)}{2m}dt^2 - \dots \quad (2.51)$$

Adding up Eqs. 2.50 and 2.51 gives new positions

$$\mathbf{r}(t + dt) = 2\mathbf{r}(t) - \mathbf{r}(t - dt) + \frac{\mathbf{F}(t)}{m}dt^2 + O(dt^4) \quad (2.52)$$

Advantages:

(i) Integration does not require the velocities, only position information is taken into

account.

- (ii) Only a single force evaluation per integration cycle is necessary. (The force evaluation is the computationally most expensive part in the simulation).
- (iii) This formulation, which is based on forward and backward expansions, is naturally reversible in time (a property of the equation of motion).

Disadvantages:

- (i) The velocities, which are required for the kinetic energy evaluation, are calculated only in an approximate manner through the equation

$$\mathbf{v}(t) = \frac{\mathbf{r}(t+dt) + \mathbf{r}(t-dt)}{2 dt} \quad (2.53)$$

This is, however, one order less in accuracy than Eq. (2.52).

- (ii) From the point of view of storage requirement Eq. (2.53) is not optimal, since information is required from positions not only at time t but also at time $t - dt$.

2.5.2 Leap Frog integrator

The Leap Frog integrator is a variation of the Verlet algorithm designed to improve the velocity evaluation. Its name comes from the fact that the velocities are evaluated at the mid-point of the position evaluation and vice versa. The algorithm is as follows:

$$\mathbf{v}(t+dt/2) = \mathbf{v}(t-dt/2) + \mathbf{a}(t)dt \quad (2.54)$$

$$\mathbf{r}(t+dt) = \mathbf{r}(t) + \mathbf{v}(t+dt/2)dt \quad (2.55)$$

This means that each integration cycle involves three step:

- (i) Calculate $\mathbf{a}(t)dt$ based on $\mathbf{r}(t)$, i.e., $\mathbf{a}(t) = -(1/m)\nabla V(\mathbf{r}(t))$.
- (ii) Calculate $\mathbf{v}(t+dt/2)$
- (iii) Calculate $\mathbf{r}(t+dt)$

The *instantaneous* velocity at time t is then calculated as

$$\mathbf{v}(t) = (\mathbf{v}(t+dt/2) + \mathbf{v}(t-dt/2))/2 \quad (2.56)$$

Advantages:

- (i) Improved evaluation of velocities.
- (ii) Direct evaluation of velocities gives a useful handle for controlling the temperature in the simulation.

Disadvantages:

- (i) The velocities at time t are still approximate.
- (ii) Computationally more expensive than the Verlet algorithm.

2.5.3 Velocity Verlet integrator

An even improved integrator is this algorithm which is designed to further improve on the velocity evaluations. The algorithm is as follows:

$$\mathbf{r}(t + dt) = \mathbf{r}(t) + \mathbf{v}(t)dt + \frac{1}{2}\mathbf{a}(t)dt^2 \quad (2.57)$$

$$\mathbf{v}(t + dt) = \mathbf{v}(t) + \frac{1}{2}(\mathbf{a}(t) + \mathbf{a}(t + dt))dt \quad (2.58)$$

This means that each integration cycle involves four steps:

- (i) Calculate $\mathbf{r}(t + dt)$ using Eq. (2.57).
- (ii) Calculate the mid-point velocity: $\mathbf{v}(t + dt/2) = \mathbf{v}(t) + \mathbf{a}(t)dt/2$
- (iii) Calculate $\mathbf{a}(t + dt) = -(1/m)\nabla V(\mathbf{r}(t + dt))$
- (iv) Calculate $\mathbf{v}(t + dt) = \mathbf{v}(t + dt/2) + \mathbf{a}(t + dt)dt/2$

Advantage: Best evaluation of velocities.

Disadvantage: Computationally more expensive than the Verlet or Leap Frog algorithms.

2.6 Simulations in Different Ensembles

2.6.1 Sampling from an ensemble

The thermodynamic state of a system is usually defined by a small set of parameters (such as the number of particles N , the temperature T and the pressure P) and not by the very many atomic positions and momenta that define the instantaneous mechanical state. These positions and momenta can be thought of as coordinates in a multidimensional space: phase space. For a system of N particles this space has $6N$ dimensions. The state of the classical N -body system at any time t is completely specified by the location of one point in phase space denoted as Γ . One can write the instantaneous value of some property \mathcal{A} as function $\mathcal{A}(\Gamma)$. As the system evolves in time, Γ and $\mathcal{A}(\Gamma)$ will change. Hence, one can assume the experimentally observable macroscopic property \mathcal{A}_{obs} is an average of $\mathcal{A}(\Gamma)$ taken over a long interval of time t_{obs} :

$$\mathcal{A}_{obs} = \langle \mathcal{A} \rangle_{time} = \lim_{t_{obs} \rightarrow \infty} \frac{1}{t_{obs}} \int_0^{t_{obs}} \mathcal{A}(\Gamma(t))dt. \quad (2.59)$$

In MD the equations of motion are usually solved approximately by a step-by-step procedure, i.e., a large finite number τ_{obs} of time steps, of length $dt = t_{obs}/\tau_{obs}$. The Eq. (2.59) becomes then

$$\mathcal{A}_{obs} = \langle \mathcal{A} \rangle_{time} = \frac{1}{\tau_{obs}} \sum_{\tau=1}^{\tau_{obs}} \mathcal{A}(\Gamma(\tau)). \quad (2.60)$$

Hence, integration of the equations of motion should then yield a trajectory that describes how the positions, velocities and accelerations of the particles vary with time, and from which the average values of the properties can be determined using Eq. (2.60). However, there exists the difficulty that for 'macroscopic' numbers of atoms or molecules it is not even feasible to determine an initial configuration of the system, let alone integrate the equations of motion and calculate a trajectory. Recognizing this problem, Boltzmann and Gibbs developed statistical mechanics, in which a single system evolving in time is replaced by a large number of replications of the system that are considered simultaneously and are known as ensemble. An ensemble is a collection of points Γ in phase space. The points are distributed according to a probability density $\rho_{ens}(\Gamma)$. Hence the time average in Eq. (2.60) is then replaced by an ensemble average:

$$\mathcal{A}_{obs} = \langle \mathcal{A} \rangle_{ens} = \sum_{\Gamma} \mathcal{A}(\Gamma) \rho_{ens}(\Gamma) \quad (2.61)$$

One can use a weight function $w_{ens}(\Gamma)$, instead of $\rho_{ens}(\Gamma)$ satisfying the following equations:

$$\rho_{ens}(\Gamma) = Q_{ens}^{-1} w_{ens}(\Gamma) \quad (2.62)$$

$$Q_{ens} = \sum_{\Gamma} w_{ens}(\Gamma) \quad (2.63)$$

$$\mathcal{A}_{ens} = \sum_{\Gamma} w_{ens}(\Gamma) \mathcal{A}_{ens}(\Gamma) / \sum_{\Gamma} w_{ens}(\Gamma). \quad (2.64)$$

The partition function Q_{ens} is a function of the macroscopic properties defining the ensemble. One can define a thermodynamic potential Ψ_{ens}

$$\Psi_{ens} = -\ln Q_{ens}, \quad (2.65)$$

which has a minimum at the thermodynamical equilibrium.

2.6.2 Common statistical ensembles

2.6.2.1 The micro-canonical ensemble

The probability density for the micro-canonical ensemble is proportional to

$$\delta(H(\Gamma) - E),$$

where $H(\Gamma)$ is the Hamiltonian. The delta function selects those states of an N particle system in a container of volume V that have the desired energy E . In a computer simulation this theoretical condition is generally violated, due to the limited accuracy in integrating the equation of motion and due to round-off errors resulting from a

limited precision of number representation. The micro-canonical partition function may be written as,

$$Q_{NVE} = \sum_{\Gamma} \delta(H(\Gamma) - E). \quad (2.66)$$

The corresponding thermodynamic potential is the negative of the entropy

$$-S/k_B = -\ln Q_{NVE}. \quad (2.67)$$

k_B represents the Boltzmann constant.

2.6.2.2 The canonical ensemble

The density for the canonical ensemble is proportional to

$$\exp(-H(\Gamma)/k_B T)$$

and the partition function is

$$Q_{NVT} = \sum_{\Gamma} \exp(-H(\Gamma)/k_B T). \quad (2.68)$$

The corresponding thermodynamic potential is the Helmholtz free energy A

$$A/k_B T = -\ln Q_{NVT}. \quad (2.69)$$

In a canonical ensemble, all values of the energy are allowed and energy fluctuations are non-zero. The time evolution occurs on a set of independent constant-energy surfaces, each of which is appropriately weighted by the factor $\exp(-H(\Gamma)/k_B T)$. Hence the algorithm for this ensemble should allow the generation of a succession of states and must make provision for transitions between the energy surfaces so that a single trajectory can probe all the accessible phase space, and yield the correct relative weighting.

2.6.2.3 The isothermal-isobaric ensemble

The probability density for the isothermal-isobaric ensemble is proportional to

$$\exp(-(H + PV)/k_B T).$$

Upon averaging the quantity in the exponent, the thermodynamic enthalpy $\mathcal{H} = \langle H \rangle + P \langle V \rangle$ is obtained. The partition function is

$$Q_{NPT} = \sum_{\Gamma} \sum_V \exp((-H + PV)/k_B T) = \sum_V \exp(-PV/k_B T) Q_{NVT}. \quad (2.70)$$

The corresponding thermodynamic function is the Gibbs free energy G

$$G/k_B = -\ln Q_{NPT}. \quad (2.71)$$

For a constant NPT ensemble the algorithm should allow for changes in the sample volume as well as the energy.

2.6.2.4 The grand canonical ensemble

The density for the grand canonical ensemble is proportional to

$$\exp(-(H - \mu N)/k_B T)$$

where μ is the chemical potential. Here the number of particles N is a variable, along with the coordinates and momenta. The grand canonical partition function is

$$Q_{\mu VT} = \sum_{\Gamma} \sum_N \exp(-(H - \mu N)/k_B T) = \sum_N \exp(\mu N/k_B T) Q_{NPT}. \quad (2.72)$$

The corresponding thermodynamic function is just $-PV/k_B T$:

$$-PV/k_B T = -\ln Q_{\mu VT}. \quad (2.73)$$

Hence the algorithm in the grand canonical ensemble must allow for addition and removal of particles. In this kind of ensemble the extensive parameters show unbounded fluctuation, i.e., the system size can grow without limit. Hence this ensemble is not so common for simulations using MD.

In the MD simulation it is possible to realize different types of thermodynamic ensembles by controlling certain thermodynamic quantities. In the following we describe different algorithms to control temperature and pressure.

2.6.3 Molecular dynamics at constant temperature

The instantaneous kinetic energy is given by

$$K(t) = \frac{1}{2} \sum_i^N m_i (v_i(t))^2 \quad (2.74)$$

The temperature T is directly related to the kinetic energy by the well-known equipartition formula, assigning an average kinetic energy $k_B T/2$ per degree of freedom:

$$K = \frac{3}{2} N k_B T \quad (2.75)$$

An estimate of the temperature is therefore directly obtained from the average kinetic energy K . For practical purposes, it is also common practice to define an *instantaneous temperature* $T(t)$, proportional to the instantaneous kinetic energy $K(t)$ by a relation analogous to Eq. (2.75).

2.6.3.1 Velocity rescaling

The temperature change is achieved by rescaling the velocities in order to bring the system to a desired temperature. In the framework of the velocity Verlet algorithm this may be accomplished by replacing the step

$$\mathbf{v}(t + dt/2) = \mathbf{v}(t) + \mathbf{a}(t)dt/2$$

with

$$\mathbf{v}(t + dt/2) = \sqrt{\frac{T_{des}}{T(t)}} \mathbf{v}(t) + \mathbf{a}(t)dt/2, \quad (2.76)$$

where T_{des} is the desired temperature and $T(t)$ is the instantaneous temperature.

2.6.3.2 Gaussian thermostat

Another way to control the temperature is to use a constrain on the equation of motion. Gauss' principle of least constraint states that a force added to restrict a particle motion on a constraint hypersurface should be normal to the surface of the realistic dynamics [66]. The constant temperature constraint has the form

$$\frac{1}{2} \sum_{i=1}^N m_i \mathbf{v}_i^2 - \frac{3}{2} N k_B T_{des} = 0. \quad (2.77)$$

Gauss' principle yields (differentiation of Eq. (2.77) with respect to t)

$$\sum_{i=1}^N m_i \mathbf{v}_i \mathbf{a}_i = \sum_{i=1}^N \mathbf{F}_i \mathbf{v}_i = 0. \quad (2.78)$$

To derive the Gaussian equation of motion, $m_i \mathbf{a}_i$ is substituted by $\mathbf{F}_i - \dot{\xi} m_i \mathbf{v}_i$. The resulting equation is then solved for the time derivative of the friction coefficient, $\dot{\xi}$, which yields

$$\dot{\xi} = \frac{\sum_{i=1}^N \mathbf{F}_i \cdot \mathbf{v}_i}{\sum_{i=1}^N m_i \mathbf{v}_i^2} \quad (2.79)$$

The Gaussian thermostat can be easily combined with the velocity Verlet integrator as:

(i) Calculate the thermostat variable $\dot{\xi}(t) = [\sum_{i=1}^N m_i \mathbf{a}_i(t) \cdot \mathbf{v}_i(t)] / [\sum_{i=1}^N m_i \mathbf{v}_i^2(t)]$.

(ii) Evaluate velocities: $\mathbf{v}_i(t + dt/2) = \mathbf{v}_i(t) + [\mathbf{a}_i(t) - \mathbf{v}_i(t) \dot{\xi}(t)] dt/2$.

(iii) Evaluate positions: $\mathbf{r}_i(t + dt/2) = \mathbf{r}_i(t) + \mathbf{v}_i(t + dt/2) dt$.

(iv) Calculate $\mathbf{F}_i(t + dt)$ and $\mathbf{a}_i(t + dt)$ and repeat from (i) for $t + dt$.

2.6.3.3 Andersen thermostat

In the constant-temperature method proposed by Andersen [67] the system is coupled to a heat bath that imposes the desired temperature. The coupling to the heat bath is represented by stochastic forces that act occasionally on randomly selected particles. To perform the simulation one must first choose two parameters: the desired temperature, T_{des} , and the mean rate at which each particles suffers stochastic collisions, ν . The probability that a particular particle suffers a stochastic collision in time dt is νdt .

The times at which each particle suffers a collision is decided before beginning of the simulation. This can be done by using random numbers to generate the values for the time intervals between successive collisions of a particle. Such intervals are distributed according to

$$P(t) = \nu \exp(-\nu t), \quad (2.80)$$

where $P(t)dt$ is the probability that the next collision will take place in the interval $[t, t + dt]$. Hence, as the calculations proceed, random numbers can be used to decide which particles are to suffer collisions in time interval dt .

A constant-temperature involving Andersen thermostat consists of the following steps:

- (i) Start with an initial set of positions and momenta and integrate the equations of motion for a time dt .
- (ii) A number of particles are selected to undergo a collision with the heat bath.
- (iii) If particle i has been selected to undergo a collision, its new velocity will be taken from a Maxwell-Boltzmann distribution corresponding to T_{des} . All other particles are unaffected by this collision.

The Andersen thermostat is consistent with the canonical ensemble and quite good for the algorithms used for investigating static properties. However it is risky to use this method when studying dynamical properties. The reason for this is that this method is based on stochastic collisions and disturbs the dynamics of the systems in an unrealistic way, which may lead to sudden random de-correlation of particle velocities.

2.6.3.4 Nosé-Hoover thermostat

This is an extended system method as it introduces additional degrees of freedom into the system's Hamiltonian. They are integrated in line with the equations for the spatial coordinates and momenta. According to the Nosé-Hoover thermostat, the effect of an external system acting as heat reservoir to keep the temperature of the system constant, is reduced to one additional degree of freedom [68]. The thermal interactions between a heat reservoir and the system result in a change of the kinetic energy, i.e., the velocities are subjected to scaling. There exist two sets of variables: real and virtual. In the following the relations between real and virtual variables are given. Real variables are indicated by a prime, to distinguish them from their unprimed virtual counterparts.

$$r' = r \quad (2.81)$$

$$p' = p \quad (2.82)$$

$$dt' = dt/s, \quad (2.83)$$

where dt is the virtual time interval and s is a scaling factor. An effective mass, M_s , is introduced as an additional degree of freedom with momentum π_s . The resulting

Hamiltonian, expressed in virtual coordinates, gives:

$$H_{NH} = \sum_i^N \frac{\mathbf{p}_i^2}{2m_i s^2} + V(r) + \frac{\pi_s^2}{2M_s} + gk_B T \ln s, \quad (2.84)$$

where $g = 3N + 1$ is the number of degrees of freedom (system of N free particles). One gets the equations of motion in real variables (dropping primes) as:

$$\dot{\mathbf{r}}_i = \mathbf{p}_i / m_i \quad (2.85)$$

$$\dot{\mathbf{p}}_i = -\frac{dV(\mathbf{r})}{d\mathbf{r}_i} - \xi \mathbf{p}_i \quad (2.86)$$

$$\dot{\xi} = \frac{1}{M_s} \left(\sum_i p_i^2 / m_i - gk_B T \right) \quad (2.87)$$

$$\xi = \frac{d \ln s}{dt}. \quad (2.88)$$

This method provides a way to keep the temperature constant more gently than the Andersen's method where particles get new, random velocities.

2.6.4 Molecular dynamics at constant pressure

The measurement of the pressure in a MD simulation is based on the Clausius virial function

$$W(r) = \sum_{i=1}^N \mathbf{r}_i \cdot \mathbf{F}_i^{tot}, \quad (2.89)$$

where \mathbf{F}_i^{tot} is the total force acting on an atom i . Its statistical average $\langle W \rangle$ is obtained as an average over the molecular dynamics trajectory:

$$\langle W \rangle = \lim_{t' \rightarrow \infty} \frac{1}{t'} \int_0^{t'} dt \sum_{i=1}^N \mathbf{r}_i(t) \cdot m_i \dot{\mathbf{r}}_i(t). \quad (2.90)$$

By integrating by parts,

$$\langle W \rangle = - \lim_{t' \rightarrow \infty} \frac{1}{t'} \int_0^{t'} dt \sum_{i=1}^N m_i |\dot{\mathbf{r}}_i(t)|^2. \quad (2.91)$$

This represents twice the kinetic energy. Therefore by the equipartition law of statistical mechanics we get,

$$\langle W \rangle = -3Nk_B T. \quad (2.92)$$

The total force can be decomposed into two contributions:

$$\mathbf{F}_i^{tot} = \mathbf{F}_i + \mathbf{F}_i^{ext}, \quad (2.93)$$

where \mathbf{F}_i is the internal force arising from the interatomic interactions, and \mathbf{F}_i^{ext} is the external force exerted by the container's wall. If the particles are enclosed in a rectangular container of sides L_x, L_y, L_z with volume $V = L_x L_y L_z$, and with the coordinates' origin on one of its corners. $\langle W^{ext} \rangle$ due to the container can be evaluated using Eq. (2.89):

$$\langle W^{ext} \rangle = L_x(-PL_y L_z) + L_y(-PL_x L_z) + L_z(-PL_x L_y) = -3PV \quad (2.94)$$

where for instance $-PL_y L_z$ is the external force F_x^{ext} applied by the yz wall along the x direction, etc. Eq. (2.92) can be written as

$$\begin{aligned} \langle \sum_i^N \mathbf{r}_i \cdot \mathbf{F}_i \rangle - 3PV &= -3Nk_B T \\ \text{or } PV &= Nk_B T + \frac{1}{3} \langle \sum_i^N \mathbf{r}_i \cdot \mathbf{F}_i \rangle. \end{aligned} \quad (2.95)$$

This equation is known as *virial equation*. All the quantities except P are easily accessible in a simulation and therefore it provides a way to calculate P . Note that Eq. (2.95) reduces to the well-known equation of state of the ideal gas if the particles are non-interacting.

2.6.4.1 Andersen's method

Andersen originally proposed a method for constant pressure MD, which involves coupling to an external variable V , the volume of the simulation box [67]. This coupling mimics the action of a piston on a real system. The piston has a mass Q and is associated with the kinetic energy

$$\mathcal{K}_V = \frac{1}{2} Q \dot{V}^2. \quad (2.96)$$

The potential energy associated with the additional variable is

$$\mathcal{V}_V = PV \quad (2.97)$$

where P is the specified pressure. The positions and velocities of the atoms are given in term of scaled coordinates as:

$$\mathbf{r} = V^{1/3} \mathbf{s} \quad (2.98)$$

$$\mathbf{v} = V^{1/3} \dot{\mathbf{s}}. \quad (2.99)$$

The potential and kinetic energies associated with the particles are $V(\mathbf{r}) = V(V^{1/3} \mathbf{s})$ and $K = \frac{1}{2} m V^{2/3} \sum_i \dot{\mathbf{s}}^2$. The equations of motion become:

$$\ddot{\mathbf{s}} = \mathbf{f}/(mV^{1/3}) - (2/3)\dot{\mathbf{s}}\dot{V}/V \quad (2.100)$$

$$\ddot{V} = (\mathcal{P} - P)/Q \quad (2.101)$$

where \mathcal{P} represents the net *instantaneous pressure* due to the external and internal forces. Both \mathcal{P} and \mathbf{f} are calculated using normal, un-scaled coordinates and momenta. The equations of motion generate trajectories which sample the isobaric-isoenthalpic ensemble.

The parameter Q is an adjustable parameter. A *small* mass will result in rapid oscillations in box size, whereas a *large* mass will give rise to slow exploration of volume-space. Andersen recommends that the time scale for box-volume fluctuations should be roughly the same as those for a sound wave to cross the simulation box.

2.6.4.2 Parrinello's and Rahman's method

The constant pressure method of Andersen allows for isotropic change in the volume of the simulation box. Parrinello and Rahman have extended this method to allow the simulation box to change shape as well as size [69, 70, 71]. In this method the scaled coordinates are introduced through the equation

$$\mathbf{r} = \mathbf{H}\mathbf{s} \quad (2.102)$$

where $\mathbf{H} = (\mathbf{h}_1, \mathbf{h}_2, \mathbf{h}_3)$ is a transformation matrix whose columns are the three vectors \mathbf{h}_α representing the sides of the box. The volume of the box is given by

$$V = |\mathbf{H}| = \mathbf{h}_1 \cdot \mathbf{h}_2 \times \mathbf{h}_3. \quad (2.103)$$

The potential energy associated with the box is

$$\mathcal{V}_V = PV \quad (2.104)$$

and the corresponding kinetic energy term is

$$\mathcal{K}_V = \frac{1}{2}Q \sum_{\alpha} \sum_{\beta} \dot{H}_{\alpha\beta}^2. \quad (2.105)$$

The equations of motion are:

$$m\ddot{\mathbf{s}} = \mathbf{H}^{-1}\mathbf{f} - m\mathbf{G}^{-1}\dot{\mathbf{G}}\dot{\mathbf{s}} \quad (2.106)$$

$$q\ddot{\mathbf{H}} = (\mathcal{P} - \mathbf{1}P)V(\mathbf{H}^{-1})^T \quad (2.107)$$

where $\mathbf{G} = \mathbf{H}^T\mathbf{H}$ is a tensor. The pressure \mathcal{P} plays the same role as in Andersen's method.

2.7 Periodic Boundary Conditions

One can perform two kinds of treatment for simulating the boundaries of the system. One possibility is doing nothing special. Here the system simply terminates and atoms

near the boundary would have less neighbors than atoms inside. In other words, the system is surrounded by surfaces. This kind of simulation is realistic only when we want to simulate clusters of atoms. In order to simulate bulk one uses *periodic boundary conditions* (PBC).

When using PBC, particles are enclosed in a box and this box is replicated to infinity by translation in all the three Cartesian directions, completely filling the space. Hence, if one of the particles is located at the position \mathbf{r} in the box, this particle really represents an infinite set of particles located at

$$\mathbf{r} + l\mathbf{a} + m\mathbf{b} + n\mathbf{c}, \quad l, m, n \in (-\infty, \infty),$$

where l, m, n are integers and $\mathbf{a}, \mathbf{b}, \mathbf{c}$ are the vectors corresponding to the edges of the simulation box.

Apparently, the number of interacting pairs becomes infinite as an effect of PBC. In practice this is not true because for a given accuracy the potentials usually have a short interaction range. The *minimum image criterion* is followed in order to reduce the level of additional complexity introduced by the use of PBC. Consider a potential with a finite range, i.e., when separated by a distance equal or larger than a cutoff distance R_c , two particles do not interact with each other. Therefore it is sufficiently accurate to choose a box size larger than $2R_c$ along each Cartesian direction.

When these conditions are satisfied, it is obvious that almost one among all the pairs formed by a particle i in the box and the set of all the periodic images of another particle j will interact. When we work under these conditions, we can safely use the minimum image criterion, i.e., among all possible images of a particle j , the closest one is selected. This condition greatly simplifies the set up of a MD program and is commonly used. Of course, one must make sure that the box size is at least $2R_c$ along the directions where PBC's are in effect.

Chapter 3

Large-Scale Optimization

3.1 Basic Approach to Large-Scale Optimization

The (partially) amorphous systems are characterized by various configurations and interconversions between them are possible due to the internal vibrations and bond changes. By relating the changes in these motions to the potential energy function, it is possible to regard changes in the system as movements on the multidimensional surface that describes the relationship between the value of the energy function and the configurations. Stable configurations of the system correspond to the local minima on the potential energy surface. The relative population of the minima depends on their statistical weight, which includes contributions from both the potential energy and the entropy. The global energy minimum on the potential energy surface does not necessarily correspond to the structure with the highest statistical weight. To perform a "configurational search" it is therefore necessary to determine those minimum energy configurations that are believed to contribute to the overall configurational partition function. This requires some methods for determining minima on the surface described by the potential energy function.

A common strategy is to use the method of MD to search the configurational space and select configurations at regular time intervals from the trajectory and minimizing them to the associated minimum energy structures. If sufficiently large numbers of time steps are used and the temperature is high enough to enable the barriers to be overcome, then in principle, all the potential energy minima could be identified. However, in MD the time step must be smaller than the period of the highest frequency motion of the constituting molecules. For this reason a time step on the order of 1 fs must be used, and with current available hardware only relatively short simulations are possible, often far too small to ensure that the whole configurational space has been covered.

Hence, one of the typical optimization applications in MD is to minimize the potential energy functions for seeking favorable configurational states of a system. The

sheer size of the configuration space and the complexity of the system introduce extensive computational requirements and the multiple-minima problem.

The multiple-minima problem is a big problem for the large-scale optimization methods. For reasonable small problems suitable algorithms exist for finding all the local minima for linear and nonlinear functions. For large problems, however many trials are required to locate the local minima and finding of the global minima cannot be ensured. These unfavorable features have prompted development in conformational search techniques along with minimization.

Local optimization methods are essentially descent methods. They are defined as an iterative procedure: $\{\mathbf{x}_0, \mathbf{x}_1, \dots, \mathbf{x}_k, \dots\}$ that attempts to find one local minimum \mathbf{x}^* from a given \mathbf{x}_0 . In each step a search vector \mathbf{p}_k is computed by a given strategy so that the function f is minimized approximately along that direction. The performance of these methods is sensitive to the choice of the starting point in addition to the search direction and algorithmic details.

Global optimization methods in contrast to the local methods, explore larger regions of the function space. These methods can be classified as deterministic and stochastic methods. In deterministic methods, a sequence of points is constructed converging towards lower and lower local minima. Ideally, they attempt to tunnel through the local barriers. Computational effort tends to be very large and guarantee of success can only be obtained under some specific assumptions. Local minimization methods are often required repeatedly. This field of deterministic global optimization is still in its infancy, however, there exist algorithms for this approach [72, 73, 74, 75].

Stochastic global methods, on the other hand, involve systematic manipulation of randomly selected points [72]. Success can be guaranteed only in stochastic sense. The simulated annealing method is a popular and effective technique for small to medium molecular systems. Simulated annealing is very fast to implement and requires no derivative computation [76, 77, 78, 79, 80]. This method has already established itself as a powerful method for solving combinatorial optimization problems, in which the "best" or "optimum" solution must be discovered from a large number of possible solutions. This method uses a control parameter to play the role of the temperature and a stochastic algorithm is used to generate a sequence of solutions to the problem (a process equivalent to a physical system coming to thermal equilibrium). The value of the control parameter is steadily decreased and by the application of the stochastic algorithm at each stage, the system reaches "thermal equilibrium" at each temperature. If this is achieved, then an analogy can be drawn with the Boltzmann distribution, which gives the most probable population of a state i with energy E_i at the temperature T :

$$n_i = [N \exp(-E_i/kT)] / \sum_j \exp(E_j/kT) \quad (3.1)$$

As the temperature is reduced, the lower energy states become more probable until at absolute zero the system occupies the lowest possible energy state. In practice the simulated annealing algorithm is only approximate because convergence to the globally

optimal solution would require an infinite number of time steps, at each of which the system must be allowed to come to the thermal equilibrium.

In contrast to the global methods, the local methods have experienced far more extensive developments and produced a range of robust and reliable techniques tailored to the problem size, smoothness, complexity and memory consideration. Refer to Refs. [81,82,83,84] for details. The following sections are mainly concerned with this class of methods.

3.2 Basic Descent Structure of Local Methods

The fundamental structure of local iterative techniques for solving unconstrained minimization problems is simple. Let $f(\mathbf{x})$ be the function for which one tries to find the minimum. An unconstrained optimization starts by choosing a starting point, an initial guess for the values of the unknown parameters in $f(\mathbf{x})$, \mathbf{x}_0 . A substantial amount of computing time can be saved by choosing \mathbf{x}_0 with some care. In practice one should use whatever information available on the behavior of $f(\mathbf{x})$, so that the initial guess is not far from the stationary point. Once the initial point is chosen, two decisions have to be taken before the next points can be generated.

- (i) One must first pick a direction along which the next point is to be chosen.
- (ii) One must decide on the step size to be taken in that direction.

Then the following iterative procedure has to be considered:

$$\mathbf{x}_{k+1} = \mathbf{x}_k + \lambda_k \mathbf{d}_k \quad k = 0, 1, \dots, \quad (3.2)$$

where \mathbf{d}_k is the direction and $|\lambda_k \mathbf{d}_k|$ is the step size. Different optimization methods differ in the choice of \mathbf{d}_k and λ_k . One can classify these methods in three categories:

- (1) The methods using only the functional values.
- (2) The methods making use of the first-order derivatives.
- (3) The methods which also requires the knowledge of the second-order derivatives.

The first category refers to the nonderivative methods and last two are considered as gradient methods. Category (3) will generally generate points that are sufficiently close to the minimum in the least numbers of steps, however, the computational costs of computing and handling the second derivatives can be substantial. Hence, method (2) is often a preferable method of choice.

For illustrative purpose, a quadratic function of a vector with the form

$$f(\mathbf{x}) = \frac{1}{2} \mathbf{x}^T \mathbf{A} \mathbf{x} + \mathbf{b}^T \mathbf{x} + c, \quad (3.3)$$

is considered. Here, matrix \mathbf{A} is a *positive-definite* matrix, \mathbf{x} and \mathbf{b} are vectors and c is a scalar constant. A matrix \mathbf{A} is positive-definite if, for every nonzero vector \mathbf{x} ,

$$\mathbf{x}^T \mathbf{A} \mathbf{x} > 0. \quad (3.4)$$

The eigenvalues of a positive-definite matrix are all positive.

3.3 Nonderivative Methods

Minimization methods that incorporate only function values generally involve some systematic method to search the configurational space. In coordinate descent methods, the search directions are the standard basis vectors. A sweep through these n search directions produces a sequential modification of one function variable at a time. Through repeated sweeping of the n -dimensional space, a local minimum might ultimately be found.

A well known variant of the basic coordinate descent scheme is Powell's method [85], which is more efficient and reliable. Rather than specifying the search vectors a priori, the standard basis directions are modified as the algorithm progresses. Consider initially n linearly independent directions as coordinate directions $\mathbf{d}_1, \mathbf{d}_2, \dots, \mathbf{d}_n$ starting from the best known approximation to the minimum, \mathbf{x}_0 . The start of the method is identical to an iteration method which changes one parameter at a time. Later the method is modified to generate conjugate directions by making each iteration define a new direction, \mathbf{d} , and choosing the linearly independent directions for the next iterations to be $\mathbf{d}_2, \mathbf{d}_3, \dots, \mathbf{d}_n, \mathbf{d}$. If a quadratic function is being minimized, after k iterations the last k of the n directions chosen for the $k+1$ th iteration are mutually conjugate. Powell's method guaranteed that in exact arithmetic (i.e., in the absence of round off error), the minimum of a convex quadratic function is found after n sweeps.

Nonderivative minimization methods are generally easy to implement but sometimes encounter convergence problems. In general, the computational cost, dominated by the number of function evaluations, can be excessively high for the functions of many variables and can far outweigh the benefit of avoiding derivative calculations. If obtaining the analytic derivatives is difficult, the gradient can be approximated by finite differences of function values, as

$$g_i \approx \frac{1}{h_i} [f(\mathbf{x} + h_i \mathbf{e}_i) - f(\mathbf{x})], \quad (3.5)$$

for suitably chosen intervals h_i .

3.4 Gradient Methods

This class of methods uses the analytic-derivative information, which clearly possess more information about the smooth objective function. Gradient methods can use the slope of a function, for example, as the direction of the movements toward extreme points. The second derivative can also incorporate curvature information from the Hessian to find the regions where the function is convex. The common gradient methods are steepest descent, conjugate gradient, Newton-Raphson methods.

3.4.1 Steepest descent method

The method of steepest descent is the simplest of the gradient methods. In this method one starts at an arbitrary point \mathbf{x}_0 and then take a series of steps to the points $\mathbf{x}_1, \mathbf{x}_2, \dots$ until convergence is achieved. The choice of the descent direction is where f decreases most quickly, which is the direction opposite to $f'(\mathbf{x}_i)$. According to Eq. (3.3), for a quadratic function, this direction is $-\nabla f(\mathbf{x}_i) = -f'(\mathbf{x}_i) = \mathbf{b} - \mathbf{A}\mathbf{x}_i$.

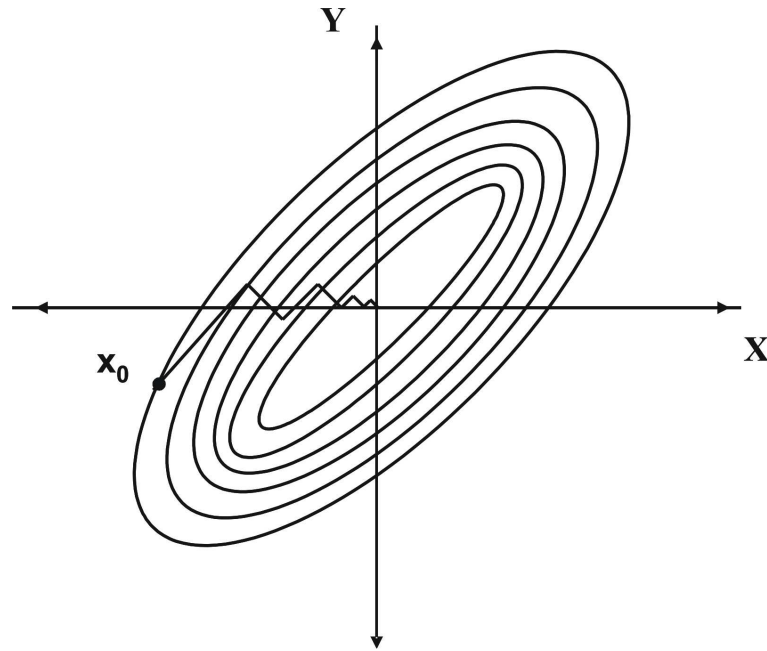


Figure 3.1: The method of steepest descent approaches the minimum in a zig-zag manner, where the new search direction is perpendicular to the previous one. The step size gets smaller and smaller as it approaches the minimum.

Consider the following definitions. The error $\mathbf{e}_i = \mathbf{x}_i - \mathbf{x}$ is the vector that indicates how far the approximate value is away from the solution. The residual $\mathbf{r}_i = \mathbf{b} - \mathbf{A}\mathbf{x}_i = -f'(\mathbf{x}_i)$, indicates the deviation from the correct value of \mathbf{b} which is also the direction of steepest descent. In this method a step is taken from \mathbf{x}_0 according to the equation:

$$\mathbf{x}_{(1)} = \mathbf{x}_0 + \lambda \mathbf{r}_0. \quad (3.6)$$

In order to choose λ a line search procedure is applied. λ minimizes f when the directional derivative $\frac{d}{d\lambda} f(\mathbf{x}_{(1)}) = 0$. By the chain rule $\frac{d}{d\lambda} f(\mathbf{x}_{(1)}) = f'(\mathbf{x}_{(1)}) \frac{d}{d\lambda} \mathbf{x}_{(1)} = f'(\mathbf{x}_{(1)})^T \mathbf{r}_0$. Hence, one finds that λ must be chosen so that \mathbf{r}_0 and $f'(\mathbf{x}_{(1)})$ are or-

thonormal. To determine λ one considers:

$$\begin{aligned}
 -f'(\mathbf{x}_{(1)})^T \mathbf{r}_0 &= 0 \\
 \mathbf{r}_{(1)}^T \mathbf{r}_0 &= 0 \\
 (\mathbf{b} - \mathbf{A}\mathbf{x}_{(1)})^T \mathbf{r}_0 &= 0 \\
 (\mathbf{b} - \mathbf{A}(\mathbf{x}_0 + \lambda \mathbf{r}_0))^T \mathbf{r}_0 &= 0 \\
 (\mathbf{b} - \mathbf{A}\mathbf{x}_0)^T \mathbf{r}_0 &= \lambda (\mathbf{A}\mathbf{r}_0)^T \mathbf{r}_0 \\
 \lambda &= \frac{\mathbf{r}_0^T \mathbf{r}_0}{\mathbf{r}_0^T \mathbf{A}\mathbf{r}_0}.
 \end{aligned} \tag{3.7}$$

Putting it all together the algorithm for the steepest descent is:

$$\mathbf{r}_{(i)} = \mathbf{b} - \mathbf{A}\mathbf{x}_{(i)}, \tag{3.8}$$

$$\lambda_{(i)} = \frac{\mathbf{r}_{(i)}^T \mathbf{r}_{(i)}}{\mathbf{r}_{(i)}^T \mathbf{A}\mathbf{r}_{(i)}}, \tag{3.9}$$

$$\mathbf{x}_{(i+1)} = \mathbf{x}_{(i)} + \lambda_{(i)} \mathbf{r}_{(i)}. \tag{3.10}$$

Fig. 3.1 illustrates the method of steepest descent. This method is very stable, if the minimum points exist. However this method suffers from low convergence problems. For badly scaled systems, the method can end up spending an infinite number of iterations before locating a minimum.

3.4.2 Conjugate gradient method

As seen in the previous subsection, the reason why the method of steepest descent converges slowly is that it has to take a right angle turn after each step, and consequently search in the same direction. The method of conjugate gradient is an attempt to mend this problem by "learning" from experience.

Conjugacy means that two unequal vectors, \mathbf{d}_i and \mathbf{d}_j , are orthogonal with respect to any symmetric positive definite matrix, \mathbf{A} , i.e.,

$$\mathbf{d}_i^T \mathbf{A} \mathbf{d}_j = 0. \tag{3.11}$$

This can be looked upon as a generalization of orthogonality, for which \mathbf{A} is the unity matrix. The idea is to let each search directions \mathbf{d}_i be dependent on other search directions searched to locate a minimum of $f(\mathbf{x})$ through Eq. (3.11). A set of such search directions are referred to as \mathbf{A} -orthogonal, or conjugate set. It will take for a positive definite n -dimensional quadratic function to its minimum point in, at most, n exact linear searches. The method is often referred to as *conjugate directions*.

The best way to visualize the working of conjugate directions is by comparing the space we work in with a stretched space as shown in Fig. 3.2. Fig. 3.2(a) demonstrates

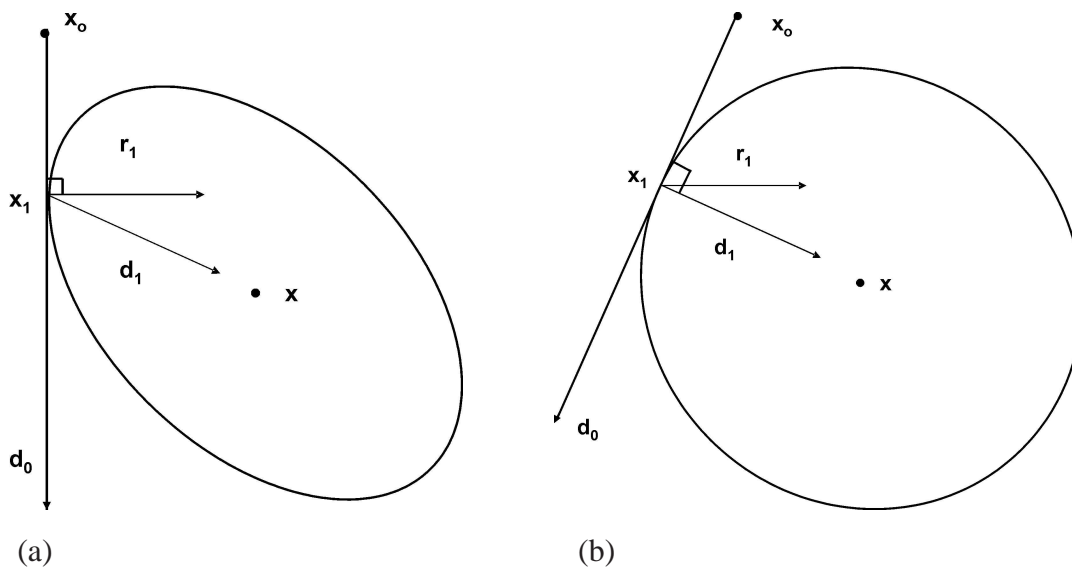


Figure 3.2: The method of conjugate directions. (a) Lines that appear perpendicular are orthogonal. (b) The same problem in a "stretched" space. Lines that appear perpendicular are \mathbf{A} -orthogonal.

the shape of a contour of a quadratic function in real space, which is elliptical (for $\mathbf{b} \neq 0$). Any pair of vectors that appear perpendicular in this space, would be orthogonal. Fig. 3.2(b) shows the same plot in a space that is stretched along the eigenvector axes so that the elliptical contour from Fig. 3.2(a) becomes circular. Any pair of vectors that appears to be perpendicular in this space, is in fact \mathbf{A} -orthogonal. The search for a minimum of the quadratic functions starts at \mathbf{x}_0 and takes a step in the direction \mathbf{d}_0 and stops at \mathbf{x}_1 . This minimum point along that direction, determined by the same way as for the steepest descent method, i.e., the minimum along a line where the directional derivative is zero. The essential difference between the steepest descent and the conjugate direction lies in the choice of the next search from this minimum point. While the steepest descent would search in the direction \mathbf{r}_1 in Fig. 3.2(a), the conjugate direction method would choose \mathbf{d}_1 . In the stretched space, the direction \mathbf{d}_0 appears to be a tangent to the now circular contour at the point \mathbf{x}_1 . Since the next search direction \mathbf{d}_1 is constrained to be \mathbf{A} -orthogonal to the previous, they appear perpendicular in "stretched space". Hence, \mathbf{d}_1 will find directly the minimum point of the quadratic function $f(x)$. To avoid searching in directions that have been searched before, the conjugate direction guarantees that the minimization of the $f(\mathbf{x}_k)$ along one direction does not "spoil" the minimization along another, i.e., after i steps $f(\mathbf{x}_i)$ will be minimized over all searched directions. The conjugate gradient method is a special case of the method of conjugate directions, where the conjugate set is generated by the gradient vectors. This seems to be a good choice since the gradient vectors have proven their applicability in the steepest descent method, and they are orthogonal to

the previous search direction. For a quadratic function, the procedure is as follows.

The initial step is in the direction of the steepest descent:

$$\mathbf{d}_0 = -f'(\mathbf{x}_0) = -\mathbf{g}_0, \quad (3.12)$$

where \mathbf{g} is the gradient. Subsequently, the mutually conjugate directions are chosen so that

$$\mathbf{d}_{k+1} = -\mathbf{g}_{k+1} + \beta_k \mathbf{d}_k \quad k = 0, 1, \dots, \quad (3.13)$$

where the coefficient β_k is given by, for example, the so called Fletcher-Reeves formula:

$$\beta_k = \frac{\mathbf{g}_{k+1}^T \cdot \mathbf{g}_{k+1}}{\mathbf{g}_k^T \cdot \mathbf{g}_k}. \quad (3.14)$$

The step length along the directions is given by

$$\lambda_k = \frac{\mathbf{d}_k^T \cdot \mathbf{g}_k}{\mathbf{d}_k^T \cdot \mathbf{A} \cdot \mathbf{d}_k}, \quad (3.15)$$

and the resulting iterative formula is identical to Eq. (3.2).

The direct use of Eq. (3.15) will most likely not bring us to the solution in n iterations either, the reason being the limited numerical accuracy in the computations which will make the search vectors lose their conjugacy. It should also be mentioned that if the matrix \mathbf{A} is badly scaled, the convergence will be slowed down considerably, as it was for the steepest descent method.

The conjugate gradient method is often employed to problems where the number of variables n is large, and it is not unusual for the method to start generating nonsensical and inefficient directions of search after a few iterations. For this reason it is important to operate the method in cycles, with the first step being the steepest descent step. One example of a restarting policy is to restart with steepest descent step after n iterations after the preceding restart.

3.4.3 Newton-Raphson method

The method of Newton-Raphson differs from the steepest descent and conjugate gradient methods in that the information of the second derivative is used to locate the minimum of a function $f(\mathbf{x})$. This results in faster convergence, but not necessarily less computing time. The computation of the second derivatives and the handling of their matrix can be very time consuming, especially for large systems.

The idea behind the Newton-Raphson method is to approximate the given function $f(\mathbf{x})$ in each iteration by a quadratic function as given in Eq. (3.3) and then move to

the minimum of this quadratic approximation. The quadratic function for a point \mathbf{x} in a suitable neighborhood of the current point \mathbf{x}_k is given by a truncated Taylor series:

$$f(\mathbf{x}) \approx f(\mathbf{x}_k) + (\mathbf{x} - \mathbf{x}_k)^T \cdot \mathbf{g}_k + \frac{1}{2}(\mathbf{x} - \mathbf{x}_k)^T \cdot \mathbf{H}_k \cdot (\mathbf{x} - \mathbf{x}_k), \quad (3.16)$$

where both the gradient \mathbf{g}_k and the Hessian matrix \mathbf{H}_k are evaluated at \mathbf{x}_k . The derivative of Eq. (3.16) is

$$\nabla f(\mathbf{x}) = \mathbf{g}_k + \frac{1}{2}\mathbf{H}_k \cdot (\mathbf{x} - \mathbf{x}_k) + \frac{1}{2}\mathbf{H}_k^T \cdot (\mathbf{x} - \mathbf{x}_k). \quad (3.17)$$

The Hessian is always symmetric if the function $f(\mathbf{x})$ is twice continuously differentiable everywhere. Hence Eq. (3.17) reduces to

$$\nabla f(\mathbf{x}) = \mathbf{g}_k + \mathbf{H}_k \cdot (\mathbf{x} - \mathbf{x}_k). \quad (3.18)$$

If we assume that the function $f(\mathbf{x})$ has a minimum at $\mathbf{x} = \mathbf{x}^*$, the gradient of f is zero, i.e.,

$$\mathbf{H}_k \cdot (\mathbf{x}^* - \mathbf{x}_k) + \mathbf{g}_k = 0, \quad (3.19)$$

which is a linear equations system. The Newton-Raphson method uses the \mathbf{x}^* as the next current point, resulting in the iterative formula,

$$\mathbf{x}_{k+1} = \mathbf{x}_k - \mathbf{H}_k^{-1} \cdot \mathbf{g}_k \quad k = 0, 1, \dots, \quad (3.20)$$

where $\mathbf{H}_k^{-1} \cdot \mathbf{g}_k$ is referred to as the Newton direction. The performance of the method is dependent on certain qualities of the Hessian. One of these qualities is the positive definiteness. If the Hessian is not positive definite, the method is no longer guaranteed to proceed towards a minimum and may end up at other critical points, which may be either saddle point or a maximum point. The size of the Hessian can also be crucial to the effectiveness of the Newton-Raphson method. For systems with a large dimensions, i.e., that the function $f(\mathbf{x})$ has a large number of variables, both the computation of the matrix and the calculations that include it, will be time consuming. This can be mended by either just using the diagonal terms in the Hessian, i.e., ignoring the cross terms or just not recalculating the Hessian at each iteration.

Chapter 4

Solid State Properties

There has been great burst of interest in the subject of amorphous solids, however this area has yet to develop any unifying principles, which can be comparable to that provided by the consequence of a periodic array of atoms or ions. Many of the concepts used in the modeling of amorphous solids are borrowed from the theory of crystalline solids, even though they are only well understood as a consequence of lattice periodicity. In this chapter solid state properties are illustrated with some reference to the crystals. For details refer to Refs. [1, 2, 86, 87, 88, 89]

4.1 Structural Properties

4.1.1 Diffraction by crystals

Usually the structure of solids is studied through the diffraction of photons, neutrons and electrons. The diffraction depends on the structure and on the wavelength. When the wavelength of the radiation is comparable with or smaller than the lattice constant, the diffracted beams are in direction quite different from the incident direction. The famous Bragg's diffraction law, i.e., $2d \sin \theta = n\lambda$, gives the condition for the constructive interference of waves scattered from the lattice points. However, in order to get deeper understanding, one need to determine the scattering intensity from the basis atoms, i.e., the spatial distribution of the electrons.

A crystal is invariant under any translation of the form $\mathbf{T} = u_1\mathbf{a}_1 + u_2\mathbf{a}_2 + u_3\mathbf{a}_3$, where u_1, u_2, u_3 are integers and $\mathbf{a}_1, \mathbf{a}_2, \mathbf{a}_3$ are the crystal axes. The reciprocal lattice

comprises of the primitive axis vectors $\mathbf{b}_1, \mathbf{b}_2, \mathbf{b}_3$, defined as

$$\mathbf{b}_1 = 2\pi \frac{\mathbf{a}_2 \times \mathbf{a}_3}{\mathbf{a}_1 \cdot \mathbf{a}_2 \times \mathbf{a}_3}, \quad (4.1)$$

$$\mathbf{b}_2 = 2\pi \frac{\mathbf{a}_3 \times \mathbf{a}_1}{\mathbf{a}_1 \cdot \mathbf{a}_2 \times \mathbf{a}_3}, \quad (4.2)$$

$$\mathbf{b}_3 = 2\pi \frac{\mathbf{a}_1 \times \mathbf{a}_2}{\mathbf{a}_1 \cdot \mathbf{a}_2 \times \mathbf{a}_3}. \quad (4.3)$$

Each vector in Eq. (4.1)- Eq. (4.3) is orthogonal to two axis vectors of the crystal lattice, thus

$$\mathbf{b}_i \cdot \mathbf{a}_j = 2\pi \delta_{ij}. \quad (4.4)$$

A reciprocal lattice vector, \mathbf{G} is defined as

$$\mathbf{G} = v_1 \mathbf{b}_1 + v_2 \mathbf{b}_2 + v_3 \mathbf{b}_3, \quad (4.5)$$

where v_1, v_2, v_3 are integers.

Any local property of a crystal is invariant under \mathbf{T} . For example, the electron density $n(\mathbf{r})$ is a periodic function of \mathbf{r} and

$$n(\mathbf{r} + \mathbf{T}) = n(\mathbf{r}). \quad (4.6)$$

The Fourier analysis of this function gives

$$n(\mathbf{r}) = \sum_{\mathbf{G}} n_{\mathbf{G}} \exp(i\mathbf{G} \cdot \mathbf{r}), \quad (4.7)$$

and for a set of reciprocal lattice vectors \mathbf{G} . The Fourier coefficients $n_{\mathbf{G}}$ determine the X-ray scattering amplitude. The inversion of Eq. (4.7) gives

$$n_{\mathbf{G}} = V_c^{-1} \int_{cell} dV n(\mathbf{r}) \exp(-i\mathbf{G} \cdot \mathbf{r}), \quad (4.8)$$

where V_c is the volume of a cell in the crystal.

The set of reciprocal lattice vectors \mathbf{G} determines the possible X-ray reflections. The amplitude of the electric or magnetic field vectors in the scattered electromagnetic wave is given by the scattering amplitude, F defined as

$$F = \int dV n(\mathbf{r}) \exp[i(\mathbf{k} - \mathbf{k}') \cdot \mathbf{r}] = \int dV n(\mathbf{r}) \exp(-i\Delta\mathbf{k} \cdot \mathbf{r}), \quad (4.9)$$

where

$$\mathbf{k} + \Delta\mathbf{k} = \mathbf{k}'. \quad (4.10)$$

Here \mathbf{k}, \mathbf{k}' represent the wave vectors of the incident and diffracted waves, respectively. The diffraction condition is given by when the scattering vector $\Delta\mathbf{k}$ is equal to a particular lattice vector, i.e.,

$$\Delta\mathbf{k} = \mathbf{G}. \quad (4.11)$$

Hence, under the diffraction condition, the scattering amplitude for a crystal of N cells is given by

$$F_{\mathbf{G}} = N \int_{cell} dV n(\mathbf{r}) \exp(-i\mathbf{G}\cdot\mathbf{r}) = NS_{\mathbf{G}} \quad (4.12)$$

Here, $S_{\mathbf{G}}$ is called the structure factor and is defined over a single cell. The electron concentration $n(\mathbf{r})$ can be considered as the superposition of electron concentration functions n_j associated with each atom j of the cell. Hence, the structure factor can be written over all atoms of a cell as

$$S_{\mathbf{G}} = \sum_j \int dV n_j(\mathbf{r} - \mathbf{r}_j) \exp(-i\mathbf{G}\cdot\mathbf{r}) = \sum_j \exp(-i\mathbf{G}\cdot\mathbf{r}_j) \int dV n_j(\boldsymbol{\zeta}) \exp(-i\mathbf{G}\cdot\boldsymbol{\zeta}), \quad (4.13)$$

where $\boldsymbol{\zeta} = \mathbf{r} - \mathbf{r}_j$. The atomic form factor is defined as

$$f_j = \int dV n_j(\boldsymbol{\zeta}) \exp(-i\mathbf{G}\cdot\boldsymbol{\zeta}), \quad (4.14)$$

which is integrated over all space. This factor measures the scattering power of the j th atom in the unit cell. Hence, the structure factor is given by

$$S_{\mathbf{G}} = \sum_j f_j \exp(-i\mathbf{G}\cdot\mathbf{r}_j). \quad (4.15)$$

4.1.2 Investigation of structures of non-crystalline solids

In contrast to the situation with crystalline materials, the absence of periodicity means that the structure can no longer be reduced to considering the smallest repeat element, the unit cell. It is only possible to estimate the probability of the distribution of atoms in the vicinity of any reference atom. Diffraction methods can be used to determine the frequency with which given interatomic distances occur in an amorphous sample.

For non-crystalline solids, in Eq. (4.12) instead of writing the structure factor of the basis, one can sum for all the atoms in the specimen. Further, instead of specifying the scattering to the reciprocal lattice vectors \mathbf{G} , one can consider arbitrary scattering vectors $\Delta\mathbf{k} = \mathbf{k}' - \mathbf{k}$. This is done because scattering from amorphous materials is not limited to the reciprocal lattice vectors, which are not defined. Therefore the scattering amplitude from an amorphous material is described by using Eq. (4.12) and Eq. (4.14) as

$$F(\Delta\mathbf{k}) = \sum_j f_j \exp(-i\Delta\mathbf{k}\cdot\mathbf{r}_j). \quad (4.16)$$

Here the summation runs over all the atoms in the material. The scattered intensity at the scattered vector $\Delta\mathbf{k}$ is given by

$$I = F * F^* = \sum_i \sum_j f_i f_j \exp[i\Delta\mathbf{k} \cdot (\mathbf{r}_i - \mathbf{r}_j)]. \quad (4.17)$$

If α is the angle between $\Delta\mathbf{k}$ and $\mathbf{r}_i - \mathbf{r}_j$, then

$$I = \sum_i \sum_j f_i f_j \exp(iKr_{ij} \cos \alpha), \quad (4.18)$$

where K and r_{ij} are the magnitude of $\Delta\mathbf{k}$ and $\mathbf{r}_i - \mathbf{r}_j$, respectively.

In an amorphous specimen the vector $\mathbf{r}_i - \mathbf{r}_j$ may take on all orientations and therefore by averaging the phase factor over a space one obtain the scattered intensity

$$I = \sum_i \sum_j f_i f_j \frac{\sin Kr_{ij}}{Kr_{ij}}. \quad (4.19)$$

For one-component system the scattered intensity is given by

$$I = Nf^2 \sum_j \frac{\sin Kr_{ij}}{Kr_{ij}}, \quad (4.20)$$

where $f_i = f_j = f$ for only one type of atom and N is the number of atoms. With the approximations $r_{ij} \rightarrow 0$, $\sin Kr_{ij}/Kr_{ij} \rightarrow 1$, and with the introduction of the density function $\rho(r)$, this leads to

$$I = Nf^2 \left[1 + \int_0^\infty 4\pi r^2 \rho(r) \frac{\sin Kr}{Kr} dr \right]. \quad (4.21)$$

Here, $\rho(r)$ is the volume density of atoms at distance r from the reference atom, and $4\pi r^2 \rho(r) dr$ is the number of atoms in a spherical shell of radius r and thickness dr . The function $\rho(r)$ is thus essentially a pair correlation function and $4\pi r^2 \rho(r)$ represents *radial distribution function* (RDF), $g(r)$. This function is specially averaged one-dimensional representation of a three-dimensional structure. Introducing ρ_0 , the average density of atoms in the sample investigated, the second integral in the equation

$$I = Nf^2 \left\{ 1 + \int_0^\infty 4\pi r^2 [\rho(r) - \rho_0] \frac{\sin Kr}{Kr} dr + \int_0^\infty 4\pi r^2 \rho_0 \frac{\sin Kr}{Kr} dr \right\} \quad (4.22)$$

can be neglected in the range of values of K acquired in a wide-angle measurement. Amorphous solids possess no long-range order, i.e., the density function $\rho(r)$ tends to ρ_0 . Thus the quantity $[\rho(r) - \rho_0]$ tends to zero at distances greater than a few atom separations and hence the first integral is dominated by the scattering mainly from close scattering centers. The RDF is obtain by the application of the Fourier's integral theorem, which eventually lead to

$$g(r) = 4\pi r^2 \rho(r) = 4\pi r^2 \rho_0 + \frac{2r}{\pi} \int_0^\infty K \left(\frac{I}{Nf^2} - 1 \right) \sin(Kr) dK. \quad (4.23)$$

4.2 Vibrational Properties

The vibrational properties of amorphous solids are very similar to that of the corresponding crystalline forms, with the exception that selection rules for transitions are relaxed and sharp features in the density of vibrational modes are broadened due to lack of periodicity. The next sections are devoted to the discussion of vibrational excitations in crystals followed by anomalous properties shown by amorphous solids. This anomalous nature is more pronounced in the low temperature regime and is quite unique to the non-crystalline phase.

4.2.1 Phonons

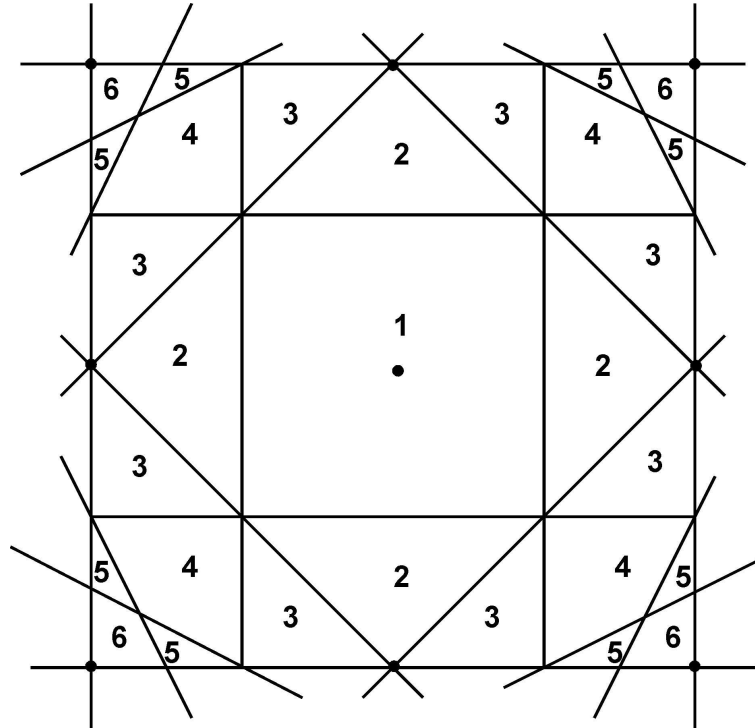


Figure 4.1: The Brillouin zones for a two-dimensional square lattice. The reciprocal lattice is also a square lattice of side b . All Bragg planes (lines, in two dimensions) that lie within the square of side $2b$ centered on the origin. These Bragg planes divide that square into regions belonging to zones 1 to 6. [Adapted from Ref. [88].]

Eq. (4.1)-Eq. (4.3) define the primitive vectors of a reciprocal lattice vector \mathbf{G} . The *first Brillouin zone* is the *Wigner-Seitz* primitive cell of the reciprocal lattice, i.e., the

set of points lying closer to $\mathbf{K} = 0$ than to any other reciprocal lattice point. Since Bragg planes bisect the lines joining the origin to points of the reciprocal lattice, one can equally well define the first zone as the set of points that can be reached from the origin without crossing any Bragg planes. In this definition the points lying on Bragg planes are excluded, which turn out to be common to the surface of the two or more zones. Higher zones are simply other regions bounded by the Bragg planes defined as follows:

The first Brillouin zone is the set of points in reciprocal space that can be reached from the origin without crossing any Bragg plane. The second Brillouin zone is the set of points that can be reached from the first zone by crossing only one Bragg plane. The $(n + 1)$ th Brillouin zone is the set of points not in the $(n - 1)$ th zone that can be reached from the n th zone by crossing only one Bragg plane. These definitions are illustrated in Fig. 4.1 for a simple two-dimensional square lattice. These Brillouin zones are essential for the analysis of vibrational properties for crystals.

Consider elastic vibrations in a crystal. If there are p atoms in the primitive cell, there are $3p$ branches to the dispersion relations: 3 acoustic branches and $3p - 3$ optical ones. The atoms vibrate against each other, but their center of mass is fixed in optical modes. Hence if they are ions, these motions will interact with the electric field of a light wave. However, in acoustical branches the atoms move together along with their center of mass.

Consider a diatomic crystal structure with masses M_1, M_2 connected by force constant C between adjacent planes. The displacements of atom of mass M_1 are denoted by $u_{s-1}, u_s, u_{s+1}, \dots$, and of atoms of mass M_2 by $\vartheta_{s-1}, \vartheta_s, \vartheta_{s+1}$. The repeated distance is a in the direction of the wave vector \mathbf{k} . The equations of motion under the assumption that each plane interacts only with its nearest planes:

$$\begin{aligned} M_1 \frac{d^2 u_s}{dt^2} &= C(\vartheta_s + \vartheta_{s-1} - 2u_s); \\ M_2 \frac{d^2 \vartheta_s}{dt^2} &= C(u_{s+1} + u_s - 2\vartheta_s). \end{aligned} \quad (4.24)$$

One can obtain a solution in the form of a traveling wave with different amplitudes u, ϑ on alternate planes:

$$\begin{aligned} u_s &= u \exp(iska) \exp(-i\omega t); \\ \vartheta_s &= \vartheta \exp(iska) \exp(-i\omega t). \end{aligned} \quad (4.25)$$

Eq. (4.24) and Eq. (4.25) lead to the dispersion relation:

$$M_1 M_2 \omega^4 - 2C(M_1 + M_2)\omega^2 + 2C^2(1 - \cos ka) = 0. \quad (4.26)$$

For the following limiting cases the roots are:

- $ka \ll 1$ (very small values of k).

Case I: $\omega^2 \approx 2C\left(\frac{1}{M_1} + \frac{1}{M_2}\right)$ (optical branch);

Case II: $\omega^2 \approx \frac{C}{2(M_1+M_2)}K^2a^2$ (acoustical branch).

- $ka \pm \pi$ (at the zone boundary).

Case I: $\omega^2 = \frac{2C}{M_2}$ (optical branch, when $M_1 > M_2$);

Case II: $\omega^2 = \frac{2C}{M_1}$ (acoustical branch, when $M_1 > M_2$).

The dependence of ω on k is shown in Fig. 4.2.

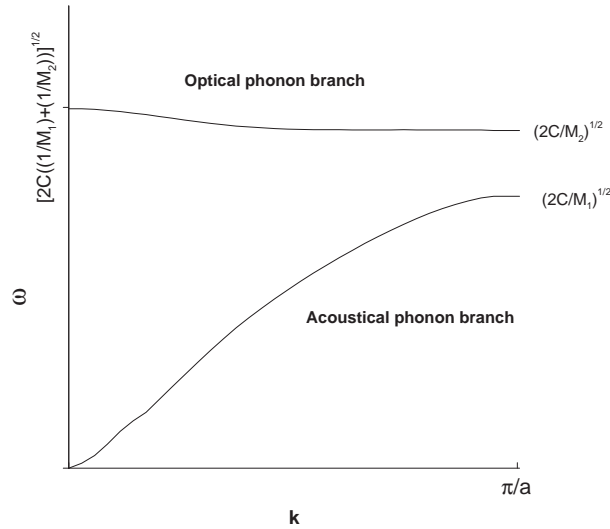


Figure 4.2: Dispersion relation for a diatomic linear lattice with lattice constant a ($M_1 > M_2$), showing the limiting frequencies at $k = 0$ and $k = k_{max} = \pi/a$. [Adapted from Ref. [87]].

4.2.2 Properties under harmonic approximation

In the harmonic approximation the normal modes, i.e., the phonons, are independent. The total wavefunction is the product of the single mode wavefunctions and the total energy and the thermodynamic functions are sums of the single mode contributions. These sums can be expressed as averages over the frequency spectrum, $g(\omega)$, defined such that $g(\omega)d\omega$ is the fraction of eigenfrequencies in the interval $[\omega, \omega + d\omega]$:

$$g(\omega) = \frac{1}{3N} \sum_{\mathbf{k}, j} \delta(\omega - \omega_j(\mathbf{k})) \quad (4.27)$$

and

$$\int_0^{\infty} d\omega g(\omega) = 1. \quad (4.28)$$

At low frequencies the spectrum increases as ω^2 which is a direct consequence of the linear dispersion of the long wavelength acoustic modes. Usually the spectrum shows number of singularities known as *van Hove singularities*, where the derivative $dg(\omega)/d\omega$ is discontinuous. These singularities originate from the extrema of the dispersion curves which are always present due to the periodicity.

The thermodynamic functions can be derived from the partition function

$$Q = \text{tr}\{\exp(-\beta H)\} \quad (4.29)$$

where tr stands for trace, H is the Hamiltonian and $\beta = 1/(k_B T)$ with k_B the Boltzmann constant and T the absolute temperature. In the harmonic approximation the trace can be evaluated for each mode separately, resulting in products of sums over the occupation numbers giving

$$Z = \prod_{\mathbf{k},j} \frac{\exp[-\frac{1}{2}\beta\hbar\omega_j(\mathbf{k})]}{1 - \exp[-\beta\hbar\omega_j(\mathbf{k})]}. \quad (4.30)$$

The Helmholtz free energy per atom is given by:

$$A = -\frac{1}{N}k_B T \ln Z = \frac{1}{N}k_B T \sum_{\mathbf{k},j} \ln\{2 \sinh[\hbar\omega_j(\mathbf{k})/(2k_B T)]\} \quad (4.31)$$

$$= 3k_B T \int d\omega \ln\{2 \sinh[\hbar\omega/(2k_B T)]\} g(\omega). \quad (4.32)$$

Here N represents number of atoms. From this expression the internal energy E , the specific heat at constant volume C_V and the vibrational entropy S per atom, can be calculated by standard thermodynamic relations:

$$E = A - T \left(\frac{\partial A}{\partial T} \right)_V = 3 \frac{\hbar}{2} \int d\omega \coth[\hbar\omega/(2k_B T)] \omega g(\omega). \quad (4.33)$$

$$C_V = \left(\frac{\partial E}{\partial T} \right)_V = 3k_B \int d\omega \left(\frac{\hbar\omega}{2k_B T} \right)^2 \{ \sinh^2[\hbar\omega/(2k_B T)] \}^{-1} g(\omega). \quad (4.34)$$

$$S = - \left(\frac{\partial A}{\partial T} \right)_V = 3k_B \int d\omega \left(\frac{\hbar\omega}{2k_B T} \coth[\hbar\omega/(2k_B T)] - \ln\{2 \sinh[\hbar\omega/(2k_B T)]\} \right) g(\omega). \quad (4.35)$$

At low temperatures the specific heat and entropy obey a $\sim T^3$ law, which is typical for an ordered lattice. In amorphous solids a leading term $\sim T$ is found which is attributed to tunneling centers.

The low temperature behavior can be approximated by the Debye spectrum. At low temperature the thermodynamics will be dominated by the low frequency phonons. The spectrum for low frequency is always proportional to ω^2 , stemming from the linear dispersion for small \mathbf{k} . In the Debye approximation one assumes a purely quadratic behavior of $g(\omega)$ up to a cutoff given by,

$$g_D(\omega) = \begin{cases} \frac{3}{\omega_D^3} \omega^2 & \omega \leq \omega_D \\ 0 & \omega > \omega_D \end{cases} \quad (4.36)$$

The Debye frequency ω_D is often expressed in terms of a Debye temperature Θ_D as

$$k_B \Theta_D = \hbar \omega_D. \quad (4.37)$$

The Debye approximation is valid only for low temperature and the Debye frequency can be determined from the low frequency part of the true spectrum or from the sound velocity.

4.2.3 Anomalies in amorphous systems

Amorphous materials possess no long-range order. Their structure can be visualized as that of a frozen-in liquid. Sound waves, the long wavelength limit of the phonons still exist in these materials. With decreasing wavelength the sound waves will be increasingly scattered by the inhomogeneity on an atomic scale. This damping of the phonons by disorder is always proportional to some power of ω . When the wavelength approaches the atomic scale, a description of the atomic vibrations in terms of phonons (plane waves) is no longer sensible. Nevertheless there are well defined atomic vibrations, but with rather complicated eigenvectors (structure factors). Usually the density of states of these vibrations are similar to their counterpart in crystals. In particular the maxima present for the crystalline form are also found in the amorphous material. The maxima in the density of state of crystal stems from the zone boundary phonons. These phonons probe the short-range order which is more or less preserved in the amorphous phase. Disorder will of course broaden all features.

At low temperatures the properties of amorphous systems differ significantly from those of crystals [90]. Best known is the anomalous low temperature behavior of the specific heat. In crystals $C_V \propto T^3$ and the proportionality constant is determined by the sound velocities. In amorphous materials for example in glasses there are additional contributions to the specific heat. Below $T \approx 2$ K the specific heat increases approximately linearly with T . At $T \approx 2$ K there is a crossover to T^5 dependence. The linear part in the specific heat is attributed to two-level systems, i.e., certain groups of atoms can be envisaged as tunneling between two minimum configurations [91, 92]. The anomaly in the specific heat above 2K are attributed to the localized soft harmonic vibrations [93]. A common description of the two-level systems and the soft vibrations was proposed in the soft potential model [94]. Refer references [94, 95, 97, 96]

for details. This model assumes that, for some reaction coordinate, disorder weakens the harmonic restoring force due to local strains. For sufficiently large local strains the original configuration can even become unstable, and the minimum configuration turns into a maximum. Eventually, the always present anharmonic terms stabilize the configuration in new minima on either side of the maximum. The maximum with two adjoining minima forms a two-well system in the reaction coordinate. The simplest description of such a scenario is given by the quartic potential,

$$V(x) = \varepsilon[\eta(x/a)^2 + t(x/a)^3 + (x/a)^4]. \quad (4.38)$$

Here the scale factor a is an atomic length, about half the nearest neighbor distance. For $x = a$ and $\eta = 1$ the quadratic and quartic parts of the potential are equal. In this formulation of the model the energy scale factor ε is equal to the value for the potential of a single atom, ε_a , times the number of atoms participating in the mode, N_s . To ensure that in the two well case Eq. (4.38) represents an expansion around the maximum, η has to be restricted to $\eta < \frac{9}{32}t^2$. Depending on the parameters, Eq. (4.38) describes a variety of situations.

Consider first the pure symmetric case ($t = 0$). For $\eta \approx 1$, $V(x)$ is a good approximation of a harmonic potential, and x describes a vibrational degree of freedom. For $\eta < 0$ we have a two-well potential with a maximum at $x = 0$ and minima at $x = \pm\sqrt{-\eta/2}$. For larger negative values of η , when both minima are clearly developed but their distance and the barrier separating them are not too large, tunneling transition from one minimum to the other becomes important. In the energy scheme this corresponds to a splitting of the ground state level of one minimum into a symmetric and an antisymmetric state regarding both minima, i.e., one has a two-level system. The higher excited states are not important at the low temperatures considered. For yet larger negative value of η , i.e., increasing the separation of the minima and higher barriers, the tunnel splitting goes to 0 and only thermally activated transitions from one minimum to other are possible (relaxations). The asymmetry of the potential for $t \neq 0$ changes the boundaries of the different regimes. For example a larger value of t suppresses the influence of the second minimum.

In this model two- and one-well model are described, causing two-level systems and soft vibrations, respectively, by a common distribution. A fit of the potential to the experimental data gives numbers of 20 to 80 atoms participating in the tunneling and the soft vibrations [97, 98]. The soft vibrations occur around atoms whose local environment differs from the average one.

4.3 Elastic Constants

The elastic constants are of interest because of the insight they give into the nature of the binding forces in solids, and they are also of importance for the thermal properties of solids. Polycrystalline and amorphous solids have isotropic elastic properties

and may be approximately described by fewer elastic constants than a single crystal. However the knowledge of the constants for single crystals are of fundamental significance. The elastic properties of a crystal are generally anisotropic and defined in terms of tensors.

4.3.1 Elastic strains and stresses

Consider three orthogonal axes $\mathbf{f}, \mathbf{g}, \mathbf{h}$ of unit length, embedded in an unstrained solid. After a small uniform deformation the axes distort to $\mathbf{f}', \mathbf{g}', \mathbf{h}'$, such as,

$$\begin{aligned}\mathbf{f}' &= (1 + \epsilon_{xx})\mathbf{f} + \epsilon_{xy}\mathbf{g} + \epsilon_{xz}\mathbf{h}; \\ \mathbf{g}' &= \epsilon_{yx}\mathbf{f} + (1 + \epsilon_{yy})\mathbf{g} + \epsilon_{yz}\mathbf{h}; \\ \mathbf{h}' &= \epsilon_{zx}\mathbf{f} + \epsilon_{zy}\mathbf{g} + (1 + \epsilon_{zz})\mathbf{h}.\end{aligned}\quad (4.39)$$

The fractional changes of length of \mathbf{f}, \mathbf{g} and \mathbf{h} are $\epsilon_{xx}, \epsilon_{yy}, \epsilon_{zz}$, respectively. The strain components are defined as

$$e_{xx} = \epsilon_{xx} \quad e_{yy} = \epsilon_{yy} \quad e_{zz} = \epsilon_{zz}.\quad (4.40)$$

The other non-diagonal component of the strain may be defined as the changes in the angle between the axes and considering only the linear terms as,

$$\begin{aligned}e_{xy} &= \mathbf{f}' \cdot \mathbf{g}' \approx \epsilon_{yx} + \epsilon_{xy}; \\ e_{yz} &= \mathbf{g}' \cdot \mathbf{h}' \approx \epsilon_{zy} + \epsilon_{yz}; \\ e_{zx} &= \mathbf{h}' \cdot \mathbf{f}' \approx \epsilon_{zx} + \epsilon_{xz}.\end{aligned}\quad (4.41)$$

Using Eq. (4.40) and Eq. (4.41), Eq. (4.39) becomes

$$\begin{aligned}\mathbf{f}' - \mathbf{f} &= e_{xx}\mathbf{f} + \frac{1}{2}e_{xy}\mathbf{g} + \frac{1}{2}e_{zx}\mathbf{h}; \\ \mathbf{g}' - \mathbf{g} &= \frac{1}{2}e_{xy}\mathbf{f} + e_{yy}\mathbf{g} + \frac{1}{2}e_{yz}\mathbf{h}; \\ \mathbf{h}' - \mathbf{h} &= \frac{1}{2}e_{zx}\mathbf{f} + \frac{1}{2}e_{yz}\mathbf{g} + e_{zz}\mathbf{h}.\end{aligned}\quad (4.42)$$

Consider a particle at the position

$$\mathbf{r} = x\mathbf{f} + y\mathbf{g} + z\mathbf{h}.\quad (4.43)$$

After the deformation the displacement is given by

$$\rho = x(\mathbf{f}' - \mathbf{f}) + y(\mathbf{g}' - \mathbf{g}) + z(\mathbf{h}' - \mathbf{h}).\quad (4.44)$$

One can write the displacement as

$$\rho = u\mathbf{f} + v\mathbf{g} + w\mathbf{h},\quad (4.45)$$

where the expression for the strain components as:

$$e_{xx} = \frac{\partial u}{\partial x}; \quad e_{yy} = \frac{\partial v}{\partial y}; \quad e_{zz} = \frac{\partial w}{\partial z}; \quad (4.46)$$

$$e_{xy} = \frac{\partial v}{\partial x} + \frac{\partial u}{\partial y}; \quad e_{yz} = \frac{\partial w}{\partial y} + \frac{\partial v}{\partial z}; \quad e_{zx} = \frac{\partial u}{\partial z} + \frac{\partial w}{\partial x}. \quad (4.47)$$

The strain component of the type e_{xy} as given in Eq. (4.47) can be interpreted as made up two simple shears. In one of the shears, planes of the material normal to the x axis slide in y direction; in the other shear, planes normal to y slide in x direction

4.3.2 Stress components

The force acting on a unit area in the solid is defined as the stress. There are nine stress components: $X_x, X_y, X_z, Y_x, Y_y, Y_z, Z_x, Z_y, Z_z$. The capital letter indicates the direction of the force, and the subscript indicates the normal to the plane to which the force is applied. Thus the stress component X_x represents a force applied in the x direction to a unit area of a plane whose normal lies in the x direction. The number of independent stress components is reduced to six by applying the condition that the angular acceleration vanish, and hence that the total torque must be zero. Therefore, it follows that

$$Y_z = Z_y; \quad Z_x = X_z; \quad X_y = Y_x;$$

and the independent stress components may be taken as $X_x, Y_y, Z_z, Y_z, Z_x, X_y$.

4.3.3 Elastic compliance and stiffness constants

Hooke's law states that for small deformations the strain is proportional to the stress. Hence, the strain components are proportional to the stress components:

$$\begin{aligned} e_{xx} &= s_{11}X_x + s_{12}Y_y + s_{13}Z_z + s_{14}Y_z + s_{15}Z_x + s_{16}X_y; \\ e_{yy} &= s_{21}X_x + s_{22}Y_y + s_{23}Z_z + s_{24}Y_z + s_{25}Z_x + s_{26}X_y; \\ e_{zz} &= s_{31}X_x + s_{32}Y_y + s_{33}Z_z + s_{34}Y_z + s_{35}Z_x + s_{36}X_y; \\ e_{yz} &= s_{41}X_x + s_{42}Y_y + s_{43}Z_z + s_{44}Y_z + s_{45}Z_x + s_{46}X_y; \\ e_{zx} &= s_{51}X_x + s_{52}Y_y + s_{53}Z_z + s_{54}Y_z + s_{55}Z_x + s_{56}X_y; \\ e_{xy} &= s_{61}X_x + s_{62}Y_y + s_{63}Z_z + s_{64}Y_z + s_{65}Z_x + s_{66}X_y; \end{aligned} \quad (4.48)$$

Conversely, the stress components are linear functions of the strain components:

$$\begin{aligned}
 X_x &= c_{11}e_{xx} + c_{12}e_{yy} + c_{13}e_{zz} + c_{14}e_{yz} + c_{15}e_{zx} + c_{16}e_{xy}; \\
 Y_y &= c_{21}e_{xx} + c_{22}e_{yy} + c_{23}e_{zz} + c_{24}e_{yz} + c_{25}e_{zx} + c_{26}e_{xy}; \\
 Z_z &= c_{31}e_{xx} + c_{32}e_{yy} + c_{33}e_{zz} + c_{34}e_{yz} + c_{35}e_{zx} + c_{36}e_{xy}; \\
 Y_z &= c_{41}e_{xx} + c_{42}e_{yy} + c_{43}e_{zz} + c_{44}e_{yz} + c_{45}e_{zx} + c_{46}e_{xy}; \\
 Z_x &= c_{51}e_{xx} + c_{52}e_{yy} + c_{53}e_{zz} + c_{54}e_{yz} + c_{55}e_{zx} + c_{56}e_{xy}; \\
 X_y &= c_{61}e_{xx} + c_{62}e_{yy} + c_{63}e_{zz} + c_{64}e_{yz} + c_{65}e_{zx} + c_{66}e_{xy};
 \end{aligned} \tag{4.49}$$

The quantities s_{11}, s_{12}, \dots are called the elastic constants or elastic compliance constants; the quantities c_{11}, c_{12}, \dots are called the elastic stiffness constants or moduli of elasticity. The matrix of c 's or s 's is symmetrical, therefore thirty-six constants are reduced to twenty-one coefficients for each case. These numbers are further reduced depending on the symmetry of the crystal.

Chapter 5

Quantum Chemical Treatment of Solids

5.1 Overview of Quantum Chemical Methods

Quantum mechanics is the correct mathematical description of the behaviors of electrons and thus of chemistry. In practice, quantum mechanical equations have only been solved exactly for one electron systems. There exist a collection of methods for approximating the solution for multiple electron systems. Refer to Refs. [84,99,100,101] for details. The following sections deals with the discussion of few of the methods.

5.1.1 The Hartree-Fock method

The Hartree-Fock (HF) approximation is a starting point for more accurate methods which includes the effect of electron correlation. HF theory is a single determinant theory, where one is interested in finding a set of spin orbitals χ_a such that the determinant formed from these spin orbitals,

$$|\Psi\rangle = |\chi_1\chi_2\cdots\chi_a\chi_b\cdots\chi_N\rangle, \quad (5.1)$$

is the best possible approximation to the ground state of the N -electron system that is described by an electronic Hamiltonian H_e , as given in Eq. (2.2). In the following discussions the subscript "e" is dropped as the discussion is only about electronic Hamiltonian and electronic wavefunction. The non-relativistic N -electron Hamiltonian under the Born-Oppenheimer approximation is given by

$$H = \sum_i h(i) + \sum_{i<j} v(i,j). \quad (5.2)$$

Here h_i is the one-electron term

$$h(i) = -\frac{1}{2}\nabla_i^2 - \sum_A \frac{Z_A}{r_{iA}}, \quad (5.3)$$

describes the kinetic energy and the electron-nucleus Coulombic interaction of i th electron. $v(i, j)$ is a two-electron term

$$v(i, j) = \frac{1}{r_{ij}}, \quad (5.4)$$

describes the Coulomb repulsion between the electrons i and j . According to the variational principle the "best" spin orbitals are those which minimizes the electronic energy

$$E_0 = \langle \Psi | H | \Psi \rangle = \sum_a \langle a | h | a \rangle + \frac{1}{2} \sum_{ab} \langle ab | ab \rangle. \quad (5.5)$$

The spin orbitals are varied, constraining them only to the extent that they remain orthogonal until E_0 is minimum. This procedure leads to the HF integro-coupled-differential equation

$$F(i)|\chi_i\rangle = \varepsilon_i|\chi_i\rangle, \quad (5.6)$$

where ε_i represent the orbital energy. F is the Fock operator given by

$$F(i) = h(i) + \sum_b J_b(i) - \sum_b K_b(i). \quad (5.7)$$

The J and K represent Coulomb and exchange operators, respectively, and are defined as

$$J_b(\mathbf{r})\chi_a(\mathbf{r}) = \left[\int d\mathbf{r}' \chi_b^*(\mathbf{r}') \frac{1}{|\mathbf{r}-\mathbf{r}'|} \chi_b(\mathbf{r}') \right] \chi_a(\mathbf{r}) \quad (5.8)$$

$$K_b(\mathbf{r})\chi_a(\mathbf{r}) = \left[\int d\mathbf{r}' \chi_b^*(\mathbf{r}') \frac{1}{|\mathbf{r}-\mathbf{r}'|} \chi_a(\mathbf{r}') \right] \chi_b(\mathbf{r}) \quad (5.9)$$

Eq. (5.6) can be interpreted as a set of effective one-electron Schrödinger equations for the orbitals. They are often referred to as the *canonical Hartree-Fock equations*. The corresponding orbitals are the canonical HF orbitals, and the eigenvalues are referred to as orbital energies.

5.1.2 Electron correlation methods

In the HF approximation, one solves equations for the behaviors of each electron in the averaged field of the remaining $(n-1)$ electrons. In reality, however, the electronic

motion occur according to the actual position of other electrons. The Coulomb repulsion between electrons reduces sufficiently only when a correlated motion of the electronic system takes place. This aspect of the electronic motion is absent in the HF approximation. A correlation hole is missing around every electron which prevent other electrons from coming too close. Consequently, the correlation energy of a system is defined as the difference between the exact energy and the HF energy.

However, there exist several theoretical methods for treating the electron correlation problem. One of the formally simplest theoretical method is full configuration interaction (FCI) method in which wavefunction is the best linear combination of all possible configuration state functions within a given basis set. FCI is practically impossible if there are more than a few electrons in the system. The CI wavefunction is usually truncated to singles and doubles substitution and referred as singles and doubles CI (CISD) method. In the following sections other methods like Second-order Møller-Plesset perturbation theory and coupled-cluster theory are described.

5.1.2.1 Second-order Møller-Plesset Perturbation Theory

The simplest electron correlation method is Møller-Plesset perturbation theory [102], which is a special variant of Rayleigh-Schrödinger perturbation theory (RSPT). In this method, the Hamiltonian operator of a N -electron system is divided into two parts, an unperturbed Hamiltonian H_0 and a perturbation λH_1

$$H = H_0 + \lambda H_1. \quad (5.10)$$

The wavefunction and energy are also expanded in a similar way and it is assumed that the zeroth-order wavefunction Ψ_0 is an eigenfunction of H_0 with eigenvalue E_0 ;

$$\Psi = \Psi_0 + \lambda \Psi_1 + \lambda^2 \Psi_2 + \dots \quad (5.11)$$

$$E = E_0 + \lambda E_1 + \lambda^2 E_2 + \dots \quad (5.12)$$

By inserting Eq. (5.10)- Eq. (5.12) into Schrödinger equation and collecting terms of the same order in λ we get the following hierarchy of equations up to second order:

$$H_0 \Psi_0 = E_0 \Psi_0 \quad (5.13)$$

$$(H_0 - E_0) \Psi_1 = (E_1 - H_1) \Psi_0 \quad (5.14)$$

$$(H_0 - E_0) \Psi_2 = (E_1 - H_1) \Psi_1 + E_2 \Psi_0. \quad (5.15)$$

One can assume that the perturbed wavefunctions are orthogonal to the zeroth-order function, which leads to the so-called intermediate normalization of the total wavefunction $\langle \Psi | \Psi_0 \rangle = 1$. Using this the following expressions of the energies up to second order is obtained:

$$E_0 = \langle \Psi_0 | H_0 | \Psi_0 \rangle \quad (5.16)$$

$$E_1 = \langle \Psi_0 | H_1 | \Psi_0 \rangle \quad (5.17)$$

$$E_2 = \langle \Psi_0 | H_1 | \Psi_1 \rangle \quad (5.18)$$

In the Møller-Plesset perturbation (MP2) theory the unperturbed Hamiltonian is chosen to be a sum of Fock-operators acting on the electron. Hence, the zeroth-order energy is the sum of the orbital energies for the occupied spin orbitals. It follows that the sum of the zeroth- and first-order energy equals the HF energy. In order to solve the first-order equation, we expand the first-order wavefunction in determinants Φ_μ :

$$\Psi_1 = \sum_{\mu} C_{\mu} \Phi_{\mu} \quad (5.19)$$

where in case of MP2 the sum runs over excited determinants with respect to the HF ground state. All Φ_μ are eigenfunctions of H_0 with eigenvalues E_μ equal to the sum of the orbital energies of the spin-orbitals occupied in the given determinant. By substituting Eq. (5.19) into Eq. (5.15), we get the following expression of the first-order expansion coefficients:

$$C_{\mu} = - \frac{\langle \Phi_{\mu} | H_1 | \Psi_0 \rangle}{E_{\mu} - E_0} \quad (5.20)$$

The numerator contains the interaction between the configuration Φ_μ and the HF reference function, hence, only those configurations, for which the element is non-zero need to be included. Singly excited configurations will not contribute due to the Brillouin theorem. Thus, the second-order energy is given by:

$$E_2 = - \sum_{i>j} \sum_{a>b} \frac{|\langle \Psi_0 | H_1 | \Phi_{ij}^{ab} \rangle|^2}{e_a + e_b - e_i - e_j}, \quad (5.21)$$

where i, j and a, b are occupied and virtual spin-orbitals, respectively. The applicability of MP2 is restricted to cases with a sufficient large HOMO-LUMO gap. If this is not the case then the energy denominators in Eq. (5.21) become small and the perturbation expansion diverges.

5.1.2.2 Coupled Cluster Method

The coupled cluster (CC) method has emerged in recent years as a powerful tool for treating electron correlation to high accuracy for small- to medium-sized atoms and molecules [103]. The advantage of this method is the size-extensivity irrespective of the truncation of the excitation level is employed. In CC theory the wavefunction is generated by an exponential excitation operator

$$\Psi^{CC} = \exp(\hat{T})\phi^{SCF}, \quad (5.22)$$

where the exponential excitation operator is defined by the Taylor expansion

$$\exp(\hat{T}) = 1 + \hat{T} + \frac{1}{2!} \hat{T} \hat{T} + \frac{1}{3!} \hat{T} \hat{T} \hat{T} + \dots \quad (5.23)$$

The excitation operator may be decomposed into single, double, and possibly higher excitation operators

$$\hat{T} = \hat{T}_1 + \hat{T}_2 + \dots \quad (5.24)$$

with

$$\hat{T}_N = \left(\frac{1}{N!}\right)^2 \sum_{ij\dots ab\dots}^N t_{ij\dots}^{ab\dots} a_a^\dagger a_b^\dagger \dots a_j a_i. \quad (5.25)$$

Here i, j, \dots and a, b, \dots refer to the occupied and unoccupied orbitals in reference determinant, respectively. a_a^\dagger and a_i refer to creation and annihilation operators. The operator \hat{T} is usually truncated after double excitations which defines the coupled-cluster singles and doubles (CCSD) method and wavefunction becomes [104, 105].

$$\Psi_{CCSD} = \exp(\hat{T}_1 + \hat{T}_2)\phi_{SCF}. \quad (5.26)$$

If we insert this wavefunction ansatz into the Schrödinger equation

$$(H - E_{CCSD})\Psi_{CCSD} = (H - E_{CCSD})\exp(\hat{T}_1 + \hat{T}_2)\phi_{SCF} = 0 \quad (5.27)$$

then projecting against the reference, singly and doubly excited states, we obtain a set of equations sufficient for determining the t_i^a and t_{ij}^{ab} coefficients:

$$\langle \phi_{SCF} | (H - E_{CCSD})(1 + \hat{T}_1 + \hat{T}_2 + \frac{1}{2}\hat{T}_1^2) | \phi_{SCF} \rangle = 0 \quad (5.28)$$

$$\langle \phi_i^a | (H - E_{CCSD})(1 + \hat{T}_1 + \hat{T}_2 + \frac{1}{2}\hat{T}_1^2 + \hat{T}_1\hat{T}_2 + \frac{1}{3!}\hat{T}_1^3) | \phi_{SCF} \rangle = 0 \quad (5.29)$$

$$\langle \phi_{ij}^{ab} | (H - E_{CCSD})(1 + \hat{T}_1 + \hat{T}_2 + \frac{1}{2}\hat{T}_1^2 + \hat{T}_1\hat{T}_2 + \frac{1}{3!}\hat{T}_1^3 + \frac{1}{2}\hat{T}_2^2 + \frac{1}{4!}\hat{T}_1^4) | \phi_{SCF} \rangle = 0. \quad (5.30)$$

The expansion on the right-hand side terminate after the quadruple excitations since the Hamiltonian can couple only configurations that differ by at most two excitations. The number of equations corresponds exactly to the number of coefficients. The computational cost of this method rises asymptotically with the sixth power of the basis set dimension. The accuracy of the CCSD calculations can be significantly improved by subsequently computing the effects of higher order excitations through RSPT based on Fock Hamiltonian and the computed CCSD amplitude of single and double excitations. The most widely used ansatz of this type, usually denoted by CCSD(T) [106].

5.1.3 Density functional theory

Density functional theory (DFT) is probably the most often used approach of computational chemistry [107]. In the following the basic idea behind DFT is presented.

In the year 1964 Hohenberg and Kohn presented two fundamental theorems [108] which gave birth to modern DFT, an alternative approach to deal with many body problem in electronic structure theory.

The first Hohenberg-Kohn theorem states that: The external potential $V_{ext}(\mathbf{r})$ is a unique functional of electron density $\rho(\mathbf{r})$; since, in turn $V_{ext}(\mathbf{r})$ fixes H we see that the full many particle ground state is a unique functional of $\rho(\mathbf{r})$. In other words: there is a unique relationship between the external potential $V_{ext}(\mathbf{r})$ (arising from the positive charges of the nuclei) within a N electron system and its (ground state) electron density $\rho(\mathbf{r})$.

Since the complete ground state energy E_0 is a unique functional of the density ρ , so must be its individual parts, i.e.,

$$E_0[\rho] = T[\rho] + V_{int}[\rho] + V_{ext}[\rho]. \quad (5.31)$$

This expression can be classified by parts dependent on the actual system (determined by the external potential) and parts which are universal in the sense that the form of the functional is independent of N , R_A and Z_A .

$$E_0[\rho] = \underbrace{V_{ext}[\rho]}_{\text{System dependent}} + \underbrace{T[\rho] + V_{int}[\rho]}_{\text{System independent}} \quad (5.32)$$

where the system-independent part defines the *Hohenberg-Kohn* functional

$$F_{HK}[\rho] = T[\rho] + V_{int}[\rho]. \quad (5.33)$$

The second Hohenberg-Kohn theorem is nothing else than the variational principle formulated for densities. Given any density $\bar{\rho}$ associated to a N electron system with the external potential V_{ext} , one can state that

$$E_0 \leq E[\bar{\rho}] = T[\bar{\rho}] + V_{int}[\bar{\rho}] + V_{ext}[\bar{\rho}] \quad (5.34)$$

with the equal sign only valid if $\bar{\rho} = \rho$.

Further the Hohenberg-Kohn functional can be identified as

$$F_{HK} = T + V_{ee} \quad (5.35)$$

with potential energy term

$$V_{ee} = \frac{1}{2} \int \int \frac{\rho(\mathbf{r}_1)\rho(\mathbf{r}_2)}{r_{12}} d\mathbf{r}_1 d\mathbf{r}_2 + E_{NCL}(\rho) = J(\rho) + E_{NCL}(\rho). \quad (5.36)$$

Here $J(\rho)$ is the classical interaction of two charge densities and $E_{NCL}(\rho)$ contains all the non-classical parts. Thus, the complete energy functional can be written as

$$E[\rho] = \underbrace{T[\rho]}_{\text{unknown}} + \underbrace{J[\rho]}_{\text{known}} + \underbrace{E_{NCL}[\rho]}_{\text{unknown}} + \underbrace{\int V_{ext}\rho(\mathbf{r})d\mathbf{r}}_{\text{known}}. \quad (5.37)$$

The solution to the problem of unknown functional for kinetic energy was given by Kohn and Sham [109]. They suggested to formally split this functional into two parts

$$T[\rho] = T_S[\rho] + T_C[\rho], \quad (5.38)$$

where $T_S[\rho]$ is expressed in a one particle approach similar to Hartree-Fock method, thus being well known, and the second part, still unknown part contains the difference between the real functional $T[\rho]$ and the one particle term $T_S[\rho]$, and will be treated, as well as the other, remaining parts of the total energy functional, which are still unknown, in an approximate way. Thus one can write

$$E[\rho] = T_S[\rho] + J[\rho] + V_{ext}[\rho] + E_{NCL}[\rho] + T_C[\rho], \quad (5.39)$$

$$= T_S[\rho] + J[\rho] + V_{ext}[\rho] + E_{XC}[\rho]. \quad (5.40)$$

Here the *exchange-correlation functional* $E_{XC}[\rho]$ remains unknown and the rest are well defined terms. T_S is defined as

$$T_S[\rho] = -\frac{1}{2} \sum_i \langle \phi_i | \nabla^2 | \phi_i \rangle \quad (5.41)$$

where the ϕ_i are one particle wavefunction which are determined similar to the Hartree-Fock theory, by applying the variational principle, which leads finally to the *Kohn-Sham equations*

$$\hat{f}^{KS} \phi_i = e_i \phi_i \quad (5.42)$$

with the *Kohn-Sham operator*

$$\hat{f}^{KS} = -\frac{1}{2} \nabla^2 + \int \frac{\rho(\mathbf{r}_2)}{r_{12}} d\mathbf{r}_2 + V_{XC}(\mathbf{r}_1) + \sum_A \frac{Z_A}{r_{1A}}. \quad (5.43)$$

All that remains is the question how to derive the exchange-correlation functional. This term has to be treated on a approximative manner. There exist different functionals, most of them are derived from the electron density of a uniform electron gas, which can be calculated by means of statistical thermodynamics.

Local density approximation (LDA): Within the local density approximation one assumes the density functional of a N particle system can be expressed in the form:

$$E_{XC}^{LDA}[\rho] = \int \rho(\mathbf{r}) \epsilon_{XC}(\rho(\mathbf{r})) d\mathbf{r}, \quad (5.44)$$

where $\epsilon_{XC}(\rho(\mathbf{r}))$ is the exchange-correlation energy per particle of a uniform gas. This quantity can be further split into:

$$\epsilon_{XC}(\rho(\mathbf{r})) = \epsilon_X(\rho(\mathbf{r})) + \epsilon_C(\rho(\mathbf{r})). \quad (5.45)$$

The exchange part can be derived analytical as

$$\epsilon_X(\rho(\mathbf{r})) = -\frac{3}{4} \left(\frac{3\rho(\mathbf{r})}{\pi} \right)^{1/3}. \quad (5.46)$$

The correlation part can not be derived analytically, but can be calculated numerically with high accuracy by means of quantum Monte Carlo simulations.

Gradient corrected functionals: Although the LDA approximation works quite well for certain systems, one cannot expect it to perform well for those classes of molecules most chemists are interested in. This is mainly due to the fact that the electron distribution within a molecule is far from being uniform. Thus the logical step is to improve LDA is to construct functionals which depend not only on the density ρ but also on its gradient $\nabla\rho$, i.e.,

$$E_{XC}^{GC} = E_{XC}^{GC}[\rho, \nabla\rho]. \quad (5.47)$$

5.2 Ab Initio Treatment of Periodic System

Most *ab initio* electronic structure calculations of solids are based on DFT, with the deficiency that no systematic improvement towards the exact result is possible. On the other hand, in the wavefunction-based methods, one improves the calculation systematically by enlarging the basis set and by including more terms in the expansion of the wavefunction, however, at the price of a considerably higher computational cost.

A typical quantum-chemical investigation of solids, employing a wavefunction based approach, begins with a HF calculations and then subsequently improved by considering virtual excitations from the HF wavefunction in order to account for the electron correlations. In order to solve the HF problem for the infinite periodic system, there exist mainly two kind of approaches, i.e., using Bloch and Wannier orbitals. Bloch orbitals are usually delocalized over the whole crystal lattice, whereas Wannier orbitals are localized and these are related by a unitary transformation. In the following sections these methods are described along with a discussion of another kind of approach based on finite cluster. Refer to Refs. [110, 111] for details.

5.2.1 The finite-cluster approaches

5.2.1.1 A simple approach

This approach is well suited for the polymeric kind of system. In this approach the total energy E_{tot} or correlation energy E_{corr} per unit cell U of a polymer U_∞ can be

obtained as the limit

$$E = \lim_{n \rightarrow \infty} \frac{E(R(U_n)R')}{n}, \quad (5.48)$$

i.e., by performing calculations for increasing long oligomers $R(U_n)R'$, where dangling bonds at the end of the polymer are saturated by groups R and R' . In order to reduce finite-size effect due to end group saturation, one can consider

$$E = \lim_{n \rightarrow \infty} \Delta E_n = \lim_{n \rightarrow \infty} \left[E(R(U_{n+1})R') - E(R(U_n)R') \right] \quad (5.49)$$

i.e., the energy changes between two oligomers differing just by a single unit cell. The convergence of ΔE_n with respect to the number of unit cells is much faster for the dynamical correlation energy than for the HF energy, due to the local character of electron correlations. One can use Bloch or Wannier orbital approach for the calculation of the long-range HF energy.

5.2.1.2 Incremental approach

In the incremental approach using localized orbitals, the correlation energy per unit cell is expanded as

$$E_{corr} = \sum_i \varepsilon_i + \sum_{i < j} \Delta \varepsilon_{ij} + \sum_{i < j < k} \Delta \varepsilon_{ijk} + \dots, \quad (5.50)$$

where the summation over i involves localized orbitals in the reference cell, while those over j and k include all the localized orbitals of the crystal. The "one-body" increments $\varepsilon_i = \Delta \varepsilon_i$ are calculated by correlating each of the localized orbitals in turn, while others are kept frozen at the HF level. The "two-body" increments are determined by considering pair of bonds and performing correlated calculations for each chosen pair. Excitations are allowed only from the orbitals belonging to this pair, keeping the rest of the orbitals frozen. Hence the "two-body" increments $\Delta \varepsilon_{ij}$ are defined as $\Delta \varepsilon_{ij} = \varepsilon_{ij} - (\varepsilon_i + \varepsilon_j)$, where ε_{ij} is the correlation energy obtained by correlating orbitals i and j . Higher-order increments are defined in an analogous way. Finally, adding all increments, with the proper weight factors determined by the occurrence in the unit cell, one obtains the exact correlation energy per unit cell of the infinite system as given in Eq. (5.50). The procedure described above only makes sense, if the incremental expansion is well convergent and can be truncated at low order increments, e.g., after second or third sum. However, the truncation of order of increments and special truncation for a given order is very important. In practical calculation usually the given order of increments is truncated including interactions up to certain nearest neighbor unit cells. The contributions from higher-order increments as well as from interactions between more distant cells are negligible.

Localized orbitals for finite-cluster calculation: Due to the fact that electron correlation effects are "local", the above localized-electron picture helps to handle the

problem of infinities at the correlated level. Localization of spin orbitals is readily accomplished by maximization of functional

$$L[\{\Phi_i\}] = \sum_i v_i^2 T_{iiii} \quad (5.51)$$

where v_i is the occupancy of the localized spin orbital Φ_i and $[T_{ijkl}]$ is the localization tensor. Various algorithms are available for the maximization of $L[\{\Phi_i\}]$. Following choices of $[T_{ijkl}]$ lead to different localization criteria:

(a) Edmiston-Ruedenberg localization [112, 113]:

$$T_{ijkl}^{ER} = \langle \Phi_i(1)\Phi_k(2) | r_{12}^{-1} | \Phi_j(1)\Phi_l(2) \rangle \quad (5.52)$$

(b) Foster-Boys localization [114, 115]:

$$T_{ijkl}^{FB} = -\langle \Phi_i | r | \Phi_j \rangle \cdot \langle \Phi_k | r | \Phi_l \rangle \quad (5.53)$$

(c) von Niessen localization [116]:

$$T_{ijkl}^N = \langle \Phi_i \Phi_k | \Phi_j \Phi_l \rangle \quad (5.54)$$

Edmiston-Ruedenberg localization method calls for repeated transformation of two-electron integrals and is computationally expensive. Therefore Foster-Boys and von Niessen approaches are more appropriate for large systems. All three criteria possess the propensity of mixing of σ and π spin orbitals in planar molecules. This hampers the clear interpretation of the resulting localized one-electron wavefunctions and calls for other localization criteria, e.g., Pipek and Mezey [117], etc.

5.2.2 Bloch-orbital-based approach

During the last couple of decades, the HF and DFT problems had been solved for the infinite periodic systems and the state of the art are present in the CRYSTAL program [118, 119]. In this section the formulation of the HF theory in CRYSTAL program is presented [120]. Consider $\Psi_i(\mathbf{r}, \mathbf{k})$ as a linear combination of Bloch functions (BF), $\phi_\mu(\mathbf{r})$ (here referred as atomic orbitals, AOs):

$$\Psi_i(\mathbf{r}; \mathbf{k}) = \sum_{\mu} a_{\mu,i}(\mathbf{k}) \phi_{\mu}(\mathbf{r}; \mathbf{k}), \quad (5.55)$$

where,

$$\phi_{\mu}(\mathbf{r}; \mathbf{k}) = \sum_{\mathbf{G}} \phi_{\mu}(\mathbf{r} - \mathbf{A}_{\mu} - \mathbf{G}) \exp(i\mathbf{k} \cdot \mathbf{G}). \quad (5.56)$$

Here, \mathbf{A}_{μ} denotes the coordinate of the nucleus in the reference cell on which ϕ_{μ} is centered, and the summation over \mathbf{G} is extended to all set of the direct lattice vectors, \mathbf{G} . The local functions are expressed as the linear combinations of a certain number,

n_g , of individually normalized Gaussian type functions (GTF) characterized by the same center, with fixed coefficients, d_j and exponents, α_j , defined as

$$\varphi_\mu(\mathbf{r} - \mathbf{A}_\mu - \mathbf{G}) = \sum_j^{n_g} d_j g(\alpha_j; \mathbf{r} - \mathbf{A}_\mu - \mathbf{G}) \quad (5.57)$$

The expansion coefficients of the Bloch functions, $a_{\mu,i}(\mathbf{k})$, are calculated by solving the Fock-matrix equation for each reciprocal lattice vector, \mathbf{k} :

$$F(\mathbf{k})C(\mathbf{k}) = S(\mathbf{k})C(\mathbf{k})E(\mathbf{k}) \quad (5.58)$$

in which $S(\mathbf{k})$ is the overlap matrix over the BF, $E(\mathbf{k})$ is the diagonal energy matrix and $F(\mathbf{k})$ is the Fock matrix in the reciprocal space given by

$$F(\mathbf{k}) = \sum_{\mathbf{G}} F^{\mathbf{G}} \exp(i\mathbf{k} \cdot \mathbf{G}) \quad (5.59)$$

The element of the Fock matrix, $F^{\mathbf{G}}$, can be written as a sum of one-electron and two-electron contributions in the basis of the AO:

$$F_{12}^{\mathbf{G}} = H_{12}^{\mathbf{G}} + B_{12}^{\mathbf{G}}. \quad (5.60)$$

The one-electron contribution is the sum of the kinetic and nuclear attraction terms and are given by

$$H_{12}^{\mathbf{G}} = T_{12}^{\mathbf{G}} + Z_{12}^{\mathbf{G}} = \langle \varphi_1^{\mathbf{O}} | T | \varphi_2^{\mathbf{G}} \rangle + \langle \varphi_1^{\mathbf{O}} | Z | \varphi_2^{\mathbf{G}} \rangle. \quad (5.61)$$

The two-electron term is the sum of the Coulomb and exchange contributions:

$$B_{12}^{\mathbf{G}} = J_{12}^{\mathbf{G}} + K_{12}^{\mathbf{G}} = \sum_{3,4} \sum_{\mathbf{n}} P_{3,4}^{\mathbf{n}} \sum_{\mathbf{h}} [(\varphi_1^{\mathbf{O}} \varphi_2^{\mathbf{G}} | \varphi_3^{\mathbf{h}} \varphi_4^{\mathbf{h}+\mathbf{n}}) - \frac{1}{2}(\varphi_1^{\mathbf{O}} \varphi_3^{\mathbf{h}} | \varphi_2^{\mathbf{G}} \varphi_4^{\mathbf{h}+\mathbf{n}})]. \quad (5.62)$$

The $P^{\mathbf{n}}$ density matrix elements in the AOs basis set are computed by integration over the volume of the Brillouin zone (BZ),

$$P_{3,4}^{\mathbf{n}} = 2 \int_{BZ} d\mathbf{k} \exp(i\mathbf{k} \cdot \mathbf{n}) \sum_j a_{3,j}^*(\mathbf{k}) a_{4,j}(\mathbf{k}) \theta(\varepsilon_F - \varepsilon_j(\mathbf{k})), \quad (5.63)$$

where $a_{i,n}$ denotes the i th component of the n th eigenvector, θ is the step function, ε_F , the Fermi energy and ε_n , n th eigenvalue.

5.2.3 Wannier-orbital-based approach

In Wannier-orbital-based method, instead of describing the electrons in terms of Bloch orbitals, one describes them in terms of mutually orthogonal orbitals localized within

the individual unit cells constituting the infinite solid. The Wannier-type orbitals are pseudo-canonical within the reference cell, i.e., they are not the most localized orbitals possible [121]. The following discussion outline the solution of the HF problem of an infinite periodic system in the Wannier representation.

A crystalline solid, in its ground state is composed of identical unit cells and the orbitals belonging to any other unit cell are identical to the corresponding orbitals belonging to any other unit cell and are related to one another by a simple translation operation. Consider the number of orbitals in a unit cell is n_c and if the α -th orbital of a unit cell located at the position given by the vector \mathbf{R}_j of the lattice is denoted by $|\alpha(\mathbf{R}_j)\rangle$ then the set $\{|\alpha(\mathbf{R}_j)\rangle; \alpha = 1, n_c; j = 1, N\}$ denotes all the orbitals in the unit cell. The translational symmetry condition expressed in the real space can be stated as

$$|\alpha(\mathbf{R}_i + \mathbf{R}_j)\rangle = T(\mathbf{R}_i)|\alpha(\mathbf{R}_j)\rangle, \quad (5.64)$$

where $T(\mathbf{R}_i)$ is an operator which represents a translation by a vector \mathbf{R}_i . One can write the total electronic energy of the solid as

$$E = N \left\{ 2 \sum_{\alpha=1}^{n_c} \langle \alpha(o) | T | \alpha(o) \rangle + \sum_{\alpha=1}^{n_c} \langle \alpha(o) | Z | \alpha(o) \rangle \right. \\ \left. + \sum_{\alpha, \beta=1}^{n_c} \sum_{j=1}^N (2 \langle \alpha(o) \beta(\mathbf{R}_j) | \alpha(o) \beta(\mathbf{R}_j) \rangle - \langle \alpha(o) \beta(\mathbf{R}_j) | \beta(\mathbf{R}_j) \alpha(o) \rangle) \right\}, \quad (5.65)$$

where $|\alpha(o)\rangle$ denotes an orbital centered in the reference unit cell. By assuming translation invariance in real space, the total HF energy of the infinite solid is expressed in terms of a finite number of orbitals. In order to make energy given in Eq. (5.65) stationary with respect to the first-order variations in the orbitals, subjected to the orthogonality constraint, HF operator is obtained and defined as

$$F = T + Z + 2 \sum_{\beta} J_{\beta} - \sum_{\beta} K_{\beta}. \quad (5.66)$$

The conventional Coulomb and exchange terms are defined as

$$J_{\beta} |\alpha\rangle = \sum_j \langle \beta(\mathbf{R}_j) | \frac{1}{r_{12}} | \beta(\mathbf{R}_j) \rangle |\alpha\rangle, \quad (5.67)$$

and

$$K_{\beta} |\alpha\rangle = \sum_j \langle \beta(\mathbf{R}_j) | \frac{1}{r_{12}} |\alpha\rangle | \beta(\mathbf{R}_j) \rangle, \quad (5.68)$$

respectively. In order to impose the requirement of obtaining localized Wannier orbitals, a projector operators corresponding to the orbitals centered in the unit cells in a sufficiently large neighborhood of the reference cell is introduced and given by

$$(T + Z + 2J - K + \sum_{k \in N} \sum_{\gamma} \lambda_{\gamma}^k |\gamma(\mathbf{R}_k)\rangle \langle \gamma(\mathbf{R}_k)|) |\alpha\rangle = \epsilon_{\alpha} |\alpha\rangle. \quad (5.69)$$

Here $|\alpha\rangle$ stands for $|\alpha(o)\rangle$, an orbital centered in the reference cell, N collectively denotes the unit cells in the neighborhood. The choice of N will dictate the system under consideration. The more delocalized electrons of the system are, the larger should be the N . The shift parameters λ_γ^k are the shift parameters associated with the corresponding orbital of N . For perfect orthogonality and localization, their values should be infinitely high. Here the projection operator along with the shift parameters simply plays a role of a localizing potential, since upon convergence their contribution to the HF equation vanishes. The orbitals contained in unit cell located farther than those in N should be automatically orthogonal to the reference cell orbitals. It is easy to see that the orthogonality of the neighboring orbitals to the reference cell orbitals along with translation symmetry of the infinite solid makes these orbitals as Wannier functions.

Part II

Applications

Chapter 6

Structural Properties

A variety of experimental techniques, particularly diffraction experiments can provide information concerning microscopic structure of amorphous solids. However, this information is limited almost entirely to the first two coordination shells, i.e., the bond lengths and angles of nearest-neighbor atoms comprising the basic structural unit. Even for monoatomic systems the RDF derived from scattering experiments have the difficulty, that peaks other than the first and second cannot be uniquely associated with a particular interatomic correlation. These are made up from a variety of contributions from higher-lying shells. This matter gets more complicated for multicomponent systems. One solution to these difficulties is the construction of models using theoretical methods like MD and MC.

In the following sections the discussion of structural properties of amorphous forms derived from ZSM-5 is presented, which were obtained using MD simulations.

6.1 Computational Details

The calculations were carried out with a modified and extended version [122] of the code of Oligschleger and Laird [123].

6.1.1 Interaction potential

The pairwise atomic interaction potential proposed by Kramer *et al.* [124] was used in all simulations. It was parameterized using data from *ab initio* calculations and experiment for achieving high accuracy and transferability. This potential has already been successfully applied for modelling of crystalline zeolite systems [125]. The functional form is a combination of Buckingham and Coulomb type and is given by

$$\phi(r_{\alpha\beta}) = \frac{q_{\alpha}q_{\beta}e^2}{r_{\alpha\beta}} + A_{\alpha\beta} \exp(-B_{\alpha\beta}r_{\alpha\beta}) - \frac{C_{\alpha\beta}}{r_{\alpha\beta}^6}. \quad (6.1)$$

Here $r_{\alpha\beta}$ is the distance between the two ions α and β ($\alpha, \beta \in \{\text{Si}, \text{O}\}$). The values of the partial charges q_α and q_β and the constants $A_{\alpha\beta}$, $B_{\alpha\beta}$ and $C_{\alpha\beta}$ are documented in Table. 6.1. The non-Coulombic contribution to the potential was truncated and shifted at a distance of 5.5 Å in order to remove fluctuations in the potential as described in chapter 2, section(2.4.1.1).

Table 6.1: Force-field parameters for BKS (Beest, Kramer and van Santen) potential.

$\alpha - \beta$	$A_{\alpha\beta}$ (eV)	$B_{\alpha\beta}$ (Å ⁻¹)	$C_{\alpha\beta}$ (eV Å ⁶)	q_α
<i>O - O</i>	444.7686	2.48513	0.0000	$q_O = -1.1$
<i>Si - O</i>	24441.2370	4.93504	180.8045	$q_{Si} = 2.2$

The above defined potentials have the unphysical property to diverge to minus infinity at very small distances [126, 127]. However this is not a severe drawback, since in order to get to such small distances the particles have to overcome a large barrier. In order to prevent the rare cases in which the particles cross the barrier and fuse together, we have substituted the potential given in Eq. (6.1) by a harmonic potential when $r_{\alpha\beta}$ is smaller than the location of the barrier, i.e., for $r_{\alpha\beta} \leq 1.1936$ Å for Si-O interaction. At low and intermediate temperatures this modification does not affect the results obtained with the potential given by Eq. (6.1) and in this limit we are thus working with the usual BKS potential. The cutoff radius for the total short-range and long-range part was taken to be 7.5 Å and 17.5 Å, respectively. The long-range Coulomb part was evaluated by means of the Ewald summation [61] with a constant α of 8.5 in Eq. (2.46) and by using all k -vectors with $|k| \leq 8 \cdot (2\pi/L)$ where L is the average length of the box.

6.1.2 Preparation of amorphous configurations

The simulations have been carried out on a (formally periodic) system with 3456 particles (Si,O) in the central MD box. The amorphous states of the silicious zeolite were generated by starting with an orthorhombic lattice of silicious ZSM-5 also widely known as silicalite, whose initial positional parameters were taken from Ref. [128].

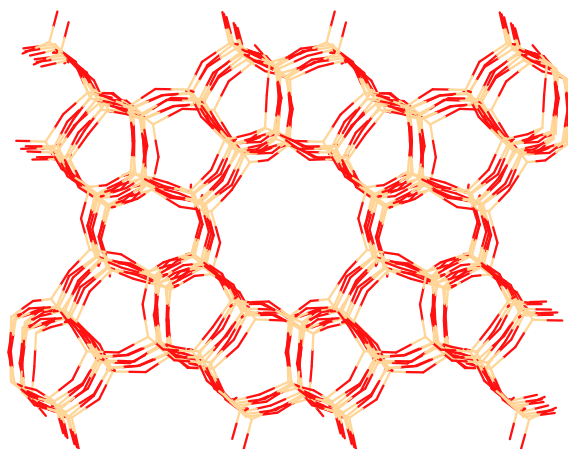


Figure 6.1: Zeolite ZSM-5 viewed along [010]. Yellow and red sticks represent Si and O atoms, respectively.

Zeolite ZSM-5 shown in Fig. 6.1 belongs to the MFI structure type. Examples of their uses include the conversion of methanol to gasoline, dewaxing of distillates, and the interconversion of aromatic compounds [129, 130]. It possesses orthorhombic symmetry $Pnma$ with cell parameters $a=20.07$, $b=19.92$, and $c=13.42$ Å and is characterized by a framework density of $18T/1000$ Å³. The three-dimensional channel system consists of straight channels running parallel to [010] having 10-membered rings of 5.4×5.6 Å free diameter and sinusoidal channels running parallel to [100] having 10-fold ring openings of 5.1×5.4 Å.

This initial configuration was heated to the temperatures $T = 4700$ K, 4800 K, 4900 K, 5000 K, with heating rate $D_{heat} < 4.7 \times 10^{13}$ K/s, was then equilibrated and finally quenched directly to $T = 300$ K with quenching rate $D_{quench} < 4.7 \times 10^{13}$ K/s, followed by equilibration and storage of atomic coordinates. Different maximum temperatures were applied in order to study the effect of the extent of amorphization on structural properties. Whereas properties such as coordination number, internal surface area or ring and pore size distribution are affected by the extent of amorphization, i.e., the maximum temperature, the positions of the peaks of the pair correlation functions and bond angle distributions are not. Vollmayr *et al.* demonstrated by simulations of amorphous silica that microscopic properties (radial distribution function, bond angle distribution and ring size distribution) are more affected by the choice of the quenching rate than macroscopic properties (density, enthalpy, thermal expansion coefficient) [127, 131]. Nevertheless, the simulated results using orders of magnitude higher quenching rates than feasible in the laboratory, e.g., the positions of the peaks of the pair correlation functions and bond angle distributions, are usually in good agreement with experimental data. The number density in the simulation cell was kept constant during all MD runs and corresponds to the mass density of 1.785 g/cm³. The equilibration was always done via constant-temperature MD simulations, by in-

tegrating the equation of motion with the velocity form of the Verlet algorithm using periodic boundary conditions. The equilibration time was about 0.6 ns corresponding to 3×10^5 integration steps. The time step was kept sufficiently small to guarantee a negligible drift of the total energy. We used the velocity rescaling method, where we averaged $T(t_i)$ over a period of 20 time steps [$T_{av} = \frac{1}{20} \sum_{i=m}^{m+19} T(t_i)$] and scaled the velocities after each period by $\sqrt{T_0/T_{av}}$ with T_0 being the "desired" temperature and T_{av} being the averaged temperature.

We monitor the atomic displacements during the course of MD runs by

$$\Delta R(t) = \sqrt{\sum_n [\mathbf{R}^n(t) - \mathbf{R}^n(0)]^2} \quad (6.2)$$

where $\mathbf{R}^n(t)$ is the position vector of particle n at time t and $\mathbf{R}^n(0)$ is the one at the starting or reference configuration. If the total displacement of the atoms exceeds a cutoff value, and the residence time of the atoms in the new positions also exceeds a minimal period of at least three times the period of a typical soft vibrational mode, the new positions of the particles were accepted as a starting point for the determination of a possible new minimum configuration. The cutoffs of displacements and resident time are chosen to avoid spurious minima. All stored coordinates were then quenched to $T = 0K$ using a combined steepest-descent-conjugate-gradient (SDCG) algorithm [132] to locate the nearest minimum configuration. These were further used for the analysis of the structural properties of the amorphous material.

6.2 Short-Range Order

To get insight into two-body structural correlation we have calculated total and partial pair-distribution functions from the MD trajectories. Partial pair-distribution functions $g_{\alpha\beta}$ are calculated from

$$\langle n_{\alpha\beta}(r) \rangle \Delta r = 4\pi r^2 \Delta r \rho_N c_\beta g_{\alpha\beta}(r) \quad (6.3)$$

where $n_{\alpha\beta}\Delta r$ is the number of particles of species β in a shell of thickness Δr , and radius r around a particle of species α and $\langle \dots \rangle$ represents the ensemble average and average over all particles of species α . ρ_N is the total number density (N/V , $N = N_\alpha + N_\beta$) and c_β is the concentration of species β . The contributions to the total pair-distribution function can be assigned by the peaks obtained in the partial pair-distribution functions. The computed total pair-distribution function and partial pair-distribution functions of Si-O, O-O and Si-Si are shown in Fig. 6.2. The most intense peak in the total pair-distribution function (Fig. 6.2(a)) arises from g_{Si-O} (Fig. 6.2(b)), smaller peaks at larger distances from g_{O-O} (Fig. 6.2(c)) and g_{Si-Si} (Fig. 6.2(d)). From the positions of these peaks we conclude that the Si-O bond length is $1.62 \pm 0.04 \text{ \AA}$ and the nearest neighbor O-O and Si-Si distances are $2.61 \pm 0.21 \text{ \AA}$ and $3.19 \pm 0.15 \text{ \AA}$, respectively.

The errors are obtained from the full width at half maximum (FWHM). The physical significance of the small peaks observed at smaller r than the most intense peaks appearing in Figs. 6.2(c) and 6.2(d) are discussed later.

The average coordination number (CN) of species α surrounded by species β , $Z_{\alpha\beta}$, is one of the most important pieces of information that can be obtained by performing integration around the first peak in the pair-distribution function.

$$Z_{\alpha\beta}(R) = 4\pi\rho_{\beta} \int_0^R g_{\alpha\beta}(r)r^2 dr, \quad (6.4)$$

Here R is the cutoff radius, usually chosen as the position of the minimum after the most intense peak of $g_{\alpha\beta}(r)$. For this integration the cutoff radii for Si-O, O-O and Si-Si are taken as 1.8 Å, 3.1 Å and 3.4 Å, respectively. From this analysis it is found that Si atoms are on the average coordinated by 3.99 O atoms and surrounded by 3.95 Si atoms. Similarly O atoms are coordinated by 2.00 Si atoms and surrounded by 6.02 O atoms. These findings indicate that the most common structural feature are all corner-sharing SiO₄ tetrahedra. The deviations from this pattern are discussed below.

The three-body correlations in amorphous ZSM-5 based material are examined and compared to the crystalline ZSM-5 through bond angle distributions plotted in Fig. 6.3, which give further information on local structural units. The O-Si-O angle distribution has the main peak at 108° with FWHM of 12.6°. The O-O-O angle distribution has an intense sharp peak at 59.4° with FWHM of 7.2° and the O-O-Si angle distribution has a main peak at 35.1° with FWHM of 6.2°. These peaks arise from atoms belonging to the same SiO₄ tetrahedra. For an ideal tetrahedron the O-Si-O, O-O-O and O-O-Si angles are 109.47°, 60° and 35.26°, respectively. The small deviations from the ideal values show that slightly distorted SiO₄ tetrahedra are the basic structural unit. Besides these peaks other intense peaks related to the connectivity between the SiO₄ tetrahedra are present. Similar to the pair-distribution functions in Fig. 6.2 smaller peaks at unexpected positions are observed in Fig. 6.3. All these features will be analyzed in the next section.

6.3 Connectivity of the Elementary Units

Considering the peaks of the pair-distribution and bond angle distribution functions we can interpret that the SiO₄ tetrahedra are linked in two ways as shown in Fig. 6.4. The model shown in Fig. 6.4(a), corresponds to the usual corner-sharing tetrahedra network. This structural pattern can be inferred from the peak of the Si-O-Si angle distribution at 157° with a broad FWHM of 40°, which represents the connectivity between two Si atoms present in neighboring tetrahedra with corner-sharing. The broad Si-O-Si angle distribution in the amorphous phase compared to the one obtained in the crystal indicates a considerable amount of flexibility in the Si-O-Si angle which is a major source of the disorder and allows for relaxation in a strained system. It has

even been shown by ball milling experiments of Kosanovic *et al.* [19] that breaking of these Si-O-Si bonds occurs in high silica zeolites and results in the collapse of the crystal structure leading to the formation of the amorphous phase. In the Si-Si-O angle distribution the peak around 21° comes from two silicon atoms bound to the same oxygen. The broad distribution from 80° to 180° in the O-O-O angle stems from O atoms bound to different Si atoms. The bond angle distribution for Si-Si-Si is peaked at 59° stemming mainly from Si atoms at their nearest neighbor distance of $\approx 3 \text{ \AA}$, and exhibits a broad maximum at 106° , hinting to a pattern in which Si is distorted tetrahedrally surrounded by four Si atoms at $\approx 5 \text{ \AA}$. The first peak points to the existence of 3-fold rings in this ZSM-5 based amorphous form, whereas the broad maximum results from the usual coordination between SiO_4 tetrahedra also present in the crystal.

The positions of the first and less intense peaks in g_{0-0} and $g_{\text{Si-Si}}$ occurring around 2.2 \AA and 2.5 \AA , respectively, look surprising at first glance. But selectively collecting the coordinates of such configurations provides strong evidence for the presence of edge-sharing SiO_4 tetrahedra. These are present in small percentage of around 1%-4% (depending on the extent of amorphization) in the ensemble of collected configurations. This model of edge-sharing between tetrahedra as shown in Fig. 6.4(b), is also in agreement with small peaks appearing in the bond angle distributions of O-Si-O at 83° , Si-O-Si at 95° , O-O-Si at 48° and Si-Si-O at 42° . These are related to four atoms, i.e., the Si centers of two edge-shared tetrahedra as well as the bridging O atoms. The peak at 83° in the O-Si-O bond angle distribution shows that the edge-shared tetrahedra are distorted severely. Edge sharing tetrahedra are also found in nature in the SiO_2 allotrope W-silica [133] and the silicate mineral leucophoenicite $\text{Mn}_7(\text{SiO}_4)_3(\text{OH})_2$ [134]. We note that in Car-Parrinello molecular dynamics studies of dehydroxylated silica surface also edge-shared tetrahedra are observed [135]. However, the edge-shared tetrahedral structures in nature are quite rare, which is usually explained by Pauling's third rule in terms of Coulombic repulsion between the cations sharing polyhedral units. Pauling's third rule states that the presence of shared edges and especially of shared faces in a coordinated structure decreases its stability. Violation of the rule is strong evidence that the structure is covalent.

In the past molecular orbital studies at the SCF- $X\alpha$ and CNDO/2 level on the rhombohedral molecule Si_2O_2 and two silicate tetrahedra sharing a common edge and saturated with hydrogens at the periphery, i.e., $\text{Si}_2\text{O}_6\text{H}_4$, have shown that covalent forces play an important role in causing edge-sharing type distortions [136, 137]. In order to analyze the validity of the results for such structural units obtained via MD, we carried out geometry optimizations using gradient-corrected DFT, HF and MP2 calculations on the edge-shared model system $\text{Si}_2\text{O}_6\text{H}_4$. The DFT and MP2 calculations were performed using the TURBOMOLE [138] and MOLPRO [139, 140] program packages, respectively. Geometric parameters for the bridged unit for edge-shared tetrahedra are presented in Table 6.2. It is obvious that the result of MD for the amorphous form derived from ZSM-5 is consistent with the experimental data for W-silica and the quantum chemical values for the edge-sharing model system. Note that the DFT and MP2 calculations on the model system do not include the effect of the surroundings.

We have also carried out solid-state *ab initio* calculations of the edge-sharing system, which include the effect of a condensed environment. The details of these calculations are presented in Chapter 8.

Frequency calculations at the HF-level on the edge-shared model system give all positive frequencies indicating that the structure corresponds to a local minimum. In the polarized Raman spectra of vitreous SiO₂, the D_1 defect line at 495 cm⁻¹ was left unassigned [141, 157]. We suggest that this could be due to the out-of-plane bending motion of the bridged unit, which was obtained in our frequency calculation on the edge-shared model system at 510 cm⁻¹. It is fair to note, however, that other interpretations also exist, i.e., no edge-sharing tetrahedra were observed in Car-Parrinello dynamics of vitreous silica and the D_1 defect line was associated with a breathing motion of 3-fold rings [142].

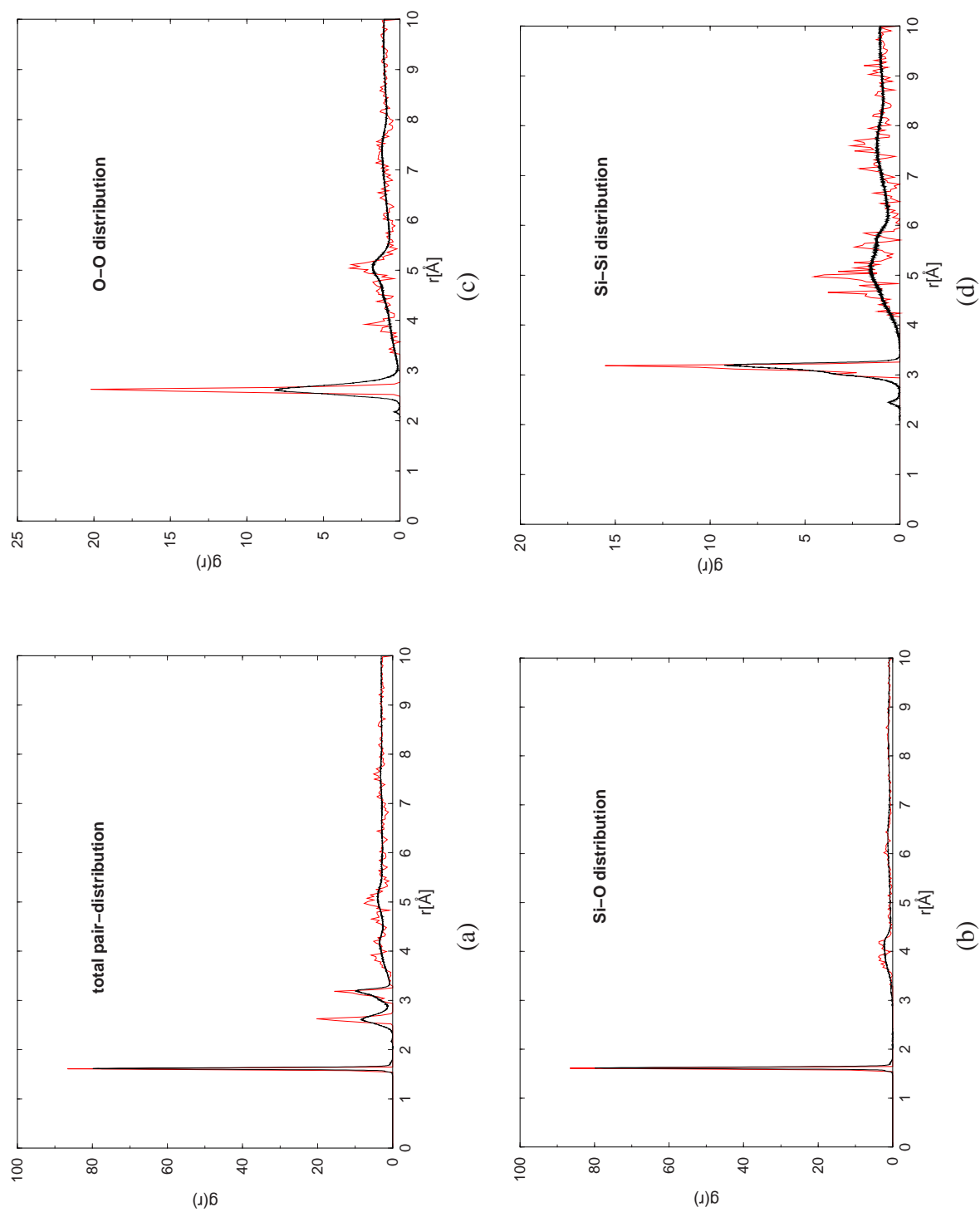


Figure 6.2: Total pair-distribution function (a) and the partial pair-distribution functions (b)-(d) in amorphous zeolite (black line) at $T = 300$ K derived from the crystalline structure (red line) when heated to 5000 K.

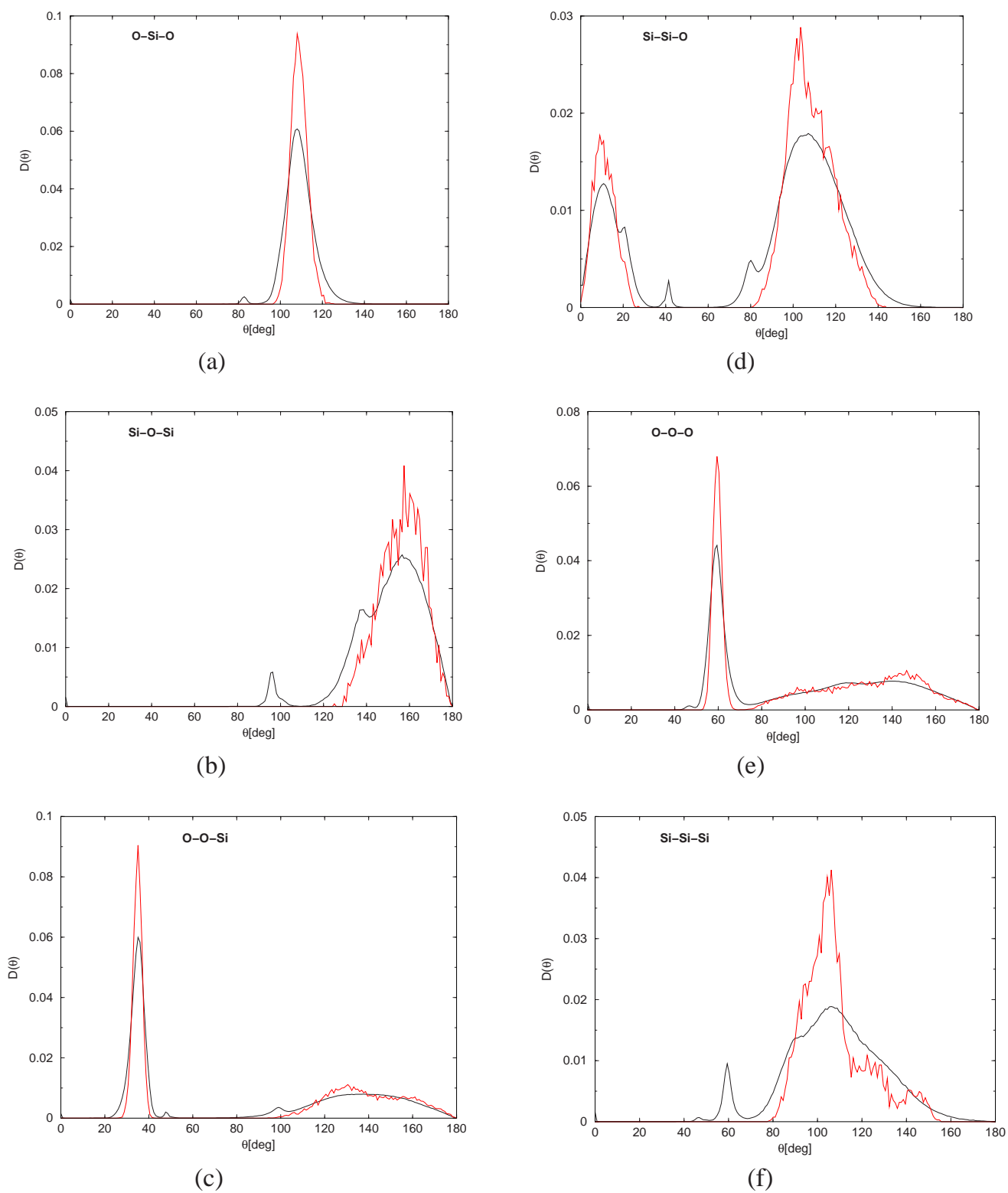


Figure 6.3: Bond angle distribution in crystalline ZSM-5 (red line) and amorphous zeolite derived from ZSM-5 (black line) at $T=300$ K.

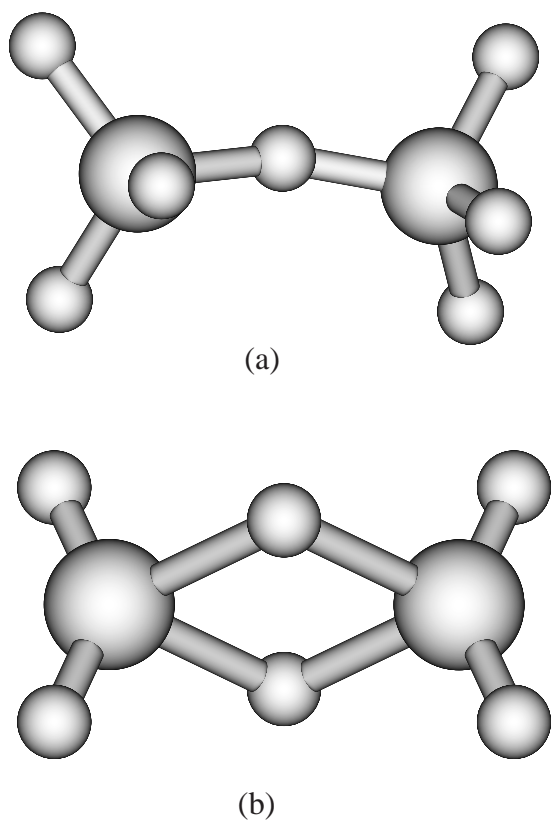


Figure 6.4: Model for the connectivity of tetrahedra in amorphous zeolite derived from ZSM-5. (a) Corner-sharing tetrahedra, (b) edge-sharing tetrahedra. (Big spheres represent Si atoms and small spheres represent O atoms.)

Table 6.2: Bond distances R (in Å) and bond angles ϕ (in degrees) for the bridged unit in edge-shared SiO_4 tetrahedra. For the sake of comparison the experimental result on W-silica from Ref. [133] is provided.

	Expt.	MD	DFT				MP2
			BP86 ^a		B3LYP ^b		
			TZVP ^c	TZVPP ^d	TZVP ^c	TZVPP ^d	
$R_{\text{Si-Si}}$	2.58	2.45 ± 0.1	2.37	2.39	2.37	2.38	
$R_{\text{O-O}}$	-	2.16 ± 0.05	2.40	2.38	2.37	2.37	
$R_{\text{Si-O}}$	1.87 ± 0.09	1.7 ± 0.16	1.69	1.69	1.68	1.68	
$\phi_{\text{O-Si-O}}$	-	83°	90.7°	89.6°	90.0°	89.6°	
$\phi_{\text{Si-O-Si}}$	-	95°	89.3°	90.4°	90.0°	90.4°	

^a Becke's gradient-corrected exchange functional [144] in combination with Perdew's correlation functional [145].

^b Becke's hybrid three-parameter exchange functional [143].

^c Valence triple- ζ basis set with one polarization function.

^d Valence triple- ζ basis set with two polarization functions.

^e Augmented correlation-consistent polarized valence triple-zeta basis set of Dunning [146, 147].

6.4 Extent of Amorphization

It was shown recently that there is a direct connection between the percentage of crystallinity of partially crystalline zeolitic material and its catalytic properties and ion exchange capacity [24, 28, 148]. If such chemical properties are based mainly on electronic effects, accurate quantum chemical calculations are needed for their investigation and explanation. However, in zeolitic systems steric effects play a great role to direct selectivities of reactions. These can be investigated by analysis of structures obtained by MD. Hence we choose a semiquantitative description to analyze the extent of amorphization, which is similar to the percentage of XRD crystallinity advocated by Nicolaidis as in Eq. (1.1) [28]. In order to get a measure independent from the number of atoms in the central MD box we choose the energy per atom as a criterion to describe the extent of amorphization of the system. We define the "percentage of energy crystallinity" (PEC), i.e.,

$$PEC = \frac{E_{amorphous} - E_{configuration}}{E_{amorphous} - E_{crystalline}} \times 100 \quad (6.5)$$

as a normalized dimensionless measure of the extent of amorphization. Here $E_{amorphous}$ corresponds to the energy per atom of the maximum amorphized structure we have obtained after minimization in our simulation, i.e., -16.90 eV/atom (in the part of configurational space spanned in our simulation no higher lying minimum occurs), and $E_{crystalline}$ corresponds to the energy per atom of the crystalline ZSM-5 system, i.e., -17.17 eV/atom. $E_{configuration}$ stands for the energy of the structure whose PEC we are interested in. It should be mentioned that clearly our definition of PEC depends on the maximum extent of amorphization obtained in the simulations, i.e., on the maximum temperature (here 5000 K) as well as the quenching rate (here 4.7×10^{12} K/s).

As shown in Fig. 6.5, the comparison between the cross section of crystalline ZSM-5 and the simulated ZSM-5 based amorphous structure with different extent of amorphization, the amorphization leads to local disorder and partial collapse of the framework structure. It is mainly this modification of pores and cavities which may allow a tuning of properties of significant interest.

6.4.1 Defect in coordination number

In Fig. 6.6 the distribution of coordination numbers (Z) for O atoms (Z_O) and Si atoms (Z_{Si}) for different PEC is given. If the interatomic distance $r < 1.8 \text{ \AA}$ (i.e., the distances corresponding to the first peak in the pair-distribution function Fig. 6.2 (a)) then the atoms are considered to be neighbors. One can easily observe the fraction of coordination defects, i.e., atoms with coordination numbers other than the ideal ones ($Z_O=2$ and $Z_{Si}=4$) decrease with PEC. Even in highly amorphized structures (low PEC) 95% of O atoms and 90% of Si atoms remain 2- and 4-coordinated, respectively.

Only 3% of the O atoms are under-coordinated ($Z_O=1$) and 2% over-coordinated ($Z_O=3$). In the case of the Si atoms around 9% are under-coordinated ($Z_{Si}=3$) and

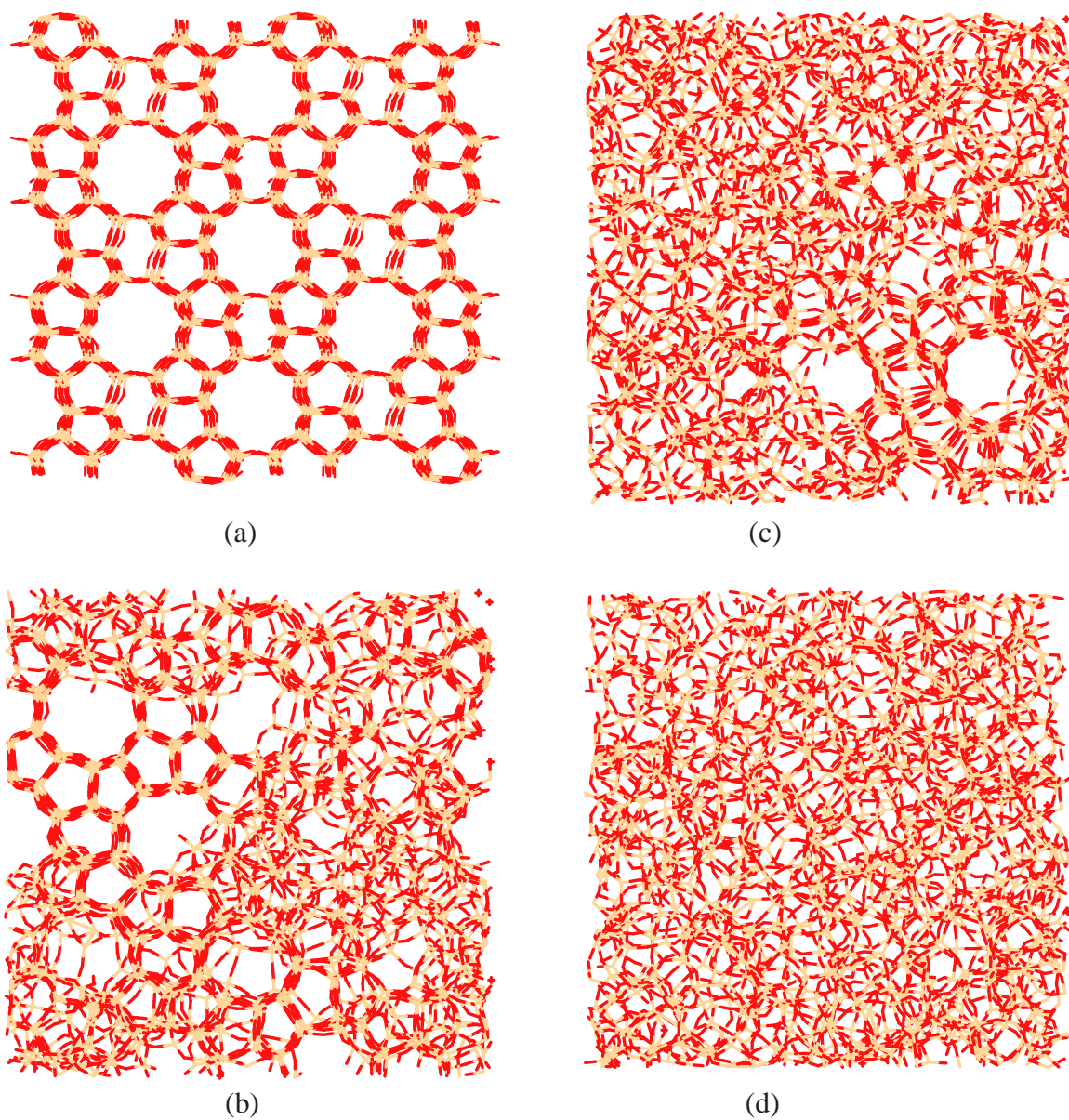
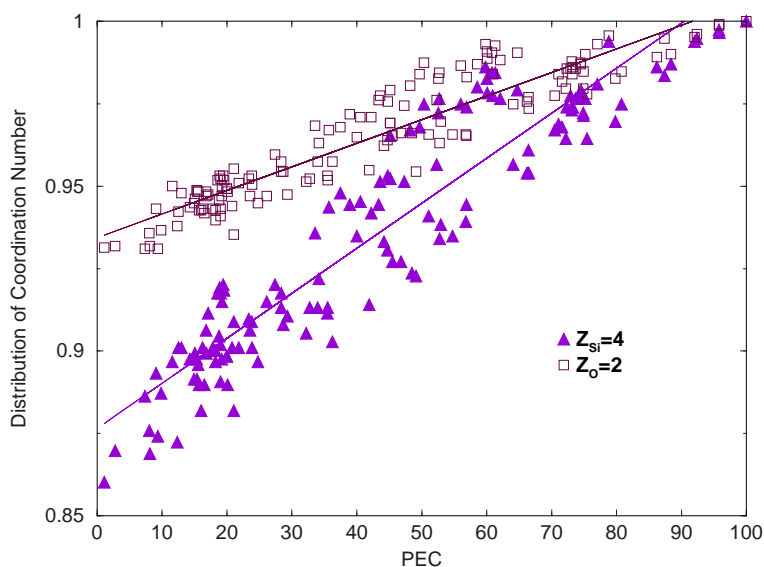
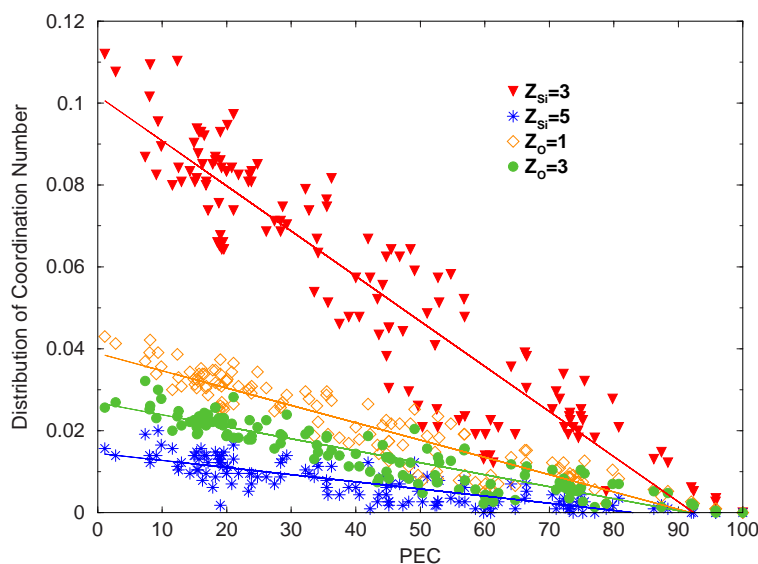


Figure 6.5: Cross section of (a) ZSM-5(crystalline), and simulated amorphous form derived from ZSM-5 with (b)80%, (c)60% and (d)20% crystallinity. Red and yellow sticks represent O and Si atoms. In all figures 3456 atoms are displayed and the view is along the Y-axis.



(a)



(b)

Figure 6.6: (a) Distribution of coordination numbers in which an O atom is surrounded by 2 atoms ($Z_O=2$) and a Si atom is surrounded by 4 atoms ($Z_{Si}=4$) vs. percentage of energy crystallinity (PEC). (b) Distribution of coordination number in which an O atom is surrounded by 1 ($Z_O=1$) and 3 ($Z_O=3$) and a Si atom is surrounded by 3 ($Z_{Si}=3$) and 5 ($Z_{Si}=5$) atoms. The solid lines were obtained from linear regression and should serve as guides for the eye, for each distribution. Note the difference in scale of the y-axis in (a) and (b). The data displayed results from a total of 140 configurations.

1% over-coordinated ($Z_{Si}=5$). The analysis by linear regression suggests that in this amorphous material low coordinations are more favored than high coordinations, (cf. Fig. 6.6). We note that also in other related amorphous systems, e.g., SiO₂ glass at low temperature [149], under-coordination of Si and O is preferred, whereas with increasing temperature over-coordination of both Si and O becomes more frequent [149, 150]. However, in the molecular dynamics simulation of silica glasses it was shown by Feuston *et al.* that the coordination number distribution strongly depends on the interaction potential used and that the structures obtained by introduction of three body potentials have fewer defects compared to those derived from calculations using only pair potentials [151].

6.4.2 Internal surface area

Table 6.3: Atomic/ionic radii R_{coord} (in Å) for O and Si depending on the coordination number (CN).

CN	$R_{coord}(O)$	$R_{coord}(Si)$
0	1.52 ^a	2.10 ^b
1	1.435	1.64
2	1.35 ^c	1.18
3	0	0.72
4	0	0.26 ^d
5 and higher	0	0

^a Van der Waals radius of O atom.

^b Van der Waals radius of Si atom.

^c Ionic radius of O^{2-} , having CN 2.

^d Ionic radius of Si^{4+} having CN 4.

Among the most characteristic structural features of zeolites are their large internal surface area (ISA) and high porosity, which both are important factors for catalytic properties (apart from the presence of acidic sites in heteroatom-substituted zeolites). Therefore it is of interest to study the dependence of both ISA and porosity on the degree of amorphization, e.g., the PEC.

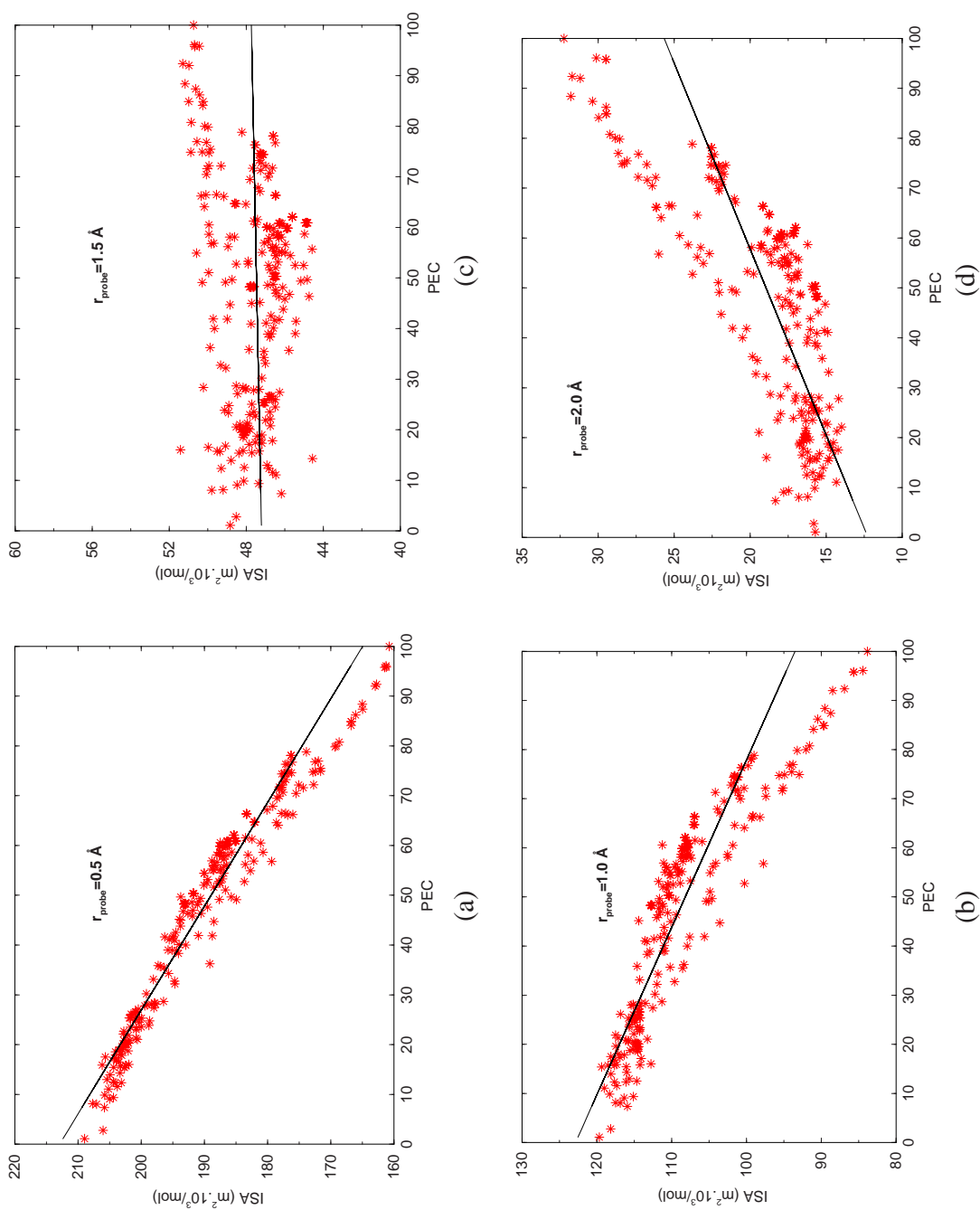


Figure 6.7: Internal surface area (ISA) vs. percentage of energy crystallinity (PEC) for 310 configurations in dependence of the probe-atom radius. The straight lines are taken from a linear regression (slopes = -0.479, -0.293, 0.005, 0.134, intercept = 212.94, 122.87, 47.20, 12.26 in units of the plot for $r_{\text{probe}} = 0.5 \text{ \AA}$, 1.0 \AA , 1.5 \AA , 2.0 \AA).

In order to calculate ISA we model the system as an ensemble of intersecting hard spheres with radii depending on the CN of the constituting atoms/ions. The CN of Si/O was determined as the number of O/Si centers within a distance of 1.8 Å, i.e., all bonds contributing to the first peak in the pair-distribution function g_{Si-O} (Fig. 1(b)) were included. Since the higher the CN of an atom/ion in the framework, the lower its contribution to ISA, we chose the radii according to Table 6.3: for uncoordinated atoms the van der Waals radii were chosen [152], whereas for standard CN 4 for Si and 2 for O the ionic radii of Si^{4+} and O^{2-} were selected [153]. For intermediate values of the CN a linear interpolation was used. Contribution of atoms/ions with higher than the standard CN were neglected.

The effective ISA of a system under study depends also on the size of the probe used to measure it. A standard way to derive the effective ISA is the so-called probe-atom model, where the ISA is defined by a surface generated by the center of a hard test sphere of radius r_{probe} rolling over the ensemble of intersecting spheres [152]. Recently Moloy *et al.* demonstrated for various crystalline zeolites that the ISA decreases by a factor of 1.4 to 2.8 when the radius of the probe atom is increased from 0.5 Å to 1.1 Å [154]. We therefore applied four different radii of the probe atom, i.e., 0.5, 1.0, 1.5 and 2.0 Å, in order to investigate the probe size dependency of the ISA upon amorphization. For the practical calculation of the ISA we increment the radii of the intersecting spheres described above by the probe-atom radius. The surface of the resulting ensemble of sphere was estimated as

$$ISA = \frac{1}{M} \left(\sum_{i=1}^N 4\pi [R_{coord}(i) + r_{probe}]^2 \frac{p_i}{p} \right) \quad (6.6)$$

Here the sum runs over all N centers i in the MD box, $R_{coord}(i)$ refers to the atom/ion radius from Table 6.3, r_{probe} is the probe-atom radius and M refers to the amount of SiO_2 present in the structure considered. A total of p points (here $p=614$) is distributed equally on the surface of each sphere i , and the number p_i of points not located inside other spheres is determined. The ratio p_i/p then provides the fraction of the accessible surface contributed by center i . Note that our definition of ISA does not consider cases where there may be internal surfaces which are not accessible due to absence of windows by which probe molecules can enter. Therefore, the values obtained here represent upper bounds to the actual accessible internal surface area.

Fig. 6.7 (a)-(d) contains our result for the ISA of 310 configurations determined with four different probe radii. Our values for crystalline ZSM-5, i.e., 160.77 and 83.86 $m^2 \cdot 10^3/mol$ for probe-atom radii of 0.5 and 1.0 Å, respectively, are in excellent agreement with results published by Moloy *et al.*, i.e., ≈ 162 and $\approx 84 m^2 \cdot 10^3/mol$ (taken from their Fig. 7, entry MFI) [154]. Amorphization leads to a collapse of the zeolitic framework and reduces the number of big pores (cf. also the discussion of ring statistics given below). This is evident from Fig. 6.7 for $r_{probe}=2.0$ Å, where amorphization decreases the ISA by roughly a factor of 2. However, for a small probe radius as $r_{probe}=0.5$ Å one observes an increase of the ISA by about a factor of 2. This

is explained partly by the increasing percentage of under-coordinated centers in the amorphous system (cf. Fig. 6.6), but also by the increasing tendency to convert larger rings into smaller rings (cf. below). In conclusion amorphization makes the framework less accessible for larger species and more accessible for smaller ones. Such structural changes can be of high importance for catalysis, where the accessibility of the acidic sites (in case of protonated ZSM-5) and the rate of adduct-product exchange at the active site can be the crucial parameters to influence the yield and selectivity of certain reactions [148, 155]. Changes in the network topology may also result in the closure of sites suitable for ion exchange (in case of hetero-atom substituted zeolites).

6.4.3 Ring analysis

In order to gain further insight in the connectivity between the SiO_4 tetrahedra and to measure quantitatively the effects of amorphization on the structure, e.g., the porosity, we performed a ring analysis. In the following we define a n -fold ring by the number n of Si atoms connected by bridging O to give a ring. The number of Si atoms was determined by first assigning to each bridging O atom a pair of adjacent Si atoms and then tracing possible connections to a ring containing a maximum of up to 15 Si atoms. Double counting is avoided and sets of Si atoms defining a small ring are not allowed to contribute as a whole to a large ring. Since rings can extend to periodic images of the MD boxes the periodic boundary condition was removed for determining the ring distribution. The latter is sensitive to the temperature and the threshold for the maximum distance between bonded atoms, thus configurations with similar PEC can exhibit slight differences in their ring distributions. The statistics for n -fold rings presented in Fig. 6.8 and Table 6.4 nevertheless clearly shows characteristic features depending on the PEC.

Crystalline ZSM-5 contains mainly 5-fold (48.9%) and 6-fold (39.2%) rings, along with a smaller amount of 10-fold (9.0%) and 4-fold (2.9%) rings. Amorphization is found to lead to a broad distribution of ring sizes from 2 to 10. In 15% energy crystalline amorphous material we observe still 5-fold (29.3%) and 6-fold (26.8%) rings to be most frequent, however also 4-fold (17.3%) and 3-fold (13.0%) rings contribute significantly. We can compare these findings to those from previous related work on SiO_2 glass, which exhibits a pronounced dominance of 6-fold rings, i.e., 3- to 6-fold rings contribute with 3.0, 11.1, 24.2 and 61.6 %, respectively [156]. Whereas for our system at small PEC (as well as for the crystal) larger than 6-fold rings are present to less than 10%, they contribute with up to 20% for intermediate values of PEC. In these cases 7-fold rings contribute roughly as much as 4-fold ones. Therefore, besides the collapse of the 10-fold rings in crystalline ZSM-5 upon amorphization, also a "fusion" of smaller membered rings to more than 6-fold rings must occur.

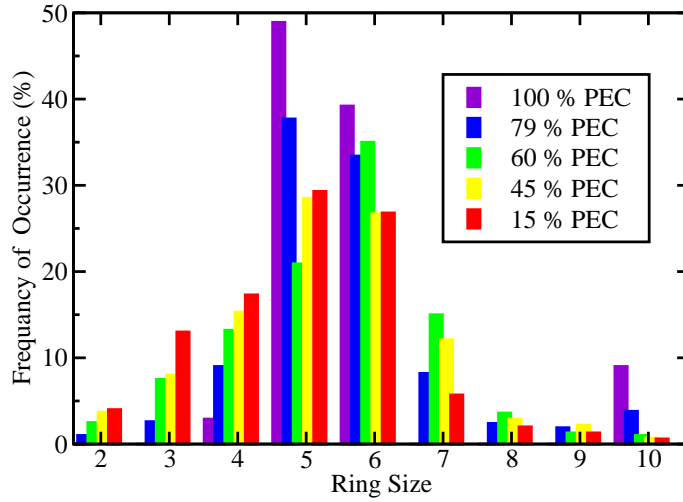


Figure 6.8: Frequency of occurrence of n -fold rings in (partially) amorphous material derived from ZSM-5.

The bond angle distributions suggest that both 2-fold and 3-fold rings are essentially planar. For 2-fold rings Si-O-Si and O-Si-O angle distributions have a peak near 90° and for 3-fold rings Si-Si-Si and O-O-O angle distributions have a peak near 60° . This result agrees quite well with the finding of Galeener based on force-field calculations that 2-fold and 3-fold rings of Si-O bonds in the vitreous form of SiO_2 are expected to be planar [157]. The presence of 2-fold rings again indicates the existence of edge-sharing tetrahedra. However, the modest number of 2-fold rings suggests that most tetrahedra are linked to each other by corners.

Much more difficult than the purely topological analysis of ring sizes is their geometrical measurement. Whereas small rings are essentially planar, larger ones are usually puckered considerably and make the definition of a ring diameter meaningless. Therefore, we calculate two simple measures for each ring, i.e.,

$$r_{avg} = \frac{1}{n} \sum_{\substack{i=1 \\ i \in ring}}^n |\mathbf{R}_{Si}(i) - \mathbf{R}_c| \quad (6.7)$$

and

$$r_{min} = \min_{i \in ring} |\mathbf{R}_{Si}(i) - \mathbf{R}_c| \quad (6.8)$$

Table 6.4: Ring analysis for ZSM-5 based amorphous material depending on the extent of amorphization at 300 K measured as percentage of energy crystallinity (PEC). The first line for each PEC gives the occurrence of n-fold rings in percent (%). In the second and third line the average and minimal radii \bar{r}_{avg} and \bar{r}_{min} are listed (in Å). The rightmost column contains estimate of the pore size S_{avg} and S_{min} .

PEC	n = 2	3	4	5	6	7	8	9	10	pore size
100	-	-	2.9	48.9	39.2	-	-	-	9.0	
			2.19	2.57	2.85				4.70	2.86
			2.16	2.42	2.53				4.32	2.62
79	1.0	2.6	9.0	37.7	33.4	8.2	2.4	1.9	3.8	
	1.22	1.72	2.17	2.58	2.89	3.28	3.65	4.16	4.68	2.81
	1.22	1.66	2.04	2.37	2.50	2.70	2.97	3.49	4.17	2.48
60	2.5	7.5	13.2	20.9	35.0	15.0	3.6	1.3	1.0	
	1.23	1.71	2.16	2.54	2.68	3.29	3.70	4.06	4.49	2.64
	1.23	1.66	2.01	2.26	1.87	2.70	3.00	3.04	3.54	2.13
45	3.7	8.0	15.3	28.5	26.7	12.1	2.9	2.2	0.7	
	1.23	1.88	2.50	3.07	2.78	3.29	3.63	4.01	4.26	2.82
	1.23	1.64	2.00	2.19	1.94	2.67	2.84	3.08	2.99	2.12
15	4.0	13.0	17.3	29.3	26.8	5.7	2.0	1.3	0.6	
	1.25	1.90	2.54	3.00	2.57	3.22	3.42	3.80	4.12	2.63
	1.25	1.57	1.81	1.81	1.37	2.52	2.58	2.29	2.44	1.71

The center of a n-fold ring \mathbf{R}_c herein is defined as

$$\mathbf{R}_c = \frac{1}{n} \sum_{\substack{i=1 \\ i \in \text{ring}}}^n \mathbf{R}_{Si}(i) \quad (6.9)$$

The quantity r_{min} gives a maximum radius below which atoms/molecules will be able to pass through the ring. For planar and regular rings r_{min} will be close to the average r_{avg} , for puckered and irregular rings r_{avg} will be significantly larger than r_{min} . Measures \bar{r}_{avg} and \bar{r}_{min} for the effective size of a certain type of rings are then generated by averaging r_{avg} and r_{min} over all rings of the specific type in the systems. Clearly, these quantities derived solely from the positions of the Si atoms are to a certain extent

arbitrary. In reality the effective ring size depends not only on the electron density distribution of the Si and O atoms in the ring but also on the one of the probe system. In addition vibrational motion will affect the effective ring size. Summing up, a well defined unique probe-independent measure of ring size cannot be given, nevertheless we believe that the values of \bar{r}_{avg} and \bar{r}_{min} listed also in Table 6.4 provide reasonable trends.

For crystalline ZSM-5 the values of \bar{r}_{avg} and \bar{r}_{min} are quite similar with a maximum deviation of $\approx 13\%$ for 6-fold rings. With increasing degree of amorphization the ratio $\bar{r}_{avg}/\bar{r}_{min}$ increases up to almost a factor of two for some ring sizes, i.e., ≈ 1.9 for 6-fold and ≈ 1.7 for 5-, 9- and 10-fold rings. This indicates that the most frequently occurring ring types (5- and 6-fold) have the largest tendency to irregular shape and puckering, leading to smaller effective pore sizes in amorphous systems.

From the individual ring averages \bar{r}_{avg} and \bar{r}_{min} we can derive global averages S_{avg} and S_{min} for the amorphous system (cf. the right column in Table 6.4) by weighting the ring-specific values \bar{r}_{avg} and \bar{r}_{min} with the occurrence of the ring types. These should have some relation to measured effective pore sizes. Whereas the averaged value S_{avg} does not exhibit a clear trend with decreasing PEC, the average S_{min} clearly decreases. This finding is in line with the concomitant decrease of ISA for large probe-atoms depicted in Fig. 6.7. We conclude that S_{min} might be more helpful in the discussion of catalytic processes. Finally we want to mention that despite all reservation the order of magnitude of S_{min} appears to be realistic: for crystalline ZSM-5 we estimate an effective pore diameter of at least 5.2 Å. This agrees well with the value of around 5.5 Å of the micropore size distribution by Saito *et al.* obtained experimentally from high resolution argon adsorption on ZSM-5 [158].

This part of the work is published in Ref. [159]

Chapter 7

Vibrational Properties

Experimental studies on the mechanical treatment of zeolites by ball-milling processes show that the amorphization also causes remarkable changes in the vibrational infrared (IR) spectra which were associated with the breaking of Si-O-Si bonds [19,20]. It was suggested that certain characteristic bands could be used as probes for detecting the extent of the presence of the zeolite framework [160]. In the following section, a detailed investigation of vibrational properties of amorphous materials derived from the silicious ZSM-5 is presented.

7.1 Vibrational Density of States

The absence of a periodic lattice in amorphous materials has several effects; an immediate consequence is that there is no reciprocal lattice and so \mathbf{k} is no longer a good quantum number for excitations in the solid, such as phonons (as described in chapter 4 section (4.2.3)). Thus phonon states cannot be described in terms of dispersion curves, instead the only quantity which is a valid description of excitations in a non-crystalline solid is the "density of states" (DOS).

The dependence of many thermodynamic properties, e.g., the specific heat C_V , on vibrational motions, makes the vibrational DOS a crucial property of solids. Experimentally it can be measured with inelastic neutron scattering as well as IR and Raman spectroscopy. In the following we present calculations of the vibrational DOS obtained by two theoretical methods, i.e., the diagonalization of the dynamic matrix and the Fourier transformation of the velocity-autocorrelation function [161, 162]. Numerical calculations of the vibrational DOS by the diagonalization of the dynamic matrix are based on the harmonic approximation of the potential energy, allow an analysis of the vibrational modes, but neglect anharmonicities as well as temperature effects. Using the second method proposed above, one is able to study the temperature dependence of the vibrational and thermodynamic properties of the solids. However, this method

suffers from the finite resolution of frequencies and the lack of information about the eigenmodes of the structures.

A detailed description of the structure generation is given in Chapter 6. In all 20 structures each comprising of 1152 particles were generated. After quenching the low-temperature configurations, i.e., the ones obtained at 300 K, a final quenching to 0 K leading to the local minima of the potential energy surface was performed. In these minima we calculated the dynamic matrix whose elements are the mass-weighted second derivatives of the potential energy U with respect to the atomic positions

$$D_{\alpha\beta}^{mn} = \frac{1}{\sqrt{M_n M_m}} \frac{\partial^2 U(\mathbf{R}^m - \mathbf{R}^n)}{\partial R_\alpha^m \partial R_\beta^n},$$

$$m, n = [1, 2, \dots, N], \alpha, \beta = [x, y, z]. \quad (7.1)$$

Here M_n represents the mass of the n th atom and R_α^n is the coordinate of atom n in α direction. Diagonalization of the dynamic matrix gives $3N$ eigenvalues corresponding to the square of the eigenfrequencies (ω^2 , where $\omega = 2\pi\nu$) and real eigenvectors (\mathbf{e}). Among the $3N$ vibrational modes the contributions by the three translation modes are almost negligible. The vibrational DOS is obtained from the frequencies ν^j of $3N-3$ vibrational and rotational modes j as

$$Z(\nu) = \left\langle \frac{1}{3N-3} \sum_j \delta(\nu - \nu^j) \right\rangle, \quad (7.2)$$

where δ is the discretized delta function and $\langle \dots \rangle$ stands for an ensemble average. Due to the small system size the low-frequency part (below 0.7 THz) could not be obtained and hence we calculated the Debye spectrum given by

$$Z_{Debye} = \frac{3}{\nu_D^3} \nu^2, \quad (7.3)$$

with

$$\nu_D = \bar{c} \left(\frac{3N}{4\pi V} \right)^{1/3}. \quad (7.4)$$

Here \bar{c} represents the average sound velocity given in terms of the longitudinal and transverse velocities c_l and c_t , respectively. N/V is the number density of the system. We use the fact of the isotropy of amorphous materials and calculated these velocities from the elastic constants as $c_l = \sqrt{c_{11}/\rho}$ and $c_t = \sqrt{c_{44}/\rho}$, where ρ is the mass density of the system. These values of the elastic constants were obtained from the changes in the potential energy ΔE under an applied strain

$$R_\alpha^m \rightarrow R_\alpha^m + \sum_\beta \epsilon_{\alpha\beta} R_\beta^m, \quad (7.5)$$

$$\Delta E = - \sum_{\alpha\beta} P_{\alpha\beta} \epsilon_{\alpha\beta} + \frac{V}{2} \sum_{\alpha\beta\gamma\delta} \epsilon_{\alpha\beta} C_{\alpha\beta\gamma\delta} \epsilon_{\gamma\delta} + \frac{1}{2} \sum_{\alpha\beta\gamma} P_{\alpha\beta} \epsilon_{\alpha\gamma} \epsilon_{\gamma\beta}. \quad (7.6)$$

Here ε is a transformation matrix which determines the shape of the system cell, i.e., the relative expansion and compression of a structure. The first term in Eq. (7.6) accounts for the work done against the forces for an ensemble which is not in equilibrium against the volume changes, where $P_{\alpha\beta}$ is the virial of the forces. The second term comes from the usual definition of the elastic energy density. The third term is the correction for a volume change under a finite shear. $C_{\alpha\beta\gamma\delta}$ are the elastic constants ($c_{11} = C_{1111}$, $c_{44} = C_{2323}$ according to Voigt's contraction scheme [163]).

As mentioned above the vibrational spectra can also be calculated by the velocity autocorrelation function defined as

$$g(t) = \sum_{m=1}^N \frac{\langle \mathbf{v}^m(t) \cdot \mathbf{v}^m(0) \rangle}{\langle \mathbf{v}^m(0) \cdot \mathbf{v}^m(0) \rangle}. \quad (7.7)$$

Here \mathbf{v}^m represents the velocity of the m th atom. The Fourier cosine transformation of the velocity autocorrelation function gives the vibrational DOS

$$Z(\nu) = \left\langle \frac{2}{\pi} \int_0^{t_{obs}} g(t) \cos(2\pi\nu t) \exp(-\lambda t^2) dt \right\rangle. \quad (7.8)$$

Due to the energy-time uncertainty principle, the resolution of the spectral line $\Delta\nu$ is inversely proportional to the observation time t_{obs} . The finite integration time t_{obs} and a non-zero value of λ will give a Gaussian-like contribution for each mode, leading to a broadening of the vibrational spectrum [164]. The effect of the choice of λ has been studied by Oligschleger et al. on selenium [162]. It was shown that the resolution of the frequency spectra increases with decreasing damping factor λ , and more and more details of the DOS of the finite-sized system become visible.

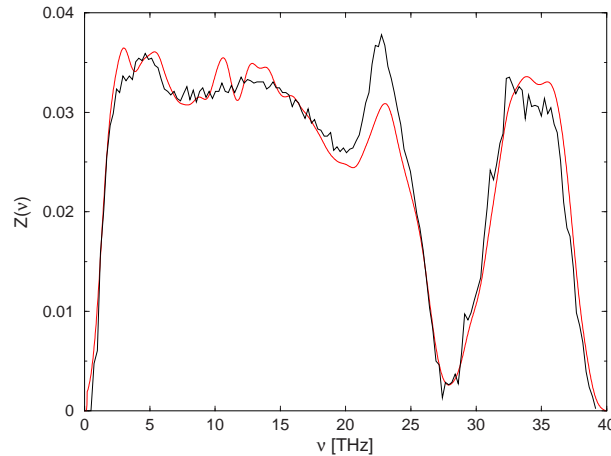


Figure 7.1: Vibrational DOS $Z(\nu)$ vs. frequency ν obtained by the diagonalization of the dynamic matrix (black-colored line) and by the Fourier transformation of the velocity autocorrelation function at temperature 10 K (red-colored line) averaged over 10 configurations.

Fig. 7.1 shows the vibrational density of states $Z(\mathbf{v})$ obtained by both the above mentioned methods for the ten structures with an average PEC of 50 %, which is a subset of the 20 generated configurations of partially crystalline forms. In the collection of ten such structures the lowest and highest value of PEC taken into account was 47 % and 52%, respectively. In order to obtain the vibrational density of states by the Fourier transformation of the velocity autocorrelation function, the equations of motions were integrated with a time step of 0.1 fs for a time interval $t_{obs}=1.00$ ps. Ten sets of initial conditions with a temperature of 10 K and a damping factor $\lambda = 4/t_{obs}^2$ were chosen. The overall shapes of the spectra are very similar. Details, e.g., more or less pronounced peaks observed for the Fourier Cosine Transformation depend on the number of sampled systems, the choice of λ and the length of the observation time [162]. In contrast to the diagonalization of the dynamic matrix the approach also accounts for relaxation and temperature effects, i.e., a complete agreement is not to be expected. The elastic constants c_{11} and c_{44} are found to be 7.03×10^{10} N/m² and 5.77×10^{10} N/m², respectively, for the systems with the mass density of 1.785 g/cm³. Hence the calculated sound velocities c_l and c_t are 6275 m/s and 5687 m/s, respectively. The percentage of anisotropy seen in terms of elastic constants in the system is found to be less than 7%, hence, the system can be considered to be isotropic for all practical purpose. At this point we want to mention that we also calculated the sound velocities c_l and c_t using potentials designed by Vashishta [165]. We obtain the values 5181 m/s and 3358 m/s for c_l and c_t , respectively. Despite of yielding a good description for the structural [159, 124] and vibrational [127] properties, it was shown that the potential by Kramer *et al.* used in the present simulation, yields somewhat less accurate elastic properties in zeolite [124]. For sodalite the values of c_{11} , c_{44} , c_{12} were overestimated by 30%, 8% and 72%, respectively. As a consequence the values obtained for the sound velocities in our simulation also seem to be at the higher end. Nevertheless we decided to use the potential of Kramer *et al.* since it yielded the experimentally observed characteristic structure of the high-energy spectrum of silica [127], whereas this is not the case for the one of Vashishta *et al.* [149].

In Fig. 7.2 we analyzed the motion of single elements and their contribution to the vibrational DOS obtained by the Fourier transformation of the element-specific velocity autocorrelation function given by

$$Z^A(\mathbf{v}) = \left\langle \frac{2}{\pi} \int_0^{t_{obs}} g^A(t) \cos(2\pi \mathbf{v}t) \exp(-\lambda t^2) dt \right\rangle \quad (7.9)$$

where

$$g^A(t) = \sum_{n=1}^{N_A} \frac{\langle \mathbf{v}^A(t) \cdot \mathbf{v}^A(0) \rangle}{\langle \mathbf{v}^A(0) \cdot \mathbf{v}^A(0) \rangle}. \quad (7.10)$$

Here N_A represents the number of atoms of type A. It is easy to see that the motions of oxygen atoms contribute dominantly for all frequency regions in the vibrational DOS. Nevertheless, the contributions of the silicon atoms become quite significant and comparable in magnitude for a peak in the mid-frequency region, i.e., around 24

THz. By MD simulations of silica glasses it was shown that the contribution of the silicon atoms even exceeds that of the oxygen atoms for this particular peak [149].

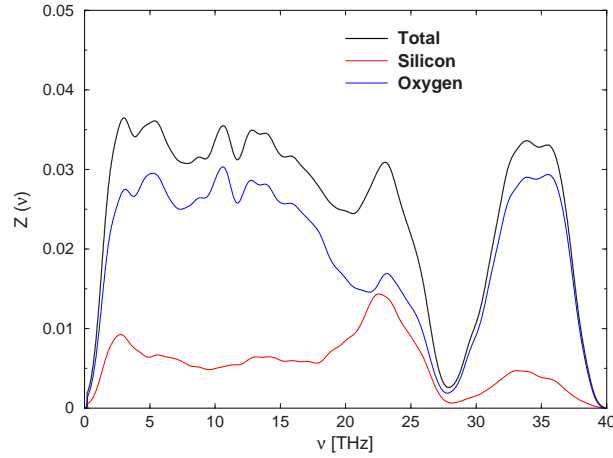


Figure 7.2: Averaged element specific-contribution to the total vibrational DOS for 10 configurations with an average PEC of 50% obtained by the Fourier transformation of the velocity autocorrelation function. Total vibrational DOS (black-colored line), Si contribution (red-colored line) and O contribution (blue-colored line) are plotted versus frequency in THz.

The best known anomalous low-temperature property of amorphous materials is their specific heat as mentioned in Chapter 4. In crystals the observed specific heat is directly proportional to T^3 and the proportionality constant is determined by the velocities of sound. In an amorphous system due to the presence of additional modes one observes deviations from this behavior. In the harmonic approximation C_V per atom is expressed in terms of the DOS as given in Eq. (4.34). In Fig. 7.3 we plotted the specific heat as C_V/T^3 as a function of temperature T . The dashed line shows the values obtained for the spectrum by adding the Debye contribution up to a frequency smaller than the lowest possible vibrational frequency seen in our system, i.e., 0.7 THz. This correction amounts to 1.8×10^{-3} of all the modes.

7.2 Analysis of the Vibrational Modes

7.2.1 Element specific motion with respect to bonds

In Fig. 7.2 the relative contributions of oxygen and silicon atoms to the vibrational DOS is presented. To learn about the typical motions of these components we calculated the angle between the displacement of atom i in mode j and the bond of this atom

to its nearest neighbor k , i.e., $\mathbf{r}_{bond} = \mathbf{r}_{ik}$,

$$\alpha_{e_{ibond}} = \arccos \left(\frac{\mathbf{e}_i^j \cdot \mathbf{r}_{bond}}{|\mathbf{e}_i^j| |\mathbf{r}_{bond}|} \right) \quad (7.11)$$

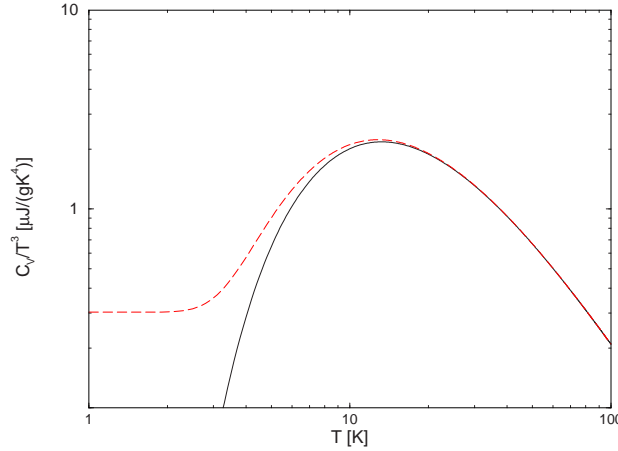


Figure 7.3: The specific heat as C_V/T^3 plotted versus the temperature T in a double-logarithmic scale. The black-colored solid line shows the contributions of the spectrum of the partially amorphous structures derived from zeolite with an average value of PEC of 50 % and the red-colored dashed line is the one with the Debye correction.

The element-specific weighted-average angle distribution for ten configurations with an average value of PEC of 50% is presented in Fig. 7.4. In order to suppress the small contributions of only slightly moving atoms we weighted the distribution with e_i^2 . For both the components, i.e., silicon and oxygen, the distributions are peaked at 90° . This hints that the motions of both silicon (significantly) and oxygen (mainly) atoms are perpendicular to the bonds. The fact that the distribution for oxygen atoms is more sharp than the distribution of silicon atoms indicates that the silicon atoms have some contributions to the motion which are either not parallel or perpendicular to the bonds, but in between. The distribution of α_{ebond} for oxygen atoms has three significant peaks at 10° , 90° and 170° with an approximate ratio of the peak height of 1:2:1. This ratio can be explained by the significant contributions of oxygen atoms to the asymmetric stretching motions of SiO_4 units (cf. below).

7.2.2 Relative contribution of motions of structural subunits to DOS

In order to investigate the atomic motions for different eigenmodes we follow the method used by Taraskin and Elliot, where one projects the eigenvectors onto various vibrational modes of the typical structural subunits [166]. In order to analyze the motion of Si and O atoms we consider two basic structural subunits Si-O-Si and SiO₄, with the approximate local point group symmetries C_{2v} and T_d , respectively. For the Si-O-Si (assuming O at rest) and SiO₄ (assuming Si at rest) subunits the components of the vibrational vectors for stretching (**S**) and bending (**B**) are given in Table 7.1 and Table 7.2, respectively.

Since the mentioned vibrational vectors in Table 7.1 and Table 7.2 describe the motion of the structural subunit using internal coordinates, the relative displacement eigenvectors $\mathbf{u}_{i(i_0)}^j$ are used for an atom i and are given for the j th mode by

$$\mathbf{u}_{i(i_0)}^j = (\mathbf{u}_i^j - \mathbf{u}_{i_0}^j) / \sqrt{(C_{i_0}^j)}. \quad (7.12)$$

Table 7.1: Vibrational vectors for Si-O-Si subunits (assuming O at rest) are presented below. The Si-O-Si subunits have two nondegenerate vibrational vectors of A_1 symmetry corresponding to the symmetric stretching and bending motions and one vibrational vector of B_1 symmetry for asymmetric stretching. In the following, the index i_0 represents the central immobile oxygen atom and the subscripts 1 and 2 refer to the silicon atoms. $\hat{\mathbf{a}}_1$ is the unit vector directed from atom i_0 to atom 1. $\hat{\mathbf{b}}_{12}$ is the unit vector perpendicular to the bond between atoms i_0 and 1, lying in the Si-O-Si plane and pointing as much as possible in direction of atom 2, i.e., $\hat{\mathbf{a}}_1 \cdot \hat{\mathbf{b}}_{12} = 0$ and $\hat{\mathbf{a}}_2 \cdot \hat{\mathbf{b}}_{12} \geq 0$. The superscripts in the vibrational vectors represent the symmetry of the modes. Note that the second component of the vibrational vectors represents the motion of oxygen which is the central, immobile and reference atom of the subunit. The first and third entries of the vibrational vectors refer to the motions of silicon atoms connected to the reference atom.

Vibrational vector	Components of the vibrational vector
$\mathbf{S}_{(i_0)}^{(A_1)}$	$\frac{1}{\sqrt{2}} \{\hat{\mathbf{a}}_1, 0, \hat{\mathbf{a}}_2\}$
$\mathbf{S}_{(i_0)}^{(B_1)}$	$\frac{1}{\sqrt{2}} \{\hat{\mathbf{a}}_1, 0, -\hat{\mathbf{a}}_2\}$
$\mathbf{B}_{(i_0)}^{(A_1)}$	$\frac{1}{\sqrt{2}} \{\hat{\mathbf{b}}_{12}, 0, \hat{\mathbf{b}}_{21}\}$

Table 7.2: Vibrational vectors for SiO_4 subunits (assuming Si at rest) are presented below. The SiO_4 subunits have one vibrational vector with A_1 symmetry for a symmetric stretching motion, two triplets for asymmetric stretching and bending motions of F_2 symmetry and a doublet for bending of E symmetry. In the following, the index i_0 represents the central immobile reference atom, i.e., the silicon atom of the SiO_4 subunit whose motion is described by the first component in all the vibrational vectors. The other four components refer to the motions of the oxygen atoms connected to the reference silicon atom i_0 and are numbered as 1, ..., 4 as a subscript. X and Y are the normalization constants used for the bending vibrational vectors of E symmetry.

Vibrational vector	Components of the vibrational vector
$\mathbf{S}_{(i_0,1)}^{(A_1)}$	$\frac{1}{\sqrt{4}}\{0, \hat{\mathbf{a}}_1, \hat{\mathbf{a}}_2, \hat{\mathbf{a}}_3, \hat{\mathbf{a}}_4\}$
$\mathbf{S}_{(i_0,1)}^{(F_2)}$	$\frac{1}{\sqrt{4}}\{0, \hat{\mathbf{a}}_1, \hat{\mathbf{a}}_2, -\hat{\mathbf{a}}_3, -\hat{\mathbf{a}}_4\}$
$\mathbf{S}_{(i_0,2)}^{(F_2)}$	$\frac{1}{\sqrt{4}}\{0, \hat{\mathbf{a}}_1, -\hat{\mathbf{a}}_2, -\hat{\mathbf{a}}_3, \hat{\mathbf{a}}_4\}$
$\mathbf{S}_{(i_0,3)}^{(F_2)}$	$\frac{1}{\sqrt{4}}\{0, \hat{\mathbf{a}}_1, -\hat{\mathbf{a}}_2, \hat{\mathbf{a}}_3, -\hat{\mathbf{a}}_4\}$
$\mathbf{B}_{(i_0,1)}^{(F_2)}$	$\frac{1}{\sqrt{4}}\{0, \hat{\mathbf{b}}_{12}, \hat{\mathbf{b}}_{21}, -\hat{\mathbf{b}}_{34}, -\hat{\mathbf{b}}_{43}\}$
$\mathbf{B}_{(i_0,2)}^{(F_2)}$	$\frac{1}{\sqrt{4}}\{0, \hat{\mathbf{b}}_{14}, -\hat{\mathbf{b}}_{23}, -\hat{\mathbf{b}}_{32}, \hat{\mathbf{b}}_{41}\}$
$\mathbf{B}_{(i_0,3)}^{(F_2)}$	$\frac{1}{\sqrt{4}}\{0, \hat{\mathbf{b}}_{13}, -\hat{\mathbf{b}}_{24}, \hat{\mathbf{b}}_{31}, -\hat{\mathbf{b}}_{42}\}$
$\mathbf{B}_{(i_0,1)}^{(E)}$	$X\{0, 2\hat{\mathbf{b}}_{12} - \hat{\mathbf{b}}_{13} - \hat{\mathbf{b}}_{14}, 2\hat{\mathbf{b}}_{21} - \hat{\mathbf{b}}_{23} - \hat{\mathbf{b}}_{24},$ $2\hat{\mathbf{b}}_{34} - \hat{\mathbf{b}}_{31} - \hat{\mathbf{b}}_{32}, 2\hat{\mathbf{b}}_{43} - \hat{\mathbf{b}}_{41} - \hat{\mathbf{b}}_{42}\}$
$\mathbf{B}_{(i_0,2)}^{(E)}$	$Y\{0, (\hat{\mathbf{b}}_{13} - \hat{\mathbf{b}}_{14}), -(\hat{\mathbf{b}}_{23} + \hat{\mathbf{b}}_{24}),$ $(\hat{\mathbf{b}}_{31} - \hat{\mathbf{b}}_{32}), -(\hat{\mathbf{b}}_{41} + \hat{\mathbf{b}}_{42})\}$

Here $C_{i_0}^j$ is the norm given by

$$C_{i_0}^j = \sum_i |\mathbf{u}_i^j - \mathbf{u}_{i_0}^j|^2. \quad (7.13)$$

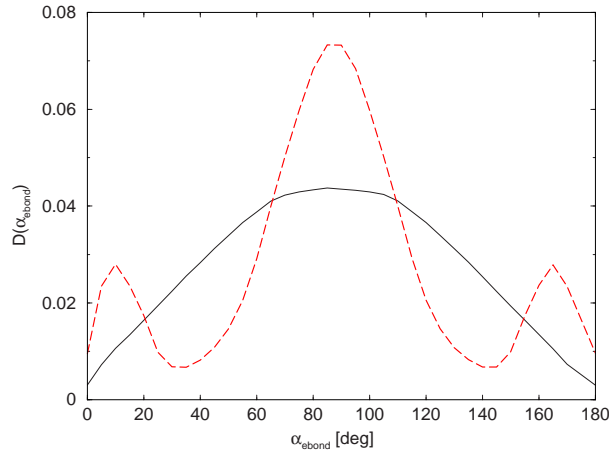


Figure 7.4: Distribution of element-specific weighted-average angles α_{ebond} between the atomic displacement eigenvectors and the bonds. The black-colored solid line corresponds to the angle distribution of silicon atoms and the red-colored dashed line to the one of oxygen atoms for ten configurations with an average value of PEC 50%.

The displacement eigenvectors \mathbf{u}_i^j are derived from the eigenvectors \mathbf{e}_i^j as $\mathbf{u}_i^j = \mathbf{e}_i^j / \sqrt{M_i}$ with the mass M_i of the i th atom. Here i_0 represents the central, immobile, reference atom for the structural subunits. The squared value of the projection of the relative displacement eigenvector $\mathbf{u}_{i(I,i_0)}^j$ onto the vibrational vectors $\mathbf{D}_{i(I)}$ (\mathbf{S} 's and \mathbf{B} 's in Table 7.1 and Table 7.2) of the structural subunit I gives the partial contribution of the vibrational motion of a specific kind for the eigenmode j . These squared projections were averaged over all structural subunits as

$$(r_{\mathbf{D}}^j)^2 = \frac{\sum_I (w_I^j)^2 (\sum_{i'(I)} \mathbf{u}_{i'(I,i_0)}^j \cdot \mathbf{D}_{i'(I)})^2}{\sum_I (w_I^j)^2}. \quad (7.14)$$

Here the index I runs over all the structural units, i.e., Si-O-Si or SiO_4 , and the index i' runs over all the atoms comprising the structural subunit. The weighting factor w_I^j is used in order to suppress the contributions of units which have negligible values and is given by

$$w_I^j = \left(\sum_{i'} |\mathbf{e}_{i'}^j|^2 \right)^{1/2}. \quad (7.15)$$

In order to obtain the rotational component of the spectrum, we obtain three perpendicular axes for a given subunit as eigenvectors by diagonalizing the shape tensor given by

$$G_{\alpha\beta}(i_0) = \sum_{i'} M_{i'} r_{i_0 i'}^\alpha r_{i_0 i'}^\beta. \quad (7.16)$$

Here for a given central atom i_0 in a structural subunit the index i' runs over other atoms connected to i_0 . $M_{i'}$ represents the mass of the i' th atom and $r_{i_0i'}^\alpha$ refers to the distance in α direction between the i_0 th and i' th atom. The squared weighted projection of the displacement eigenvectors onto the rotational vectors around the three perpendicular axes summed and averaged over all the subunits gives the contribution of the rotational motion.

In Fig. 7.5 we show the partial vibrational DOS obtained by the projections onto the vibrations of the Si-O-Si and SiO₄ subunits which are averaged over all subunits in all ten configurations with an average PEC of 50 %. The percentages of the individual contributions were determined by integrating the DOS over the frequency ν , where we also assessed low-frequency (high-frequency) contributions by integrating up to (from) the minimum in the DOS at ≈ 28 THz (Table 7.3). The contributions by rotational and bending motions are significant for both subunits. For Si-O-Si (Fig. 7.5(a)) rotational motions contribute to the DOS for the entire frequency range and become very significant for the low-frequency region (47.7 %) with a maximum around 3 THz. The rotational motions of the Si-O-Si subunits have strong contributions and hence in Fig. 7.4 we find that the distribution for the element specific weighted-average angles α_{bond} shows a maximum around 90° for the silicon atoms. The bending modes contribute also quite significantly for the low-frequency region (29.9 %). The symmetric stretching motions exhibit a maximum at 23 THz, but their overall contribution is not so dominating (7.6 %). The high-frequency region is mostly dominated by the asymmetric stretching motions (54.1 %) and has a broad maximum around 33 THz. In contrast to the vibrational features obtained for silica, where one observes a sharp splitting of both rotational and asymmetric stretching motions in high frequency peaks, this is quite diminished in case of the amorphized form derived from zeolite [166].

Fig. 7.5(b) shows the corresponding projection onto the SiO₄ subunits. Similar to the Si-O-Si subunits, the rotational motions of the SiO₄ subunits become quite dominant (34.0 %) in the beginning of the low-frequency region and exhibit a maximum at 5 THz. The bending motions are significant for the end of the low-frequency region (40.7 % for F_2 type and 19.2 % for E type). The bending motions with E type have a broad maximum at 14 THz and a small maximum at 22 THz. In silica this bending motion has just one broad maximum at 15 THz [166].

For the bending motion of F_2 type we observe two peaks, one with a flat maximum around 17 THz and another sharp maximum at 23 THz. In silica this sharp peak is found to be missing [166, 167]. For the partially amorphous system studied here one sees a very strong contribution of the asymmetric stretching motions around 32 THz in the high-frequency region (65.8 %). The symmetric motions contribute weakly for the whole spectrum (4.1 %). A slightly forked feature of the DOS in the high-frequency region is mainly due to the existence of the symmetric and asymmetric stretching motions of the SiO₄ subunits. Due to the occurrence of a very sharp peak for the asymmetric motions and a strong peak for the rotational motions one can explain the peaks observed for the distribution of element specific weighted-average angles

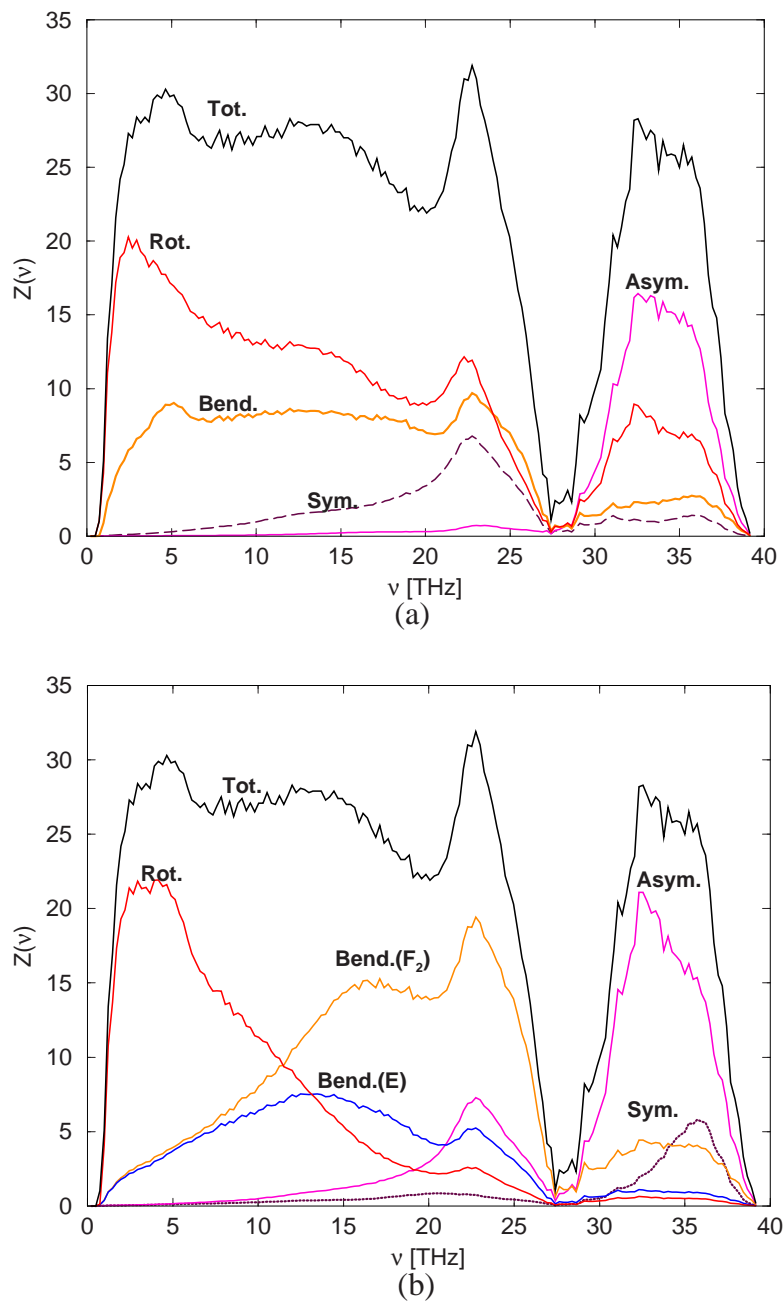


Figure 7.5: (a) The total and partial vibrational DOS obtained by the projection of the relative atomic displacements onto the vibrational vectors of the (a) Si-O-Si and (b) SiO₄ subunits. All the plots are shown as an average over 10 configurations with an average value of PEC of 50 %.

α_{ebond} for oxygen at 10° , 90° and 170° . 10° and 170° are related to the strong asymmetric stretching motions and 90° is related to the dominant low-frequency rotational motions. A small contribution occurring at the band gap, i.e., around 28 THz, comes mainly from the bending motions of both E and F_2 types.

Table 7.3: Partial contributions of the eigenmodes of the subunits (Si-O-Si and SiO_4) calculated by the integration of respective DOS each related to the low- frequency, high-frequency part of the spectrum and the total spectrum displayed in Fig. 7.5 (numbers presented below are in percentage).

Subunit	Motion	Below 28 THz	Above 28 THz	Total
Si-O-Si	Sym.	8.2	5.4	7.6
	Asym.	0.9	54.1	12.7
	Bend.	29.9	10.8	25.7
	Rot.	47.7	29.1	43.6
SiO_4	Sym.	1.4	13.5	4.1
	Asym.	7.3	65.8	20.2
	Bend.(F_2)	40.7	17.9	35.6
	Bend.(E)	19.2	4.2	15.9
	Rot.	34.0	2.2	27.0

7.2.3 Mode localization

In order to determine the degree of localization of phonons there are two commonly used concepts, i.e., the effective mass and the participation ratio [168, 169]. The effective mass is defined as

$$M_{eff}^j = M_{i'} / |\mathbf{e}_{i'}^j|^2, \quad (7.17)$$

where i' corresponds to an atom with largest displacement and with a real eigenvector $\mathbf{e}_{i'}^j$ for the j th mode. However, this concept is not suitable for the description of the localization of the modes in the case of large systems. For localized modes M_{eff} is a system independent quantity but for the extended modes its value scales with the system size. The participation ratio is given in terms of the eigenvectors as

$$p^j = \left(N \sum_{n=1}^N |\mathbf{e}_n^j|^4 \right)^{-1}. \quad (7.18)$$

For the extended modes, p is unity and for the localized or quasi-localized modes it scales inversely with the system size.

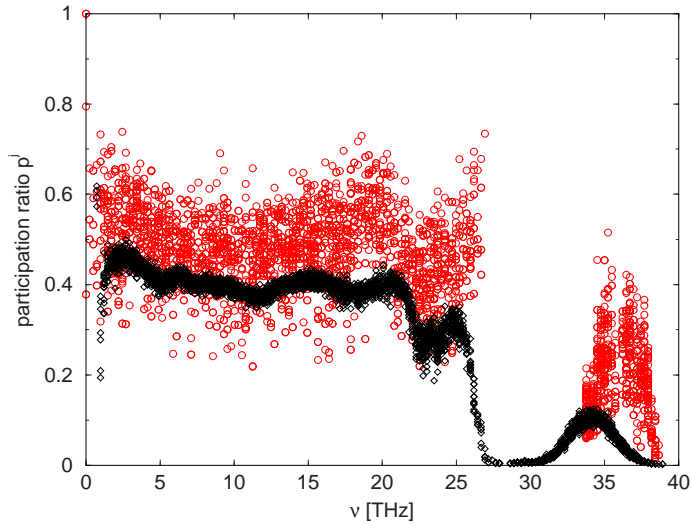


Figure 7.6: Comparison of participation ratios of the crystalline (red-colored circles) and amorphous systems with PEC of 50% (black-colored plus).

Fig. 7.6 shows the comparison of participation ratios of the crystalline form and the partially amorphized form obtained from a configurational average over 10 structures with an average PEC of 50%. One can see easily that amorphization leads to a remarkable localization of the modes at the tails of the high-frequency modes and at very low-frequency modes, i.e., around 1 THz. At 0.7 THz one observes very few modes with high participation number, i.e., around 0.6. These correspond to the extended modes, i.e., the lowest-lying phonons permitted by the system size. Similar to other theoretical simulations on amorphous silica systems [166, 167, 161], we see a very strong localization of the modes with effective mass centered on 2 atoms at the tail regions of the high-frequency modes. For the low-frequency modes the strongest localization is centered around 8 atoms with a participation ratio as low as 0.2. These modes are formed by the interactions of localized modes and phonons and hence referred to as quasi-localized modes [170]. Localized and quasi-localized vibrations are well-known phenomenon in the phonon theory of crystals with impurities or defects [171]. The localized vibrations occur outside the continuum of the lattice frequency, do not interact with the lattice modes and their eigenvectors decay exponentially with the distance. In amorphous systems this type of vibrations are seen in the the high-frequency tail. Defects and localized vibrations are also possible at the low-frequency regime where the DOS is quite low. These types of localized modes would hybridize with extended acoustic modes, lose their strict localized nature of the vibrations and are referred to as quasi-localized modes. Similar to the localized modes occurring at the tails of the high-frequency regime, these modes are localized near the

defects. However, their eigenvectors do not decay exponentially [98].

Similar to the analysis of Jin *et al.* we calculated the effective radius of gyration R_{gyr}^j for the j th mode as

$$R_{gyr}^j = \sqrt{\frac{1}{3} \sum_{\alpha} [\langle X_{\alpha}(j)^2 \rangle - \langle X_{\alpha}(j) \rangle^2]}, \quad (7.19)$$

where

$$\langle X_{\alpha}(j)^2 \rangle = \sum_{i=1}^N |e_{i\alpha}^j|^2 (r_{i\alpha} - r_{i\alpha}^j)^2 \quad (7.20)$$

and

$$\langle X_{\alpha}(j) \rangle = \sum_{i=1}^N |e_{i\alpha}^j|^2 (r_{i\alpha} - r_{i\alpha}^j). \quad (7.21)$$

Here i' refers to an atom with the largest displacement for the j th mode. For a localized mode involving essentially only the motion of a single atom R_{gyr} will be zero and for an extended mode it is the average root-mean-squared distance [161]. Fig. 7.7 shows R_{gyr}/L for various frequencies. The average box length L is 28.8 Å. The average radius of gyration for the quasi-localized low-frequency modes are approximately 0.3 times of the box length. However, for the high-frequency region the modes especially at the tails become highly localized, i.e., within 0.01 times the box length.

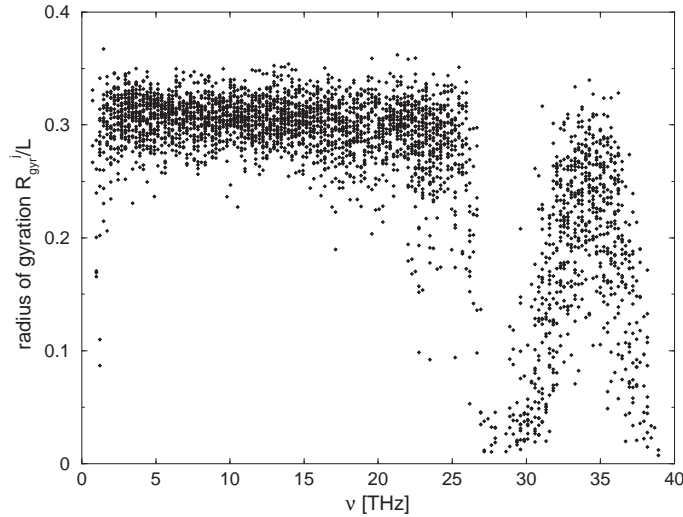


Figure 7.7: Plot of radius of gyration as R_{gyr}/L versus frequency with L as length of the simulation box.

7.2.4 Phase quotient

In order to determine the behavior of the correlation between the individual atomic displacements, we analyzed the phase quotients of the modes. Phonons in a crystal can be distinctly classified as acoustic and optical modes. In purely acoustic modes adjacent atoms move in phase, while in the optical modes their motions are out of phase. Since in amorphous structures the modes cannot be specified by wave-vectors such classification is not justified in strict sense. However, one can associate a phase character to a mode j by a so-called weighted phase quotient defined as

$$q^j = \frac{1}{\sum_i |\mathbf{e}_i^j|^2} \sum_i \sum_{i'} \frac{\mathbf{u}_i^j \cdot \mathbf{u}_{i'}^j}{|\mathbf{u}_i^j| \cdot |\mathbf{u}_{i'}^j|} \cdot |\mathbf{e}_i^j|^2. \quad (7.22)$$

Here i and i' run over all the silicon atoms and the neighboring oxygen atoms, respectively. For the in-phase acoustic-like modes the phase quotient is close to unity and for the out-of-phase optic-like modes its value is close to minus unity [161, 166].

In Fig. 7.8 we show the weighted phase quotient for the modes with respect to the frequencies. The phase quotients tend to unity with the decrease in frequency indicating the acoustic character of the modes increases upon decrease of the frequencies. In the high-frequency region the phase quotients are mainly negative and show significant optic-like character.

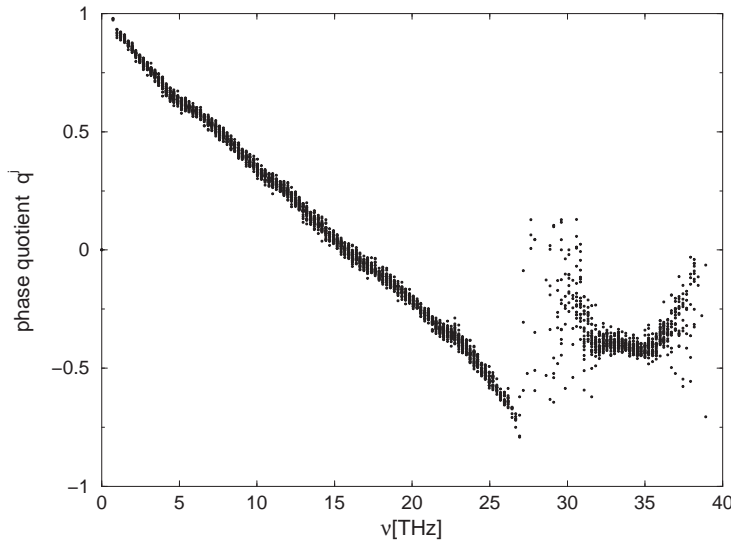


Figure 7.8: Weighted phase quotient vs. frequency.

7.3 Effect of Extent of Amorphization on Vibrational DOS

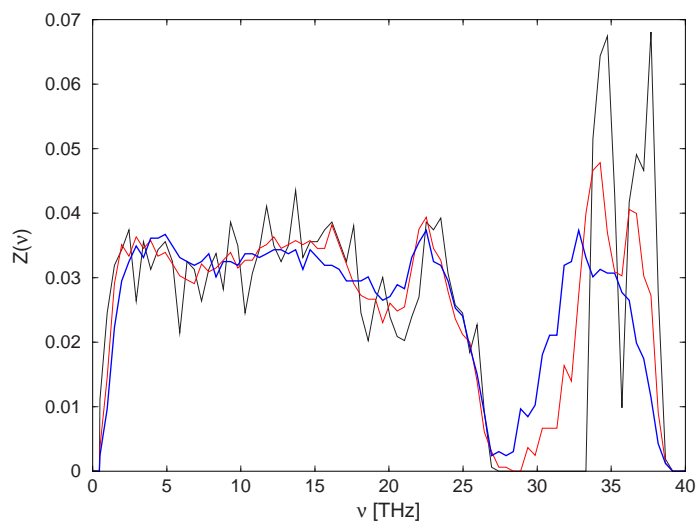


Figure 7.9: Vibrational DOS obtained by diagonalization of the dynamic matrix for different PEC obtained from ZSM-5 versus frequency. The black-colored line refers to the vibrational DOS for the crystalline ZSM-5 and the red-colored line represents the density of states obtained for the structures with PEC of 70 % and the blue-colored line for the structures with PEC of 50 %.

Fig. 7.9 we analyzed the change in the vibrational DOS with different PEC. It was found that the structures with PEC less than 50% show very similar features of vibrational DOS as those of the ones obtained with PEC of 50%. In order to have a not too crowded figure we present the dependence of the PEC on the vibrational DOS for crystalline ZSM-5 and partially amorphous structures with the PEC of 70% and 50%. At this point we want to mention that the calculated vibrational DOS of silicalite, using the interatomic potentials of Kramer *et al.* [124] are in good agreement with the DOS measured experimentally using the inelastic neutron scattering spectrum obtained by Jobic *et al.* [172]. The high-frequency double peak obtained in our simulation at 34 THz and 37 THz was experimentally observed at 33 THz and 36 THz, respectively. The generalized force field used in previous simulations could not reproduce the forked nature of the high-frequency peaks [173, 172]. The peaks at the mid-frequency region seen at 16 THz and 23 THz were observed experimentally at 16.5 THz and 22.5 THz, respectively. We see that the amorphization has a significant effect on the intensities and leads to a broadening of the high-frequency peak. There is also shift in the peaks of the high-frequency region towards lower frequency with a narrowing of the band gap. The low-frequency region shows a relatively small dependence on the PEC.

It has been shown by Kosanovic *et al.* that during amorphization by ball milling experiments the absorbance at 16.5 THz was reduced [19]. Jacobs *et al.* assigned this peak as asymmetric stretching mode of distorted double five membered rings present

in the zeolitic framework and suggested this band as a probe for detecting the presence of a zeolitic framework [160]. In Fig. 7.9 we do see a slight decrease of the intensity of the peak at 16.1 THz. But this change is not so drastic for the structures below 50% PEC and could be justified by the ring distribution of five membered rings. On analysis of the ring distribution we find that the percentage of 5-fold rings reduces from 49% for the crystalline form to 38% for a structure with PEC of 79% and to 21% for a structure with PEC of 60%. It remains roughly constant at a value of 29% for structures of PEC below 50% [159].

7.4 Low-Frequency Vibrational Excitations

The origin and nature of the low-frequency vibrations in (partially) disordered materials as well as their influence on low-temperature thermodynamic properties such as specific heat and thermal conductivity is still not fully understood and under debate [90, 174]. Especially the so-called boson-peak (BP) in the reduced DOS $Z(\nu)/\nu^2$, which is traditionally associated with a vibrational DOS exceeding the Debye value around 1 THz, remains a subject of theoretical controversy (cf. Ref. [175] and references therein). The reduced DOS is shown in Fig. 7.10(a) for five selected structures with different PEC (representatives for a total of 30 structures studied). The maximum of the reduced DOS in the BP region (0.5 THz to 1 THz) for 30 structures are plotted in Fig. 7.10(b). The two distinct ranges of PEC exhibiting opposite behavior of the intensity of the BP with respect to amorphization are observed: for structures with PEC of 100% (crystalline) to $\approx 60\%$, the intensity of the BP decreases with increasing amorphization and the opposite behavior is found for structures with PEC below $\approx 60\%$. In the following we try to explain these trends on the basis of the competition between various factors in the framework of Maxwell counting of floppy modes [176]. In a generic case, e.g., a general infinite system formed by linked rigid tetrahedra, an exact balance between the degrees of freedom and the number of constraints exists [177]. However, the zeolites fall into the category of non-generic cases, where the high symmetry present in these materials can make some constraints degenerate and allow for floppy modes [178]. Hammonds *et al.* have proposed the existence of a significant number of floppy modes with respect to the total number of modes in the zeolitic systems, thereby explaining the flexibility of the framework and its relation to the adsorption sites [179, 180].

Low-frequency modes for crystalline structure: In order to investigate the high intensity of the peak obtained for the crystalline system we generated the phonon dispersion curves along the symmetry directions of the orthorhombic unit cell of ZSM-5. The dispersion curve is obtained from the dynamic matrix in \mathbf{k} space and defined as

$$D_{ij}^{\alpha\beta}(\mathbf{k}) = \frac{1}{\sqrt{M_i M_j}} \sum_{kl} \frac{\partial^2 U}{\partial R_{ik}^\alpha \partial R_{jl}^\beta} \cdot \exp i\mathbf{k} \cdot (\mathbf{R}_{ik} - \mathbf{R}_{jl}). \quad (7.23)$$

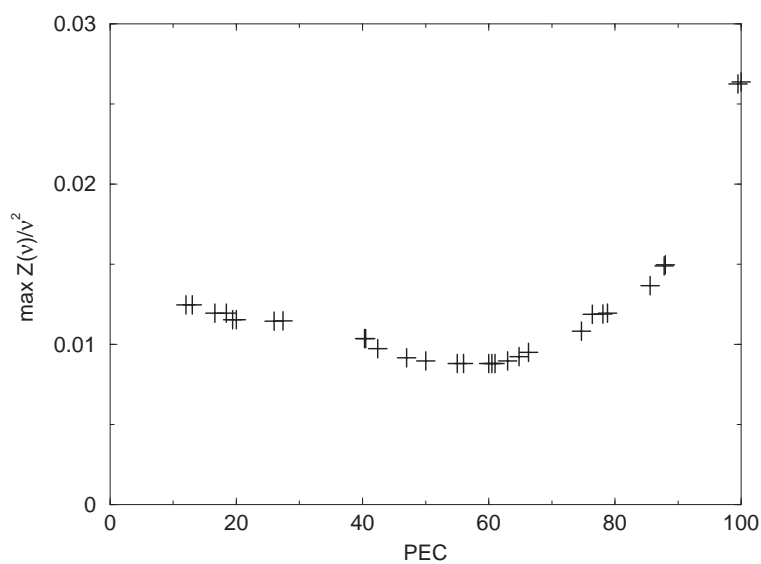
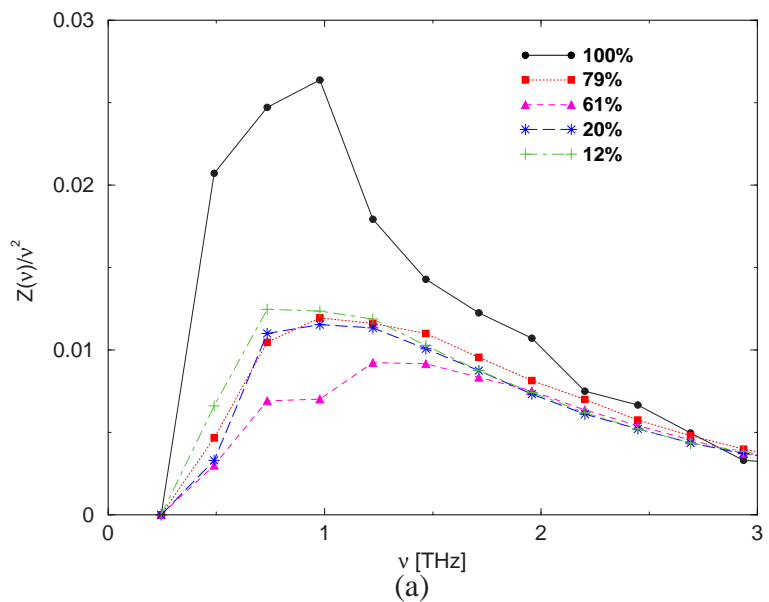


Figure 7.10: (a) $Z(v)/v^2$ vs. v for zeolite ZSM-5 based partially amorphous structures with different percentage of energy crystallinity. (b) Maximum value of reduced DOS obtained in BP region, i.e., $\max Z(v)/v^2$ for 30 structures.

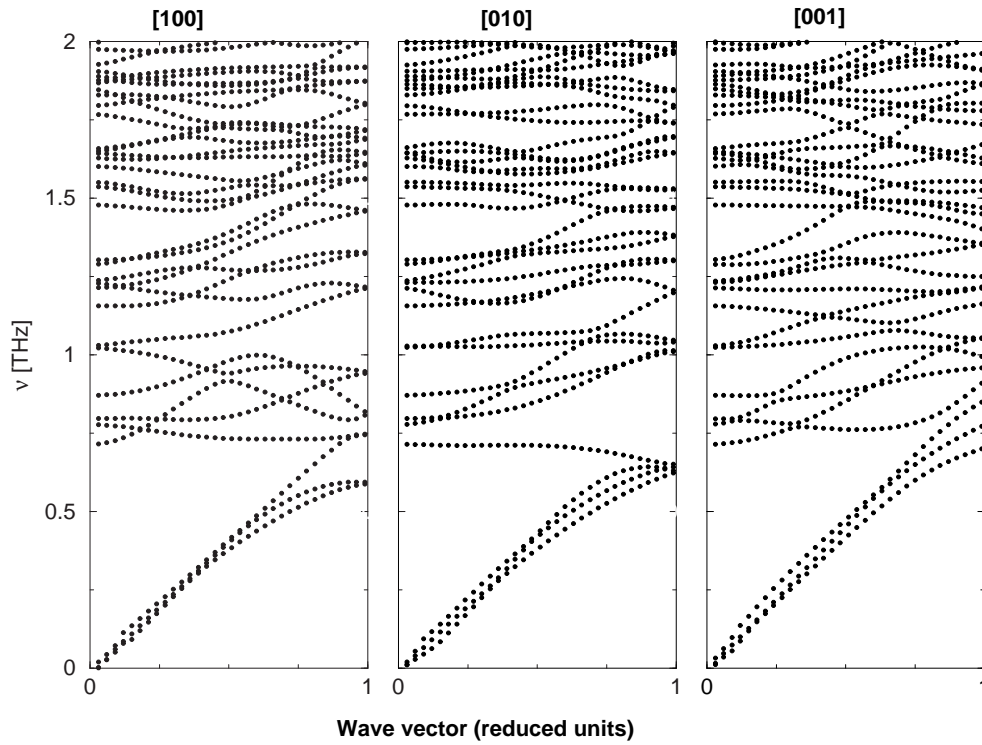


Figure 7.11: Phonon dispersion curves along the symmetry directions for the silicious ZSM-5.

Here α and β denote the Cartesian indices, k, l the unit cells, and i, j the sublattice. \mathbf{R}_{ik} and \mathbf{R}_{jl} are the atomic positions and M_i and M_j the atomic masses. The summation is over all cells l, k within the interaction sphere. Diagonalization of matrix $\mathbf{D}(\mathbf{k})$ yields as eigenvalues the squared phonon frequencies ν^2 . The calculated dispersion curve is shown in Fig. 7.11. Since ZSM-5 has a large unit cell of 288 atoms, it has a large number of optic modes along with three low lying acoustic modes. For the analysis only modes up to 2 THz are shown. The curves show that the peak obtained in Fig. 7.10 around 1 THz is due to the low-lying modes which are mainly optical in character. Since there is merging of the phonons of the acoustic branches with the optic ones the possibility of having hybridized modes cannot be neglected as proposed by Taraskin *et al.* for the case of vitreous silica [181].

Various factors may influence the modes associated with the BP as documented in the literature [182, 183, 184, 185]. It has been proposed by Nakamura *et al.* that buckling motions of mismatched rings (No. of Si in the ring $\neq 6$) could be related to the origin of the BP in vitreous silica. This was further supported on the basis of the suppression of the BP in densified silica and was related to the reduction in the number of these mismatched rings (regarded as floppy rings) [182]. A very intense hump present in the reduced specific heat vs. temperature (which has a relation to the BP [186]) for the zeolites belonging to the family of MFI and BEA in comparison to

vitreous silica and cristobalite, was associated with the presence of large 10-fold and 12-fold rings, respectively [183]. The degree of coordination defects was also found to influence the intensity of the BP. Finkemeier *et al.* showed for amorphous silicon that the intensity of the excess DOS increases upon introduction of defects by modifying the coordination numbers (CNs) [184, 185].

Table 7.4: The first line for each PEC gives the occurrence of n-fold rings in percent. In the second line, the quantity ρ describes the degree of puckering of the rings. The numbers in parentheses in the first column represent the average participation ratios of the modes in the BP region.

PEC	n = 2	3	4	5	6	7	8	9	10
100 (0.45)	-	-	2.9 1.01	48.9 1.06	39.2 1.13	-	-	-	9.0 1.09
90 (0.42)		0.4 1.04	4.8 1.04	45.3 1.08	38.1 1.15	2.3 1.23		0.9 1.12	8.2 1.11
79 (0.41)	1.0 1.00	2.6 1.04	9.0 1.06	37.7 1.09	33.4 1.16	8.2 1.22	2.4 1.23	1.9 1.19	3.8 1.12
61 (0.40)	1.8 1.00	7.2 1.09	14.9 1.10	24.7 1.20	31.7 1.37	14.2 1.22	3.2 1.22	1.4 1.22	0.9 1.28
47 (0.38)	3.1 1.00	9.1 1.04	15.8 1.08	27.8 1.15	25.9 1.55	12.5 1.22	3.0 1.23	2.1 1.33	0.7 1.28
20 (0.31)	3.9 1.00	11.8 1.07	16.4 1.15	25.7 1.27	26.6 1.53	10.7 1.27	2.8 1.31	1.4 1.32	0.7 1.40
12 (0.27)	4.5 1.00	13.8 1.15	17.8 1.21	26.0 1.32	28.4 2.78	5.5 1.30	2.2 1.47	1.2 1.46	0.6 1.54

In order to study the relationship between the above mentioned factors with the simulated behavior of the intensity of the BP in this letter, we present an analysis of ring statistics and CNs in Tables 7.4 and 7.5, respectively. Ring distributions were calculated by the procedure described in Chapter 6. \bar{r}_{avg} refers to the average of the radii of all n-fold rings in the system and \bar{r}_{min} refers to the average of the maximum radii below which atoms and molecules will be able to pass through these rings. A deviation of ρ from 1.00 quantifies the degree of ring puckering. We note here in passing that although in a partially amorphous system a higher degree of puckering will most likely correspond to a lowering of the symmetry, ρ cannot be regarded as a

measure of symmetry in a strict sense. In order to study the localization of the modes in the BP region (0.5 THz to 1.5 THz), average participation ratios calculated using the definition of Bell and Dean [169] are also presented in Table 7.4. The distribution of CNs of the most active 10% of the atoms in the modes contributing to the BP region selected on the basis of the magnitude of the mass-weighted eigenvectors is listed in Table 7.5.

Table 7.5: Distribution of the coordination numbers (CNs) in percent for the 10 % most active atoms present in the modes belonging to the BP region.

PEC	Si			O		
	CN = 4	CN > 4	CN < 4	CN = 2	CN > 2	CN < 2
100	1	-	-	99	-	-
90	5	0	0	94	0	1
79	7	0	0	89	0	4
61	14	0	0	81	0	5
47	17	0	1	68	0	13
20	17	0	1	59	1	23
12	17	0	2	55	1	25

Low-frequency modes for the structures with PEC above $\approx 60\%$: The modes in the BP region are found to be relatively delocalized with average participation ratios of 0.4 or larger. The most active atoms are mainly located around large 10-fold rings as shown in Fig. 7.12. For the crystalline system the large 10-fold rings are quite regular ($\rho \approx 1.09$, cf. Table 7.4). Amorphization causes a drastic disappearance of these rings (9% reduces to 0.9%) accompanied by a formation of 7-,8- and 9-fold mismatched large rings. However severe puckering of the rings takes place (ρ increases from 1.09 to 1.28) thereby reducing the possibility of having more regular and symmetric rings. In the framework of the model of the floppy modes, the presence of large rings alone without the additional effect of symmetry cannot break the basic balance between the constraints and the degrees of freedom and thus cannot give rise to the floppy modes [178]. Therefore these modifications described above result in a reduction of the number of floppy modes and thereby decrease the intensity of the BP.

Low-frequency modes for the structures with PEC below $\approx 60\%$: The possibility of having floppy modes due to the closed rings is quite low due to severe puckering ($\rho > 1.22$ for 7-fold and larger rings, cf. Table 7.4). A tremendous increase of the number of under-coordinated active atoms (5% to 27%, cf. Table 7.5) is observed. These are related to non-bridging Si-O bonds and 'open' rings. The resulting reduced

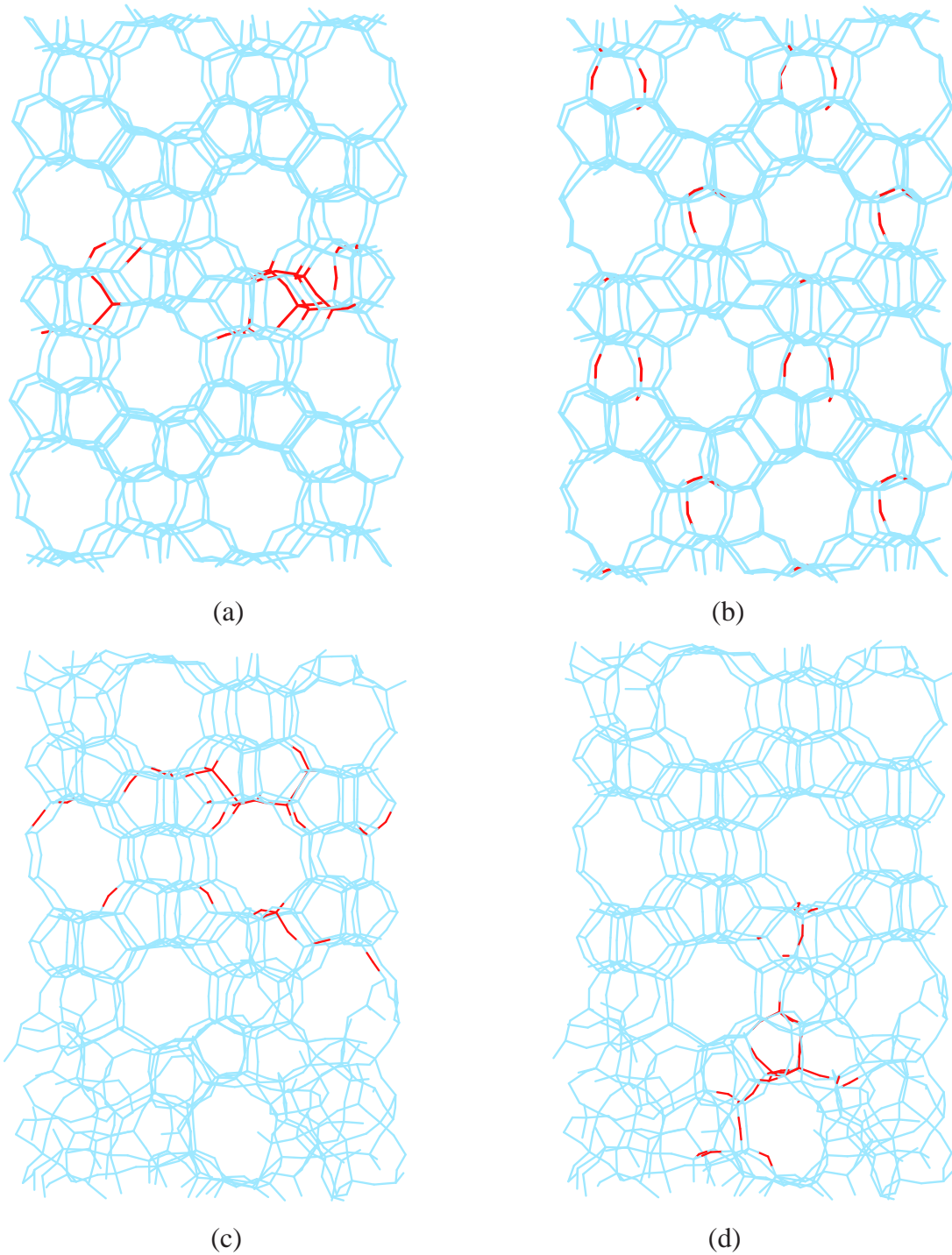


Figure 7.12: The active atoms shown by red lines of the modes at 0.5 THz and 1 THz in the structures with PEC of 100% ((a) and (b), respectively) and 73% ((c) and (d), respectively) in the yz plane.

number of constraints leads to an increase of the number of floppy modes. Note that for the structures with PEC larger than $\approx 60\%$ this effect is largely suppressed due to the much lower number of active under-coordinated centers. The average participation ratio decreases drastically on amorphization (from 0.40 to 0.27 for structures with PEC of 61% to 12%), with the formation of highly localized modes as shown in Fig. 7.13. The increased number of these localized floppy modes associated with under-coordinated centers causes most likely the increased intensity of the BP for this range of PEC.

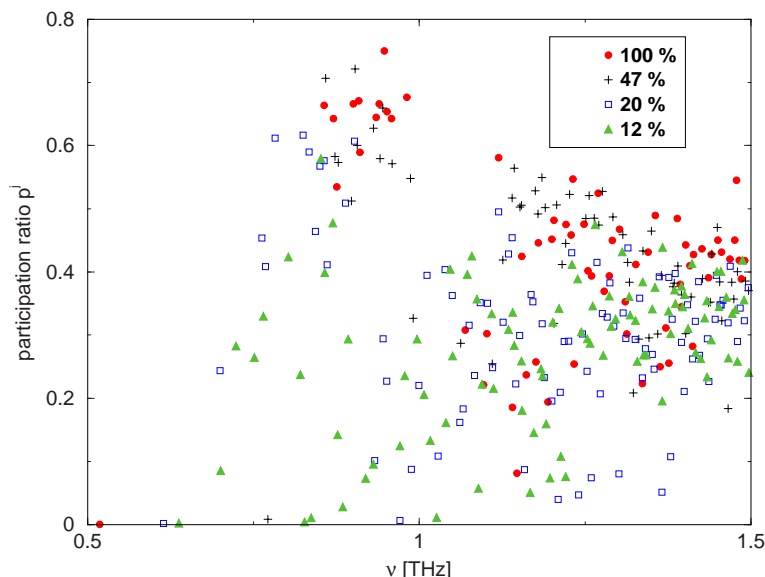


Figure 7.13: Participation ratios of the low-frequency modes of the partially crystalline structures corresponding to different PEC.

Nature of the vibrational motions in low-frequency modes: We performed an analysis similar to the one used by Taraskin and Elliot [166]. We projected the eigenvectors of the SiO_4 and Si-O-Si structural subunits (active subunits) containing active Si and O atoms onto the vibrational vectors of the ideal SiO_4 and Si-O-Si units with T_d and C_{2v} symmetry, respectively. The calculated contributions of the vibrational motions exhibited by the active subunits are shown in Table 7.6. Obviously the stretching motions of both kinds of active subunits contribute negligibly. For the active SiO_4 subunits the main contributions result from the rotational motions. However, for intermediate and low values of PEC the bending character contributes noticeably, indicating that distortions of the SiO_4 subunits are associated with these low-frequency modes. Hence the floppy modes are not in strict sense rigid unit modes in these systems. The motions of the active Si-O-Si structural units involve a strong mixing of both bending and rotational motions for the crystalline case (43% and 56%, respectively). Upon amorphization the bending character decreases and the vibrational motions become mainly rotational in nature. Since the BP occurring in the partially crystalline forms are in the

same frequency region as for the crystalline one, although with a reduced intensity as shown in Fig. 7.10, we predict that the modes are mainly optic in nature.

Table 7.6: Contributions (in percent) of the vibrational motions exhibited by the active subunits (SiO_4 and Si-O-Si) as described in the text. 'S', 'B' and 'Rot.' represent the stretching, bending and rotational contributions, respectively and the superscripts denote the symmetry of the motions.

PEC	SiO_4					Si-O-Si			
	S ^(A₁)	S ^(F₂)	B ^(F₂)	B ^(E)	Rot.	S ^(A₁)	S ^(B₁)	B ^(A₁)	Rot.
100	1	1	4	1	93	0	0	43	56
90	1	1	4	2	93	1	0	40	59
79	0	0	6	3	90	1	0	37	62
61	0	0	8	4	88	0	0	29	71
47	0	0	9	6	84	0	0	27	72
20	0	0	6	5	89	0	0	20	79
12	0	0	6	4	90	0	0	16	84

Hence, we conclude that in relatively high crystalline porous structures, the decrease in the intensity of the BP can be associated with the reduction in the number of the floppy modes due to the decrease in the concentration of the large membered rings and the lowering of their symmetry upon amorphization. The opposite behavior for relatively low crystalline structures is explained by the increased number of floppy modes due to the formation of non-bridging bonds and 'open' rings. Although there may exist other mechanisms which are not investigated in this thesis, floppy modes associated with 'open' rings and coordination defects have most likely a strong influence of the intensity of the BP in partially crystalline zeolitic systems.

This part of work is published in Refs. [187, 188]

Chapter 8

Relaxation Properties

Amorphous phases exhibit over an extremely broad range of time particular motional processes known as relaxations [189,190,191,192,193]. Classical relaxation in glasses, sometimes also called *secondary relaxation* to distinguish it from the primary relaxation at the glass transition, is generally believed to be well described in terms of the Arrhenius-Kramers picture [194], with a relaxation time τ given by the Arrhenius relation

$$\tau = \tau_0 \exp\left(\frac{E}{k_B T}\right), \quad (8.1)$$

where τ_0 is a macroscopic time of the order of 10^{-13} s, E is the energy of the barrier between two energy minima of the system. The secondary or β relaxations are envisaged as thermally activated transitions over the barriers separating the local minima in the potential energy landscape [195, 196, 197], thus an insight into the topography of the inherent structures can be obtained by investigating these relaxations [167, 198, 199].

In contrast, the primary relaxation process or α -process, the onset of the flow process at the glass transition temperature T_g and above, seems to follow a much steeper law [200, 201]

$$\tau = \tau_0 \exp\left(\frac{A}{(T - T_0)}\right), \quad (8.2)$$

where A and T_0 are constants with the dimension of temperature. This is the well known empirical Vogel-Fulcher-Tamman equation.

In the following sections we present a MD investigation of secondary relaxations occurring in our chosen model system, i.e., (partially) amorphous-forms derived from zeolite ZSM-5. The occurrence of these relaxations might change the level of crystallinity and hence, it can effect the selectivity of the reactions which are dependent on the percentage of crystallinity [28]. The dynamics show some interesting phenomena like aging and dynamical heterogeneities at the intermediate time scales studied (1 ps

to 0.6 ns). In all 20 structures with 3456 particles were chosen to study the relaxational dynamics below the critical temperature, T_c .

An estimate of T_c was obtained by calculating the diffusion constant D of the system as a function of temperature using the relation

$$D_\alpha = \lim_{t \rightarrow \infty} \frac{1}{6t} \langle |\mathbf{R}_\alpha(0) - \mathbf{R}_\alpha(t)|^2 \rangle. \quad (8.3)$$

Here $\mathbf{R}_\alpha(t)$ is the time-dependent position vector of a particle of type $\alpha \in \{\text{Si}, \text{O}\}$ and $\langle \dots \rangle$ denotes the configurational average. In Fig. 8.1 one can observe that the temperature dependent diffusion constants for both silicon and oxygen atoms show a rapid drop below 4000 K, which can be taken as the upper limit for T_c . Such high T_c is a common problem to most of computer simulations and caused by too high heating/quenching rates, which exceed the experimental ones by many orders of magnitude [127]. After the MD-quench to 300 K as described above, the chosen structures were heated to elevated temperatures (300 K \rightarrow 1000 K \rightarrow 2000 K \rightarrow 3000 K) and further aged at each temperature for 300,000 time steps corresponding to 0.6 ns.

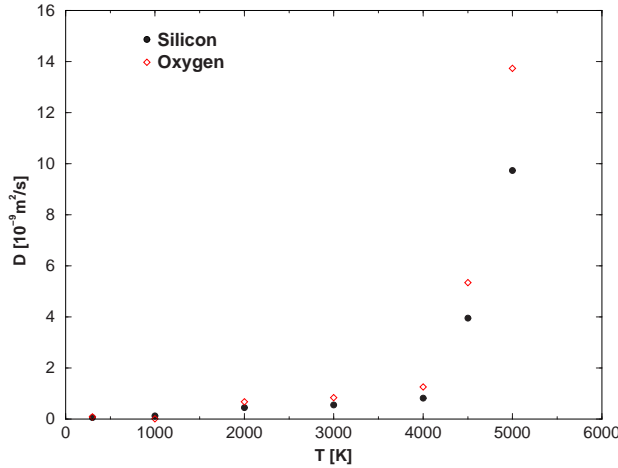


Figure 8.1: Element-specific diffusion constants in zeolite ZSM-5 based partially amorphized material at different temperatures.

To detect relaxations at a given temperature in the course of MD-runs, we monitored the atomic displacements defined as

$$\Delta R(t) = \sqrt{\sum_n [\mathbf{R}_n(t) - \mathbf{R}_n(0)]^2}. \quad (8.4)$$

Here $\mathbf{R}_n(t)$ is the position vector of the particle n at time t , whereas $\mathbf{R}_n(0)$ is the one at the starting or reference configuration on the potential energy surface. If the total displacement of the atoms exceeds a cutoff value and the residence time of the atoms in the new positions also exceeds a minimal period of at least three times the period of

a typical soft vibrational mode, the new positions of the particles were accepted as a starting point for the determination of a possible new minimum configuration. All the stored coordinates were then quenched to $T = 0$ K using a combined SDCG algorithm [132] to locate the nearest minimum configuration in the potential energy surface. In the following section we discuss on the relaxation properties of these minimum structures during aging at the temperatures mentioned above.

8.1 Time Evolution on the Energy Landscape

Figs. 8.2 (a) and (b) show the time evolution of the ensemble averaged potential energies and displacements per atom obtained during the aging of the systems at different temperatures. These averages were taken over ten configurations with a starting average PEC of 60%. In general the potential energy drops during aging. After heating there is a subsequent leveling off of the potential energy at lower temperatures (300K and 1000K). The largest part of the atomic-displacement immediately follows after heating. The average displacements of the atoms is very small, i.e., less than 2% of the Si-O bond distance at 3000 K. The decrease in the average potential energy and displacement per atom increases with temperature as the possibility to cross large energy barriers and to visit farther away minima in potential energy landscape increases.

8.2 Structure and Mode of Relaxations

To study the localization behavior of the relaxations we calculated analogous to our study of the vibrations (chapter 7), the relaxational effective mass and participation ratio. The effective mass of a relaxation is defined as

$$M_{eff} = m_{max} \frac{(\Delta R^0)^2}{|\Delta(\mathbf{R}_{max}^0)^2|}, \quad (8.5)$$

where ΔR^0 represents the distance between two successive minimum configurations as obtained using Eq. (8.4). $|\Delta(\mathbf{R}_{max}^0)^2|$ and m_{max} denote the maximal distance and mass of the farthest jumping atom. The participation ratio is defined as,

$$P_{\Delta R^0} = \frac{(\Delta R^0)^4}{N \sum_n (\mathbf{R}_n^{i,0} - \mathbf{R}_n^{f,0})^4}, \quad (8.6)$$

where $\mathbf{R}_n^{i,0}$ and $\mathbf{R}_n^{f,0}$ denote the initial and the final position of the atom n and N represents the total number of atoms. The participation ratio has the value n/N if n atoms are equally involved in the relaxation process. If all atoms contribute equally in the jump, the resulting participation ratio will be 1.

The influence of the temperature on the jump lengths and the participation ratios are shown in Fig. 8.3. The participation ratios roughly grow linearly with the jump

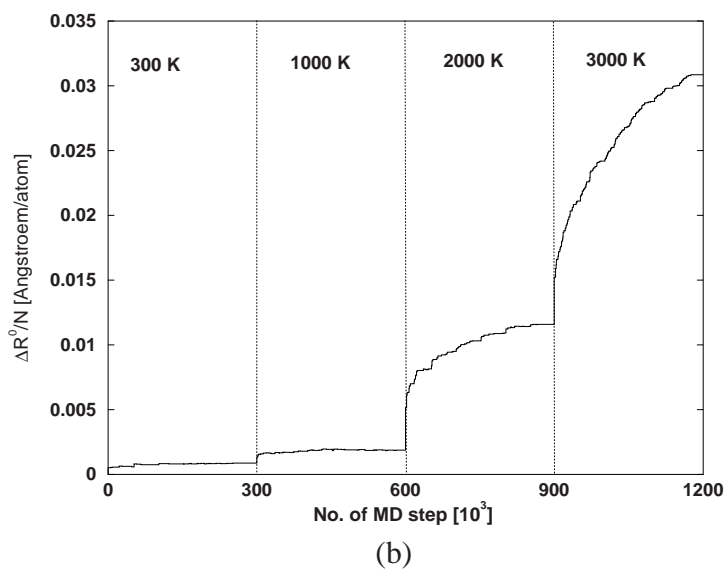
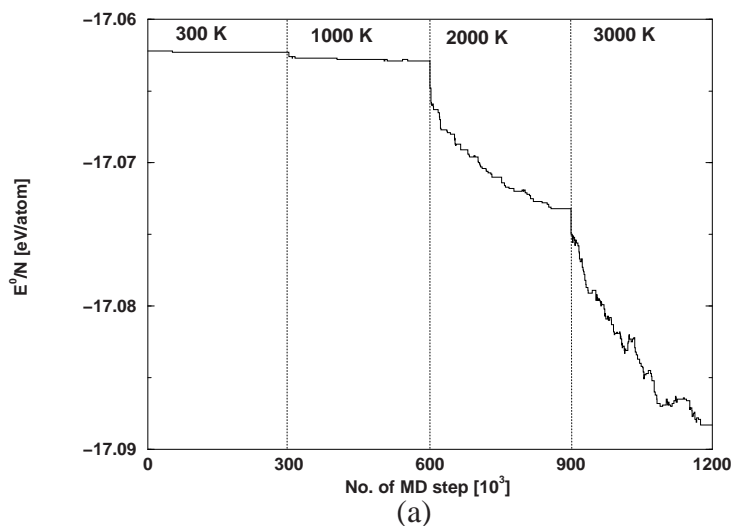


Figure 8.2: (a) Changes in the potential energy per atom and (b) displacement per atom during aging obtained as the ensemble averages. The temperature intervals are indicated by the dotted lines. The heating procedures consisting of 50,000 MD steps between each temperature interval are omitted in the plots.

lengths. The average participation ratios of 0.009, 0.010, 0.018 and 0.036 are observed for jumps at 300 K, 1000 K, 2000 K and 3000 K, respectively. These correspond to the effective masses of 7, 10, 16 and 29 atoms, respectively.

To analyze the relaxation structures we define, a dimensionality of the relaxations and calculate for each jump j the tensor \mathbf{G} ;

$$G_{\alpha\beta}(j) = \frac{\sum_n |\Delta \mathbf{R}_n^0(j)|^\mu (R_{\alpha,n}^0 - R_{\alpha}^{c.m.})(R_{\beta,n}^0 - R_{\beta}^{c.m.})}{\sum_n |\mathbf{R}_n^0(j)|^\mu}, \quad (8.7)$$

where the exponents $\mu = 2$ and $\mu = 4$, correspond to the effective mass and participation ratio, respectively. $\mathbf{R}^{c.m.}$ is the corresponding center of mass coordinate of the relaxation:

$$\mathbf{R}^{c.m.} = \frac{\sum_n |\Delta \mathbf{R}_n^0(j)|^\mu \mathbf{R}_n^0}{\sum_n |\Delta \mathbf{R}_n^0(j)|^\mu}. \quad (8.8)$$

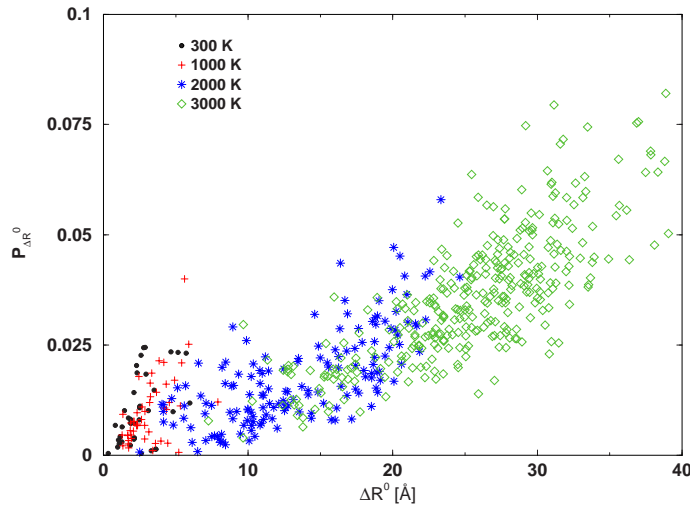


Figure 8.3: Participation ratios of relaxations against jump distance at different temperatures.

Diagonalizing \mathbf{G} we obtain three eigenvalues $\rho^i(j, \mu)$ (for $i = 1, 2, 3$). From these an average radius of gyration is obtained as,

$$R_{gyr}(j, \mu) = \sqrt{\frac{1}{3} \sum_i \rho^i(j, \mu)}. \quad (8.9)$$

If a relaxation is localized on a single atom, $R_{gyr}=0$. For an extended relaxation, it is the root-mean-square distance with the weight determined by μ . A effective dimension of the relaxation can be defined as

$$d(j, \mu) = \sum_i \rho^i(j, \mu) / \max \rho^i(j, \mu). \quad (8.10)$$

Fig. 8.4 and Table 8.1 summarize the results for temperature-dependent dimensionalities and average radii of gyration, averaged over the whole relaxation. We find that at lower temperature the relaxations are of lower dimensionality. At elevated temperatures the average dimensionality as well the average gyration radius increases due to the side-branching of the relaxing chains. The effective mass related values are always higher than the ones related to the participation ratio, reflecting the different weights of the long range displacements.

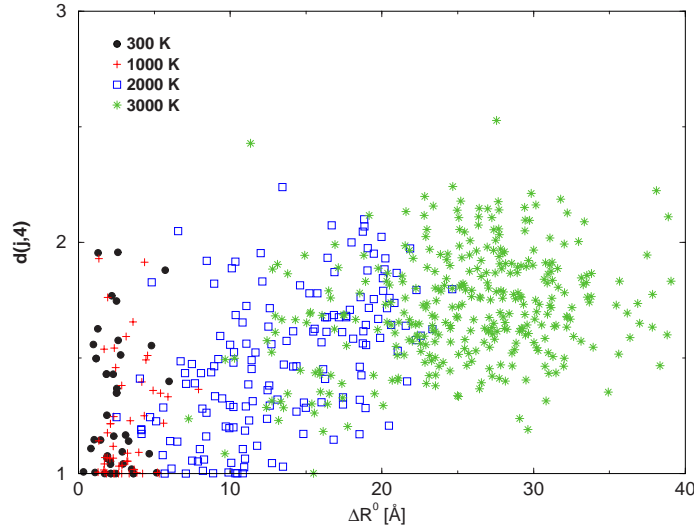


Figure 8.4: The dimensions of the jumps related to the participation ratio at different temperatures.

Table 8.1: The average dimensionalities $\bar{d}(\mu)$ and average radii of gyration $\bar{R}_{gyr}(\mu)$ (in Å) are summarized corresponding to the exponents $\mu = 2$ and $\mu = 4$.

T	$\bar{d}(2)$	$\bar{d}(4)$	$\bar{R}_{gyr}(2)$	$\bar{R}_{gyr}(4)$
300 K	1.34	1.22	6.10	3.88
1000 K	1.51	1.28	8.63	5.46
2000 K	1.55	1.48	11.29	8.69
3000 K	1.72	1.70	13.05	11.36

Table 8.2 summarizes the results of the relaxations with respect to the Si-O bond changes in terms of the increase or the decrease in the coordination number (CN) per jump. The cutoff value of the Si-O bond is 1.8 Å taken from the position of the minimum according to the most intense peak in the total pair-distribution function (for

details refer Fig. 6.2(a)). Another possibility may be that the CN is conserved but the atoms can switch bonds during the relaxation. We denote such changes as bond switch in Table 8.2. At lower temperature (1000 K and below) the relaxations are mainly due to the small changes in the atomic positions and bond breaking occurs only in few cases. At elevated temperatures, bond formations and dissociations occur for 3.38 % of the atoms. The percentage of bond switching processes seems to increase significantly from 0.65% to 2.56% on elevating the temperature from 2000 K to 3000 K.

Table 8.2: Relaxation with respect to bond changes. The numbers represent the percentage of atoms undergoing the mentioned changes per jump.

T	increase in CN	decrease in CN	bond switch
300 K	0.04	0.04	-
1000 K	0.04	0.04	0.01
2000 K	0.24	0.23	0.65
3000 K	0.41	0.41	2.56

Table 8.3: Contributions (in percent) of the relaxations exhibited by Si-O-Si and SiO₄ subunits by the projectional analysis. 'S', 'B' and 'Rot.' represent the stretching, bending and rotational contributions, respectively and the superscripts denote the symmetry of the motions.

T	SiO ₄					Si-O-Si			
	S ^(A₁)	S ^(F₂)	B ^(F₂)	B ^(E)	Rot.	S ^(A₁)	S ^(B₁)	B ^(A₁)	Rot.
300K	1	1	11	10	77	1	0	18	81
1000K	0	0	9	14	77	0	0	17	83
2000K	1	2	11	10	76	1	1	20	78
3000K	1	3	11	9	76	2	1	21	76

In order to study the type of motions involved during the relaxations, we performed the projections of the relaxation vectors onto the symmetry modes of the ideal Si-O-Si (C_{2v} symmetry) and SiO₄ (T_d symmetry) subunits, analogous to the mode analysis for studying the vibrational properties (cf. chapter 7). The calculated contributions of the motion involved in the relaxations exhibited by the subunits are shown in Table 8.3. The respective motions of the oxygen and silicon atoms in the SiO₄ and Si-O-Si subunits mostly stem from rotation followed by bending. The rotational contribution of

the Si-O-Si subunit decreases slightly with increase of the bending contributions with increasing temperature. The contributions from the symmetric and anti-symmetric stretching motions are not so significant. The contributions of Si-O-Si subunits are similar to the modes corresponding to the boson peak region (cf. Table 7.6). However, the bending contributions of the SiO₄ subunits are quite significant for the case of relaxations.

8.3 Correlation between Jumps

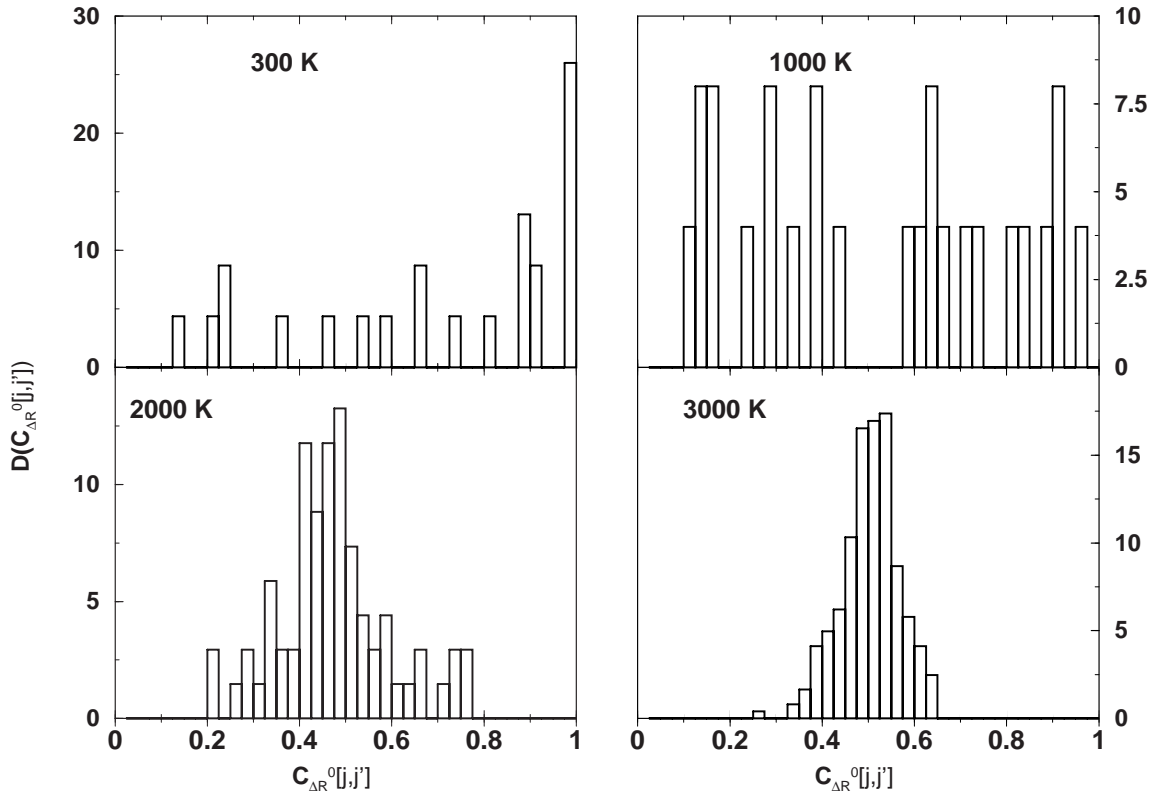


Figure 8.5: The distribution of correlations between the successive jumps at different temperatures.

Looking more closely at the active atoms, the relaxations are found to consist of collective jumps of chains of atoms. These jumps are not uncorrelated events, but successive jumps tend to involve the same atoms. As a quantitative measure, we calculate the correlation between the jumps as

$$c_{\Delta R^0}[j, j'] = \frac{\sum_n \Delta R_n^0[j] \cdot \Delta R_n^0[j']}{\Delta R^0[j] \Delta R^0[j']}, \quad (8.11)$$

where j and j' denotes successive relaxations. For reversible jumps, $c_{\Delta R^0}[j, j']=1$ and for completely uncorrelated jumps one would get values of the order of $1/N$.

Fig. 8.5 shows the observed distributions of all the correlation values averaged over all the relaxations. At low temperatures (300 K and 1000 K) there exists a wide distribution of the correlations. Extremely high-correlated jumps are mainly due to reversible jumps, whereas very low-correlated ones imply that the different parts of the active regions of the system contribute to the relaxations at different times. In contrary at high temperatures (2000 K and 3000 K), the jumps with very high and very low correlations become rare. The former case is due to a strong drop in the potential energy and hence, the possibility of having reversible jumps or highly correlated successive jumps are removed. The latter case is due to the aggregation of different active regions to form large complexes and thus decreasing the possibility of jumps with very low correlations.

8.4 Heterogeneity

In recent years one particular aim of intensive experimental and theoretical studies of relaxations in amorphous solids and liquids was to determine whether the relaxations involve only groups of atoms or they are spread over the whole system [202, 203, 204, 205]. While the first case is related to the heterogeneous scenario, the latter features are homogeneous ones. Various investigations showed that the system becomes homogeneous at high temperatures for sufficiently long times, corresponding to the α relaxation regime [206, 207]. In the intermediate time domain, corresponding to the β relaxation, the heterogeneity becomes more pronounced when the system is cooled down [150].

A detailed picture about the atomic-motions in the relaxations can be obtained by investigating the self part of the van Hove correlation function $G_s(R, t)$, defined as,

$$G_s^\alpha(R, t) = \left\langle \frac{1}{N_\alpha} \sum_{i=1}^{N_\alpha} \delta(R - |\mathbf{R}_i(t) - \mathbf{R}_i(0)|) \right\rangle. \quad (8.12)$$

$\mathbf{R}_i(t)$ is the time-dependent position vector of atom i and $\mathbf{R}_i(0)$ corresponds to the initial configuration. If all the atoms have the same mobility the van Hove correlation function is a Gaussian one. However if atoms are trapped in cages or some are more mobile than the rest, the resulting function will be a non-Gaussian one.

In Fig. 8.6 we show the time-dependent element-specific van Hove correlation functions at 1000 K, 2000 K and 3000 K and at times 0.02 ns, 0.2 ns and 0.6 ns. We observe that with increasing temperature, the atoms move over larger distances as the particles have higher diffusion constants. A striking feature occurs at 2000 K, especially for oxygen, where a formation of distinct peaks in the correlation function has been observed. At still higher temperature (3000 K), these peaks develop into

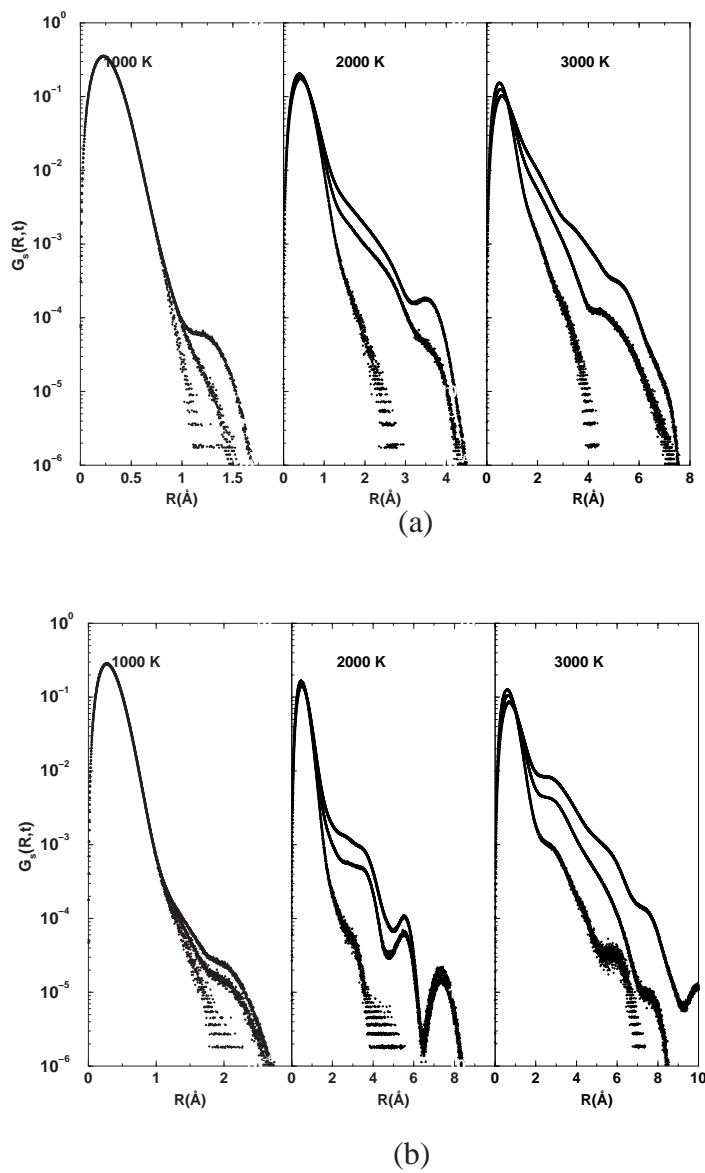


Figure 8.6: Log-linear plots of the van Hove correlation functions of (a) Si and (b) O atoms at different temperatures. The plots are for increasing time of 0.02 ns, 0.2 ns and 0.6 ns in each graph.

weak shoulders. The existence of such peaks are direct evidence of the hopping processes existing in the system that are more prominent for the oxygen atoms. The van Hove correlation functions for the oxygen atoms exhibit a shoulder at 2.6 Å for all the temperatures whose positions correspond to the first peak in the O-O pair-distribution function (refer Fig. 6.2 for details on structural properties). These jumps can be envisaged as defects corresponding to the one-fold or the three-fold coordination. One also observes crowding of graphs at lower temperatures compared to the one observed at 3000 K. These observations lead to the manifestation of the cage effect. At lower temperatures the particles are unable to leave the cage formed by other particles that surround them over the time scale studied in this simulation. However, at higher temperatures (nearing the critical temperature) the particles have sufficient kinetic energy to overcome this cage effect, hence, the motion starts to get more diffusional in nature.

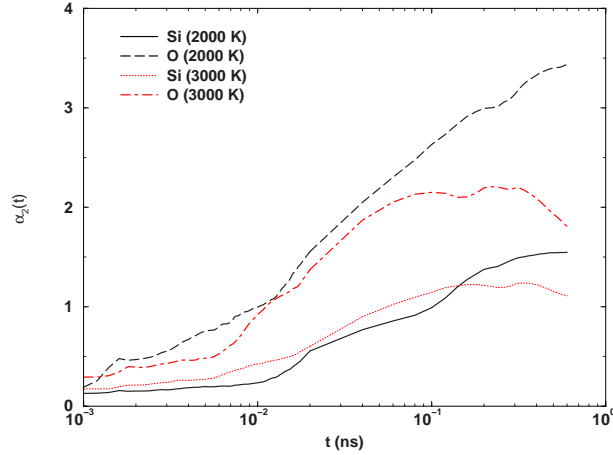


Figure 8.7: Log-linear plot of the non-Gaussianity parameter for Si and O at 2000 K and 3000 K.

The non-Gaussianity parameter (NGP),

$$\alpha_2(t) = (3/5) \langle R^4(t) \rangle / \langle R^2(t) \rangle^2 - 1 \quad (8.13)$$

quantifies the deviation of $G_s(R, t)$ from a Gaussian form. Fig. 8.7 shows, in a log-linear plot the α_2 at 2000 K and 3000 K covering a span of 3 decades. At very short times the NGP is quite small and limiting to zero. In the intermediate time range (0.01 ns - 1.00 ns) the NGP increases with time. The limiting behavior for large times (not shown here) has been studied for various other systems and usually the NGP tends to zero [207, 208, 209]. At both temperatures the oxygen atoms have a higher value of NGP, hence, its a clear evidence that the oxygen atoms probe a more heterogeneous environment than the silicon atoms and can be attributed to smaller mass. For sufficiently long times the non-Gaussianity becomes more pronounced for lower temperature (2000 K) than higher one (3000 K) for both the Si and O atoms. This part of work is documented in Ref. [210].

Chapter 9

Two-Fold Rings in Silicates

Most polymorphs of silicates are formed by corner-sharing of the SiO_4 tetrahedra with differing topology of the networks. However, there also exist structures like stishovite [211] and W-silica [133] containing SiO_6 octahedra and edge-sharing tetrahedra, respectively. The edge-sharing tetrahedral structures in pure silicates are quite rare in nature. Recently, Car-Parrinello MD simulations of a dehydroxylated silica surface showed the presence of edge-sharing tetrahedra [135]. We have also obtained a small percentage of edge-sharing tetrahedra in (partially) amorphous structures obtained by MD (cf. chapter 6).

Considerable interest has been focused on the study of edge-sharing SiO_4 tetrahedra as defective centers in vitreous silica, which act as sites of high chemical reactivity [212, 213, 214, 215]. The occurrence of these edge-sharing units makes structures geometrically constrained and results in an energy penalty. The lack of experimental insight into the stability of these unusual features makes theoretical methods important tools to investigate these strained systems. The knowledge of the energy penalty presently rests on theoretical studies of mainly small clusters using the techniques of quantum chemistry [216, 217, 218] and classical force field models based on quantum chemical reference data [157]. Such calculations neglect the effect of the condensed environment in which the strained part of the system actually resides. Calculations on other solids showed the importance of electron correlation to allow a meaningful comparison of calculated quantities like cohesive energy etc. with experimental data [219, 220]. The most widely used approach is DFT [221, 222, 223]. The attractiveness of this method for practical calculations results mainly from the speed with which the computations can be carried out. Recently, Hamann used DFT based on the generalized gradient approximation (GGA) to extract the strained energies of two- and three- membered rings in models of a SiO_2 network [221]. The calculations gave much smaller strain energies than previously estimated from HF calculations applied to small hydrogen-terminated molecular models [216, 217, 218]. However despite the large success in electronic structure theory DFT has the drawback that the results are highly dependent on the chosen functional and cannot be improved in a systematic

way. As an alternative one can use wave-function based quantum chemical *ab initio* techniques (cf. chapter 5), which are free from these flaws and provide a large array of methods of different accuracy and computational cost. In this approach one can improve the calculation systematically by enlarging the basis set and by including more terms in the expansion of the wavefunction, however at the price of a considerably higher computational cost.

In the following we present HF SCF calculations and subsequent correlation calculations of the energy of edge-sharing tetrahedra and provide a comparison to the usual corner-sharing tetrahedral system. We choose W-silica and α -quartz as the model systems for edge-sharing and corner-sharing silicate systems, respectively. The total and correlation energy per unit cell of W-silica and α -quartz were obtained using a finite cluster and an incremental approach. Various non-metallic polymeric systems have been studied previously using the finite-cluster approach, which yielded accurate results for geometries and energies [219, 224]. The incremental scheme has been used to explore cohesive and geometrical properties of covalent solids [225, 226], semiconductors [227, 220] and ionic solids [228, 229]. Within the incremental approach, starting from HF data obtained with a standard solid state program package as CRYSTAL [118], the necessary correlation corrections to the total energy per unit cell of a periodic system can be obtained as a sum over increments defined in terms of localized orbitals. The correlation energy increments of well localized orbitals may be derived from quantum chemical calculations on finite model systems.

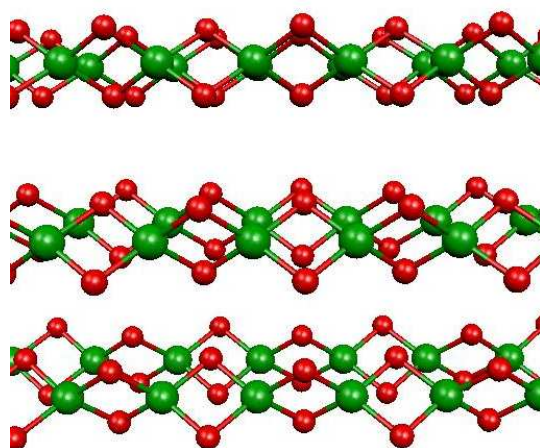


Figure 9.1: Model of W-silica which is characterized by weakly interacting chains of edge-sharing SiO_4 tetrahedral units. Red and green spheres represent O and Si atoms, respectively.

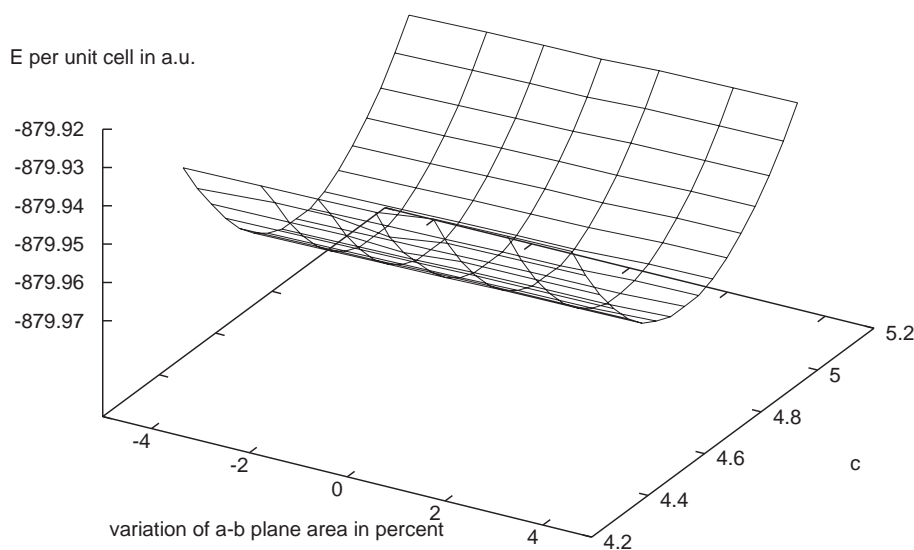


Figure 9.2: Potential energy surface plotted with respect to the variations of the area of a - b plane, where the ratio a/b is constant and the lattice parameter c in Å.

9.1 Applied Methods and Technical Details

W-silica as shown in Fig. 9.1 has a body-centered orthorhombic crystal structure with $Ibam$ space-group, characterized by chains of edge-sharing SiO_4 tetrahedra. Since, these chains are interacting only by weak van der Waals forces, the geometry is mainly determined by the lattice parameter c in the chain direction, i.e., the Si-Si distances. We have carried out series of all-electron calculations using DFT based on the GGA of Perdew and Wang (PW91) [144, 230] varying c over a range 4.2 Å to 5.2 Å. a and b were varied with fixed a/b ratio to change the a - b plane area by $\pm 5\%$. These calculations were performed using a new version of the CRYSTAL code, i.e., CRYSTAL2003, which can optimize the fractional coordinates implicitly [119]. These calculations are analogous to the ones by Hamann [221] where the Si and O ion cores were represented by pseudopotentials. One can see in Fig. 9.2 that the potential energy surface is considerably flatter with respect to a, b variations compared to c variation. This is consistent with the fact that no significant change of energy and ring geometry could be obtained by optimizing the a and b parameter as shown by Hamann [221]. Cal-

culations with and without chain interaction at the minima show only a small energy difference of ≈ 0.005 a.u. Hence one can neglect the weak inter-chain interactions and consider only a single chain for the calculation of geometries and energies.

9.1.1 Finite-Cluster approach/A simple approach

In principle, the total energy E per $[\text{Si}_2\text{O}_4]$ unit cell of a single chain of W-silica may be obtained as the limit

$$E = \lim_{n \rightarrow \infty} \frac{E(\text{Si}_{2n}\text{O}_{4n+2}\text{H}_4)}{n}, \quad (9.1)$$

i.e., by performing calculations for increasingly long oligomers $(\text{OH})_2(\text{Si}_2\text{O}_4)_n\text{H}_2$. In order to reduce the finite-size effects due to the termination of the oligomers by two OH and H groups saturating the dangling bonds of $(\text{Si}_2\text{O}_4)_n$, one may consider instead

$$\begin{aligned} E &= \lim_{n \rightarrow \infty} \Delta E_n \\ &= \lim_{n \rightarrow \infty} [E(\text{Si}_{2n+2}\text{O}_{4n+6}\text{H}_4) - E(\text{Si}_{2n}\text{O}_{4n+2}\text{H}_4)], \end{aligned} \quad (9.2)$$

i.e., the energy change between the subsequent oligomers differing by a single unit cell. Therefore, identical unit cells were used as building blocks for both oligomers, i.e., the geometrical optimization was restricted only to the parameters relevant for the polymer. Eq. (9.2) was used for computing the energy per unit cell employing HF, MP2 and CC levels of theory.

9.1.2 Incremental approach

The simple approach outlined in the previous section relies on the correlated calculations for the whole finite model system, i.e., all the valence electrons have to be correlated at a time. For larger basis sets or more complex systems (as in the case of α -quartz) this approach may become computationally too expensive. Therefore we used an incremental approach based on localized orbitals. One of the prerequisites for the electron correlation treatment within the incremental approach is a reliable HF ground state calculation. We performed such a calculation using the periodic HF code CRYSTAL 98 [118]. Starting from the occupied canonical orbitals of a standard SCF calculation localized bond orbitals are generated using a suitable criterion, e.g., the Foster-Boys localization. The correlation energy per unit cell is expanded as given in Eq. (5.50) in Chapter 5. In order to get reliable results a size-extensive correlation method should be used, although non-size-extensive schemes also may provide a reasonable estimate. We used MP2 and CCSD for this approach for both the systems.

9.2 Structure and Stability of Two-Fold Ring

Calculations on both the systems, i.e., W-silica and α -quartz were performed with 6-31G** basis sets [231, 232]. Usually for polar polymeric systems, calculations using the finite-cluster approach at the HF level may not be applicable due to the long-range of Coulomb interactions. Nevertheless in case of W-silica the finite-cluster approach seems to be accurate enough. For $n = 4$, the HF energy per Si_2O_4 unit is found to be -877.6282 a.u. at the optimized geometry (cf. below). The Bloch-type function based periodic HF code CRYSTAL 98 uses five parameters (ITOL1 to ITOL5) to determine the accuracy of the integral evaluation with respect to the Coulomb and exchange series. For the default combination (6, 6, 6, 6, 12) the HF energy per Si_2O_4 unit is found to be -877.6268 a.u. and for an even tighter threshold (10, 10, 10, 12, 26) a value of -877.6278 a.u. in excellent agreement with the finite-cluster value is obtained. For the HF calculations on the infinite system, using CRYSTAL, the most diffuse *sp* Gaussian exponents of the original basis sets had to be increased due to linear dependency problems. This led to exponents of 0.28 for oxygen (original 0.27) and 0.21 for silicon (original 0.0778). We want to mention that the energy obtained using CRYSTAL, shows a drastic dependence on the *d* Gaussian exponents. For the optimized geometry and the tighter threshold the HF energy per Si_2O_4 unit is found to be -877.6513 a.u. with optimized *d* exponents of 0.48 for oxygen and 0.72 for silicon. However for the correlated calculations and for the comparison with α -quartz, we used the original basis set as a lower value of the total energy per unit cell is obtained.

The correlation energy was calculated by subtracting from the MP2, CCSD and CCSD(T) values the corresponding HF energy/ cell. In this manner we ensured that no spurious contributions to the correlation energy arose due to the use of two different basis sets. The cohesive energies were obtained by subtracting the corresponding energies of the free ground state atoms from the energy per unit cell. These calculations were performed using the MOLPRO molecular orbital *ab initio* program package [139, 140, 233]. The energy per unit cell and the cohesive energy converge rapidly with respect to the cluster size (cf. Fig. 9.3). One finds $\Delta E_4 - \Delta E_3 \approx 10^{-5}$ a.u. (see Eq. (9.2) for definition of ΔE_n). An all-electron CCSD(T) (CCSD with a perturbative contribution of triples) approach could not be used to compute ΔE_4 due to the large system size. The optimized geometry reported in Fig. 9.4(a) and (b) and in Table 9.1 was obtained by performing in turn several total energy calculations for various values of each geometric parameter and fitting the results by a least-squares procedure to polynomials of suitable degrees. The computed lattice parameter *c* of 4.75 Å is in good agreement with the experimental value *e* of 4.72 Å. However, the Si-O bond length of 1.844 Å determined in Ref. [133] appears to be un-physically large. This bond length is even larger than those of three-fold coordinated O in stishovite [234] as was pointed out also in other theoretical studies [216, 221]. Generally, our MP2, CCSD and CCSD(T) structural values agree with those of a previous gradient-corrected DFT study within 0.02 Å and 1°.

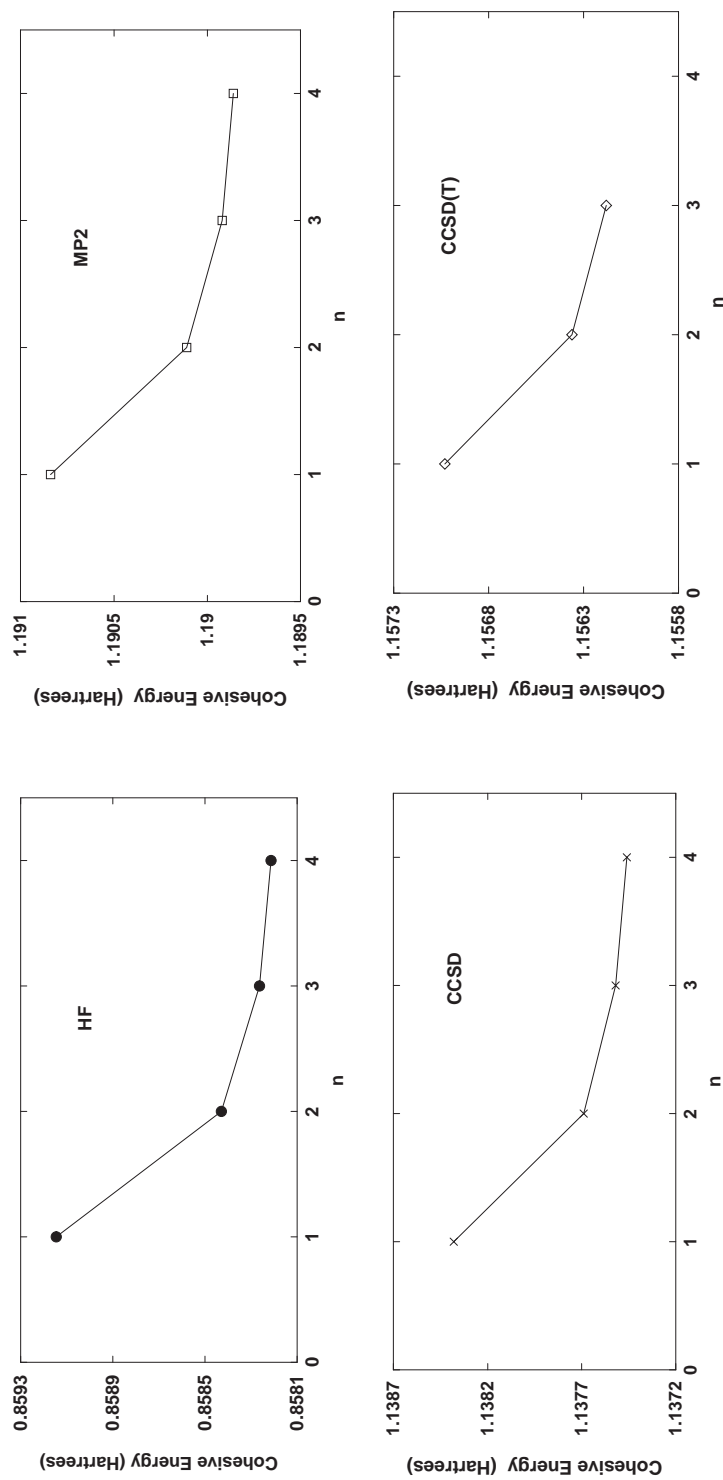


Figure 9.3: Cohesive energy per Si_2O_4 unit of W-silica computed by the finite-cluster approach, plotted as a function of the number unit cells n .

Table 9.1: Geometries of two-membered rings in W-silica.

Method	c (Å)	Si-O (Å)	Si-O-Si (°)	O-Si-O (°)
CRYSTAL SCF	4.680	1.643	90.86	89.13
Finite cluster SCF	4.717	1.650	91.28	88.72
MP2	4.744	1.683	89.62	90.38
CCSD	4.744	1.676	90.09	89.91
CCSD(T)	4.745	1.680	89.81	90.19
GGA ^a	4.757	1.678	90.3	89.7
Expt. ^b	4.720	1.844	79.6	100.4

^a Reference [221].^b Reference [133].

In order to perform a comparison of the stability of W-silica with respect to α -quartz, we performed correlated calculations for both systems on the same footing, i.e., by using the incremental approach truncated at the same level of correlation increments. The experimental geometry [235] was used for α -quartz, whereas the optimized geometry at the CCSD level was used for W-silica (cf. above).

The HF ground state calculations were done using the CRYSTAL code. In order to overcome the convergence problems due to too diffuse exponents and the resulting near-linear dependencies we optimized the exponents of the most diffuse sp Gaussians of a 6-31G** basis set also for α -quartz as performed in Ref. [236]. For O and Si values of 0.28 and 0.21, respectively, were obtained. The exponents of the single d shell of O and Si were optimized to be 0.45 and 0.72 respectively. These d exponents led to a lower total HF energy compared the to the original basis sets.

The exact equation for the infinite system, i.e., Eq. (5.50) in chapter 5 is of little use in practice. However, since electron correlation is a local phenomenon one may derive E_{corr} from a finite model system. Thereby changing the infinite sums in Eq. (5.50) to finite sums up to a maximum order of increments given by the number of bonds n in the finite system. It has been shown by previous calculations that usually there is a rapid convergence of the many-body expansion with respect to the number of atoms included and the integration error decreases with r^{-3} [220, 237]. Therefore, we restricted the expansion of the correlation energy per unit cell to one- and two-body increments, and included the interaction between up to second-nearest neighbor unit cells. The resulting finite clusters as shown in Fig. 9.5 (a) and (b), contain 30 and 57 atoms with dangling bonds saturated by hydrogens for W-silica and α -

quartz, respectively. We performed standard SCF calculations on the clusters in C_1 symmetry and localized the bonds according to the Foster-Boys criterion [115] within the occupied valence space. Following the procedure described above we calculated the correlation energy increments at the MP2 and CCSD level using the MOLPRO molecular orbital *ab initio* program package [139, 140, 233]. Computed increments to the correlation energy are summarized in Table 9.2. It is interesting to note that for α -quartz the two-body increments amount to 69% and 65 % of the correlation energy computed by the MP2 and CCSD methods, respectively.

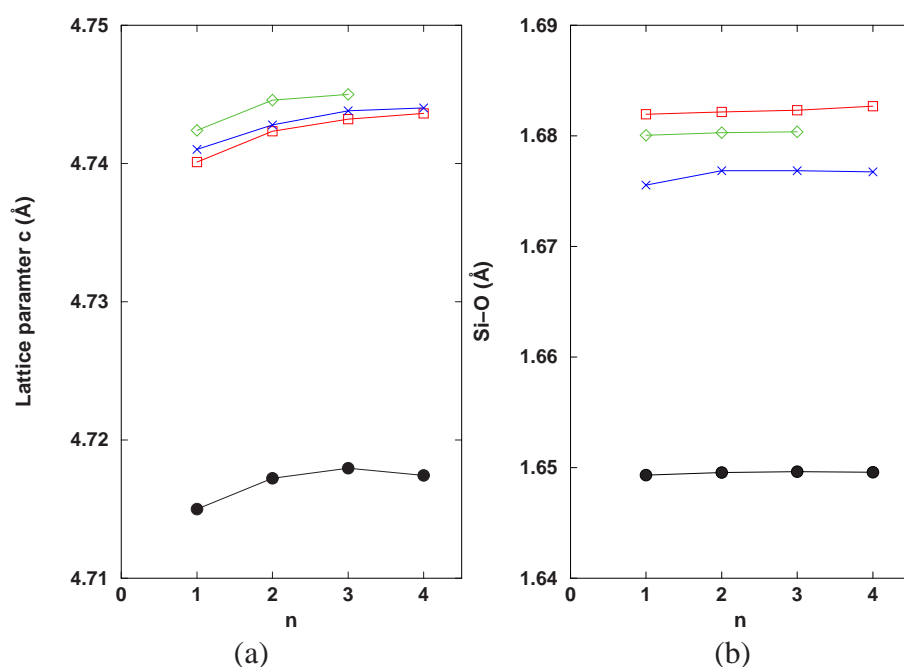
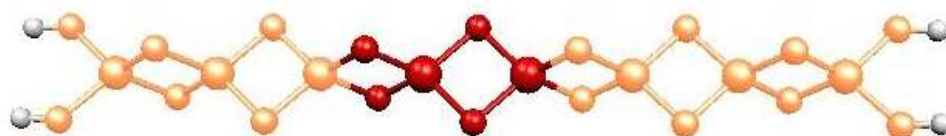
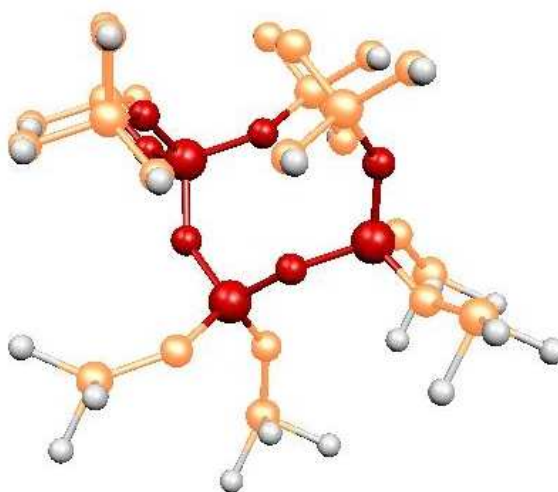


Figure 9.4: (a) Lattice parameter c and (b) Si-O distance of W-silica computed using the finite-cluster approach, plotted as a function of the number unit cells n (filled circles, squares, crosses and diamonds represent HF, MP2, CCSD and CCSD(T) results, respectively).

The correlation contributions to the cohesive energies for α -quartz were obtained as $E_{coh}^{corr} = E_{solid}^{corr} - \sum_i E_{atom,i}^{corr}$ per SiO_2 unit. The results are shown in Table 9.3 for different theoretical methods. For the best method, i.e., CCSD, we obtain 88% of the experimental cohesive energy, which amounts to $\approx 57\%$ of the "experimental" correlation contribution to the cohesive energies (defined as the difference between the experimental cohesive energy and the SCF value). DFT using the local density approximation (LDA) overestimates the cohesive energy by 18%.



(a)



(b)

Figure 9.5: Finite clusters of 30 and 57 atoms of (a) a chain of W-silica and (b) α -quartz, respectively, which are used for the incremental approach. The reference cell is represented by red-colored spheres and the environment by light ones. Here the small-, medium- and large-sized spheres represent H, O and Si atoms, respectively.

Table 9.2: Various increments to the correlation energy per unit cell (in Hartrees) for W-silica and α -quartz. 1NN and 2NN stand for nearest and next-nearest neighbors, respectively.

Correlation treatment	W-silica		α -quartz	
	MP2	CCSD	MP2	CCSD
One-body	-.261366	-.336929	-.327725	-.419682
Two-body (1NN)	-.535584	-.565459	-.692420	-.738037
Two-body (2NN)	-.016056	-.019333	-.037162	-.044587

In Table 9.4 we present the relative energy per Si_2O_4 unit for two-fold rings with respect to α -quartz. Our HF value seems to be much higher compared to the values in References [216,217,222]. These calculations were done on small clusters which lack the strain effect of the environment due to successive edge sharing units. Correlation also seems to play an important role for the stability of these edge-sharing systems. A DFT study using a GGA functional gave a much lower relative energy [221]. In our calculations, by considering MP2 correlation contributions the stability increased by 65%, whereas upon inclusion of CCSD correlation increments the stability increased by 73%. The most sophisticated correlation approach used in our study based on CCSD gave a strain energy of 0.0427 a.u., even less compared to the one of 0.0452 a.u. obtained by a previous DFT calculation [221].

We conclude that edge-sharing SiO_4 tetrahedra in (partially) amorphous SiO_4 systems are possible at a modest energetic expense. This part of work is published in Ref. [239].

Table 9.3: Cohesive energies per SiO_2 unit (in a.u) in α -quartz at different theoretical levels. The percentage of the experimental value is given in parentheses.

HF	HF+MP2	HF+CCSD	LDA ^a	Expt. ^b
.507 (72%)	.598 (85%)	.618 (88%)	.824 (118%)	.706

^a Reference [238].

^b Reference [153].

Table 9.4: Relative energy of a Si_2O_4 unit for various systems with respect to α -quartz (in a.u.).

Method	System	ΔE
HF ^a	W-silica	.156
MP2 ^a	W-silica	.0547
CCSD ^a	W-silica	.0427
GGA ^b	W-silica	.0452
HF ^c	$\text{H}_4\text{Si}_2\text{O}_6$ (C_{2h})	.0849
HF ^d	$\text{H}_4\text{Si}_2\text{O}_6$ (C_{2h})	.0673
HF ^e	$\text{H}_4\text{Si}_2\text{O}_2$ (D_{2h})	>.1058
HF ^f	$\text{H}_{14}\text{Si}_9\text{O}_{25}$.0680

^a This work.

^b Reference [221].

^c Reference [216].

^d Reference [217].

^e Reference [218] [Relative to $\text{H}_8\text{Si}_4\text{O}_4$ (D_{4h})].

^f Reference [222].

Chapter 10

Summary and Outlook

In this thesis we present an investigation of static and dynamic properties of zeolite ZSM-5-based (partially) amorphous materials. The partially amorphized structures were obtained by quenching configurations, which were generated by heating the ZSM-5 crystalline structure using MD. Our simulations gave a detailed account of many significant structural properties at the microscopic level which explain the modified properties and applications of these low crystalline and amorphous materials. The simulations showed that the elementary building blocks are distorted SiO_4 tetrahedra which are mainly connected by corner sharing. A small percentage of edge-shared tetrahedra are also present in the simulated structures. Two-body structural correlation was analyzed by pair-distribution functions and showed the average bond distance between Si and O atoms to be about 1.62 Å. Si-Si and O-O distances correspond to 3.19 Å and 2.61 Å, respectively. Three-body structural correlation was analyzed by bond angle distributions and supports the presence of mainly corner sharing tetrahedra in the network along with a small percentage of edge-sharing ones. The extent of amorphization was quantified by the parameter "percentage of energy crystallinity". Crucial properties like coordination number distribution, effective internal surface area, ring size distribution and effective pore size are found to be a functional of the extent of amorphization. Amorphization leads to a collapse of the framework which reduces for large species the porosity of the system and brings about a closure of large-sized rings and channels. Whereas for larger species the effective internal surface is reduced by this process, it is increased for smaller species, probably due to the increase of the amount of under-coordinated atoms and the generation of smaller rings from larger ones. Hence, it can effect properties like ion exchange and steric effects on reactions. In the amorphous phase 5-fold and 6-folds rings contribute most to the ring distribution followed by 4-fold, 3-fold and 7-fold rings, however, due to irregular ring shape the pores provided by 5-fold and especially 6-fold rings appear to be relatively small.

Vibrational densities of states were calculated by Fourier transformation of the velocity-autocorrelation function and by the diagonalization of the dynamic matrix. The element-specific contributions show that the oxygen atoms participate more signif-

icantly than the silicon atoms, however the contributions of the silicon atoms become quite remarkable for the peak obtained near 24 THz. By means of the eigenmode analysis it was shown that in general both silicon and oxygen atoms exhibit motions which are perpendicular to the Si-O bonds. However oxygen atoms have also significant contributions for their motions parallel to the bonds. The contribution of the individual modes to the specific heat has been analyzed and the plot of C_V/T^3 with respect to T shows a maximum around 15 K.

The vibrational analysis was done in order to get an insight into the nature of vibrational modes, the degree of mode localization and the phase relation. We found that the localized modes are centered in the high-frequency region whereas the quasi-localized states are in the low-frequency region. The phonons in the low-frequency region are mainly acoustic in character whereas those of the high-frequency region are optic-like. Projection of the eigenmodes onto the vibrational symmetric vectors of Si-O-Si and SiO₄ structural subunits suggests that for both structural subunits the asymmetric stretching motions dominantly contribute to the high-frequency region. The symmetric stretching motions of Si-O-Si subunits contribute mostly for the peak at 24 THz in the mid-frequency region and for the peaks between 30 THz and 40 THz in the high-frequency region for the SiO₄ subunits. The rotational and bending motions mainly contribute for the low- and mid-frequency region. Analysis of the dependence of the vibrational DOS with respect to the degree of amorphization reveals that besides an overall smoothening of DOS the high-frequency modes are more drastically affected compared to the low-frequency ones.

Analysis of the low-frequency excitations show that for higher crystallinity the intensity of the boson peak decreases upon amorphization, whereas the opposite behavior is observed for forms with lower crystallinity. The former effect is associated with a decrease of the concentration of 10-fold rings and a general lowering of symmetry by puckering of large rings. The latter behavior is related to an increasing participation of under-coordinated centers in the relevant low-frequency motions. Both observations can be explained in the framework of Maxwell counting of floppy modes. The modes associated with the boson peak for these materials are found to be mainly optic in nature.

The investigation of relaxational properties were restricted to the secondary processes occurring at the temperatures corresponding to 300 K, 1000 K, 2000 K and 3000 K. At higher temperatures (2000 K and 3000 K), the configurations show a sharp drop in the potential energies during aging and reflecting the possibility to visit farther away minima increases. At low temperatures (300 K and 1000 K), the relaxations are mainly due to the small changes in the positions of the atoms. Bond creations and annihilations become significant at higher temperatures (2000 K and 3000 K). The localization of the relaxations was studied using participation ratios and effective masses. We found that participation ratios and jump lengths increase with the increasing temperatures. The structure of the relaxation was quantified by the dimensionality of the jumps. At low temperatures the relaxations consist of chains of atoms that are mainly one dimensional. The dimensionality of the jumps increases with the

temperature due to side-branching of the chains. There exists a wide distribution of correlations between successive jumps at low temperatures. On increasing the temperature we found very high and very low correlated jumps becoming rare. The former fact is due the sharp drop in the potential energy occurring during relaxations making reversible jumps to become rare events. The latter is due to the aggregations of various active regions to form large complexes. Analysis of the heterogeneity in the relaxations occurring in these systems was performed by the van Hove correlation function and the non-Gaussian parameter. The van-Hove correlation function specially for the O atoms exhibits peaks, which are characteristic for the hopping processes. The analysis of non-Gaussianity parameters shows that the oxygen atoms probe a more heterogeneous environment than the silicon atoms and probably attributed to the smaller mass of oxygen atoms. For a longer time scale at low temperature (2000 K) the dynamics becomes more heterogeneous than at the higher one (3000 K). Caging effects are also found to be more prominent at lower temperatures.

We have performed a comparative study on periodic W-silica and α -quartz based on correlated *ab initio* electronic structure calculations. The former compound is considered as a model system for edge-sharing SiO_4 tetrahedra silicates and the latter for corner-sharing ones. Periodic HF theory was used to obtain the mean-field results. The finite-cluster and the incremental approach were used to determine correlation effects in W-silica and α -quartz. For the finite-cluster approach, the geometry as well as the energy per unit cell seem to converge rapidly. Our optimized geometry supports the claim of a previous DFT study that the experimentally available Si-O distance is abnormally large and might be incorrect. For α -quartz we have obtained at the CCSD level around 88% of the experimental cohesive energy using a 6-31G** basis set. The remaining error may be partly due to the lack of higher polarization functions in our one-particle basis set as well as the absence of triple excitations.

Our results and those available from literature predict the strain energy associated with the two-fold rings to depend highly on the chosen model system as well as on the method. Correlation contributions seem to play an important role for the relative stability of the edge-sharing units with respect to corner-sharing ones. HF calculations done solely on the infinite W-silica system gave a strain energy of 0.156 a.u. much higher than the relaxed finite-cluster calculations. Correlation contributions reduce this result by about a factor of three. The most sophisticated method, i.e., CCSD, gave a strain energy of 0.0427 a.u, even slightly lower than the value of 0.0452 a.u. obtained by a previous DFT calculation. We conclude that edge-sharing SiO_4 tetrahedra in (partially) amorphous SiO_4 systems are possible at a modest energetic expense.

Since the success of MD depend on applied potential it will be worth to re-investigate these properties using other potentials. The available potentials for pure silicate systems are that of Vashishta *et al* [165], Oumi *et al* [240], etc. An even deeper insight into catalytic properties of real system can be obtained by using H-ZSM-5 for the simulation. Recently, ZSM-5 based materials with XRD crystallinity levels as low as 2% exhibited superior catalytic performance in skeletal isomerization of linear butenes to iso-butenes [28]. This was ascribed to the decrease in the extend of the alkene inter-

conversion and H-transfer reactions (reduced acidity) occurring as a consequence of decreased zeolitic pore-length. Zeolite ZSM-5 has 12 distinct site for substitution of Si by Al. There exist numerous theoretical studies in order to determine the most favorable position of Al in crystalline ZSM-5 [241, 242, 243]. The model of crystalline H-ZSM-5 can be build from these information. In order to model H-ZSM-5 and its derived system the pair-potential of Kramer *et al* [125] can be used. The method used in this thesis can be used to generate the (partially) amorphous structures corresponding to different extent of amorphization. Further the active site containing Al centers can be cut out with a few layers of environment and the geometry can be allowed to relax within the combined quantum mechanics and molecular mechanics (QM/MM) approach [244, 245]. Brønsted acidities of the active sites can be studied which significantly influence the occurrence of the above mentioned reaction.

Finally, the results presented in this thesis are mainly predictions using theoretical model, it will be dream-coming true to see that these are confirmed by experiments in future.

Bibliography

- [1] S. R. Elliott, *Physics of amorphous materials*, Longman, London (1983).
- [2] A. Feltz, *Amorphous Inorganic Materials and Glasses*, VCH Weinheim (1993).
- [3] H. Salmang, *Die Glasfabrikation*, Springer-Verlag, Berlin (1957).
- [4] J. J. Kitaigorodsky, *Technologie des Glases*, Verlag Technik, Berlin (1959).
- [5] P. T. Sarjeant, R. Roy, *J. Amer. Ceram. Soc.*, **52**, 344 (1969).
- [6] H. Dislich, *J. Non-Cryst. Solids*, **57**, 371 (1983).
- [7] R. C. Haushalter, C. M. O'Connor, J. P. Haushalter, A. M. Umarji, G. K. Shenoy, *Angew. Chem.*, **96**, 147 (1984).
- [8] J. Tauc, A. Abraham, R. Zallen, M. Slade, *J. Non-Cryst. Solids*, **4**, 279 (1970).
- [9] A. Feltz, C. Kaps, *Thin Solid Films*, **70**, 117 (1980).
- [10] P. R. Stuart, *Vacuum*, **19**, 507 (1969).
- [11] F. K. McTaggart, *Plasma Chemistry in Electrical Discharges*, Elsevier, New York (1967).
- [12] R. H. Doremus, *Proc. 11th Int. Congr. Glass Prague*, **1**, 263 (1977).
- [13] R. Schrader, W. Dusdorf, *Kristall und Technik*, **1**, 59 (1966).
- [14] P. S. De Carli, J. C. Jamieson, *J. Chem. Phys.*, **31**, 1657 (1959).
- [15] W. Primak, *Phys. Rev.*, **110**, 1240 (1958).
- [16] A. F. Cronstedt, *Akad. Handl. Stockholm*, **18**, 120 (1756).
- [17] R. M. Barrer, *Proc. Roy. Soc.* (1938).
- [18] R. M. Barrer, P. J. Denny, *J. Chem. Soc.*, 971 (1961).

- [19] C. Kosanovic, A. Cizmek, B. Subotic, I. Smit, M. Stubicar, A. Tonejc, *Zeolites*, **15**, 51 (1995).
- [20] C. Kosanovic, B. Subotic, *Microporous Mater.*, **12**, 261 (1997).
- [21] R. A. Secco, Y. Huang, *J. Phys. Chem. Solids*, **60**, 999 (1999)
- [22] C. Kosanovic, B. Subotic, I. Smit, *Thermochim. Acta*, **317**, 25 (1998).
- [23] S. X. Wang, L. M. Wang, R. C. Ewing, *J. Nucl. Mater.*, **278**, 233 (2000).
- [24] B. X. Gu, L. M. Wang, R. C. Ewing, *J. Nucl. Mater.*, **278**, 64 (2000).
- [25] C. P. Nicolaidis, N. P. Sincadu, M. S. Scurrrell, *Catal. Today*, **17**, 429 (2002).
- [26] P. B. Venuto, *Microporous Mater.*, **2**, 297 (1994).
- [27] G. H. Hutchings, C. P. Nicolaidis, M. S. Scurrrell, *Catal. Today*, **15**, 23 (1992).
- [28] C. P. Nicolaidis, *Appl. Catal. A*, **185**, 211 (1999).
- [29] M. S. Scurrrell, *Appl. Catal.*, **41** 89 (1988).
- [30] D. Seddon, *Catal. Today*, **6**, 351 (1990).
- [31] J. A. Biscardi, E. Iglesia, *J. Catal.*, **182**, 117 (1999).
- [32] J. C. Tully, *Classical and Quantum Dynamics in Condensed Phase Simulations*, edited by B. J. Berne, G. Cicotti and D. F. Coker, World Scientific, Singapore (1998).
- [33] J. C. Tully, *Faraday Discuss.*, **110**, 407 (1998).
- [34] J. C. Burant, J. C. Tully, *J. Chem. Phys.*, **112**, 6097 (2000).
- [35] A. Messiah, *Quantum Mechanics*, North-Holland Publishing Company, Amsterdam (1964).
- [36] H. Goldstein, *Classical Mechanics*, Aula-Verlag, Wiesbaden (1987).
- [37] G. C. Schatz, *Rev. Mod. Phys.*, **61**, 669 (1989).
- [38] J. C. Greer, R. Ahlrichs and I. V. Hertel, *Z. Phys. D*, **18**, 413 (1991).
- [39] M. P. Allen, D. J. Tildesly, *Computer Simulation of Liquids*, Clarendon Press, Oxford (1990).
- [40] C. G. Gray, K. E. Gubbins, *Theory of Molecular Fluids Vol. 1*, Clarendon Press, Oxford (1984).

- [41] D. Marx, J. Hutter, *Modern Methods and Algorithms of Quantum Chemistry*, NIC Series, Vol. 1 (2000).
- [42] M. E. Tuckerman, *Quantum Simulations of Complex Many-Body Systems: From Theory to Algorithms*, NIC Series, Vol. 10 (2002).
- [43] M. Griebel, S. Knapek, G. Zumbusch, A. Caglar, *Numerische Simulation in der Moleküldynamik*, Springer-Verlag Berlin, Heidelberg (2004).
- [44] D. C. Rapaport, *The Art of Molecular Dynamics Simulation*, Cambridge University Press, Cambridge (1995).
- [45] J. M. Haile, *Molecular Dynamics Simulation*, Wiley (1992).
- [46] A. R. Leach, *Molecular Modelling: Principles and Application*, Pearson Education Limited, (2001).
- [47] D. Frenkel, B. Smit, *Understanding Molecular Simulation: From Algorithms to Applications*, Academic Press, California (2002).
- [48] W. Cui, F. Li, N. L. Allinger, *J. Amer. Chem. Soc.*, **115**, 2943 (1993).
- [49] N. Nevins, J. H. Lii, N. L. Allinger, *J. Comp. Chem.*, **17**, 695 (1996).
- [50] S. L. Mayo, B. D. Olafson, W. A. Goddard, *J. Phys. Chem.*, **94**, 8897 (1990).
- [51] M. J. Bearpark, M. A. Robb, F. Bernardi, M. Olivucci, *Chem. Phys. Lett.*, **217**, 513 (1994).
- [52] T. Cleveland, C. R. Landis, *J. Amer. Chem. Soc.*, **118**, 6020 (1996).
- [53] A. K. Rappé, C. J. Casewit, K. S. Colwell, W. A. Goddard, W. M. Skiff, *J. Amer. Chem. Soc.*, **114**, 10024 (1992).
- [54] Z. W. Peng, C. S. Ewig, M. -J. Hwang, M. Waldmann, A. T. Hagler, *J. Phys. Chem.*, **101**, 7243 (1997).
- [55] W. D. Cornell, P. Cieplak, C. I. Bayly, I. R. Gould, K. M. Merz, D. M. Ferguson, D. C. Spellmeyer, T. Fox, J. W. Caldwell, P. A. Kollman, *J. Amer. Chem. Soc.*, **117**, 5179 (1995).
- [56] A. D. Mackerell, J. Wiorkiewicz-Kuczera, M. Karplus, *J. Amer. Chem. Soc.*, **117**, 11946 (1995).
- [57] W. L. Jorgensen, D. S. Maxwell, J. Tiradorives, *J. Amer. Chem. Soc.*, **118**, 11225 (1996).
- [58] T. A. Halgren, *J. Comp. Chem.*, **17**, 490 (1996).

- [59] J. J. Nicolas, K. E. Gubbins, W. B. Streett, D. J. Tildesly, *Mol. Phys.*, **37**, 1429 (1979).
- [60] P. Ewald, *Ann. Phys.*, **64**, 253 (1921).
- [61] S. W. de Leeuw, J. W. Perram, E. R. Smith, *Proc. R. Soc. London*, A373, 27(1980).
- [62] S. W. de Leeuw, J. W. Perram, E. R. Smith, *Proc. R. Soc. London*, A373,57 (1980).
- [63] P. Gibbon, G. Sutmann, *Quantum Simulations of Complex Many-Body Systems: From Theory to Algorithms*, NIC Series, Vol. 10 (2002).
- [64] D. M. Heyes, *J. Chem. Phys.*, **74**, 1924 (1981).
- [65] J. W. Perram, H. G. Petersen, S. W. de Leeuw, *Mol. Phys.*, **65**, 875 (1988).
- [66] D. J. Evans, W. G. Hoover, B. H. Failor, B. Moran and A. J. C. Ladd, *Phys. Rev. A*, **28**, 1016 (1983).
- [67] H. C. Andersen, *J. Chem. Phys.*, **72**, 2384, (1980).
- [68] S. Nosé, *J. Chem. Phys.*, **81**, 511, (1984).
- [69] M. Parrinello, A. Rahman, *Phys. Rev. Lett.*, **45**, 1196, (1980).
- [70] M. Parrinello, A. Rahman, *J. Appl. Phys.*, **52**, 7182, (1981).
- [71] M. Parrinello, A. Rahman, *J. Chem. Phys.*, **76**, 2662, (1982).
- [72] C. A. Floudas, P. M. Pardalos, *Recent Advances in Global Optimization*, Princeton University Press, Princeton, NJ (1991).
- [73] A. R. Leach, *Reviews in Computational Chemistry Vol-2*, VCH publishers, New York (1991).
- [74] L. Piel, J. Kostrowicki, H. A. Scheraga, *J. Phys. Chem.*, **93**, 3339, (1989).
- [75] E. O. Purisima, H. A. Scheraga, *Proc. Natl. Acad. Sci., USA*, **83**, 2782, (1986).
- [76] E. Aarts, J. Korst *Simulated Annealing and Boltzmann Machines*, Wiley-Interscience Series in Discrete Mathematics and Optimization, John Wiley & Sons, Tiptree, Essex (1990).
- [77] S. Kirkpatrick, C. D. Gelatt, M. P. Vecchi, *Science*, **220**, 671 (1983).
- [78] N. Metropolis, A. W. Rosenbluth, A. H. Teller, E. Teller, *J. Chem. Phys.*, **21**, 1087, (1953).

- [79] I. O. Bohachevsky, M. E. Johnson, M. L. Stein, *Technometrics*, **28**, 209, (1986).
- [80] M. Hao, W. K. Olson, *Macromolecules*, **22**, 3292 (1989).
- [81] T. Schlick, *Reviews in Computational Chemistry Vol-3*, VCH publishers, New York (1992).
- [82] J. R. Shewchuck, *An introduction to the conjugate gradient method without agonizing pain*, Tech. Rep. CMU-CS-94-125, Carnegie Mellon University (1994).
- [83] T. Hjorteland, *The action variational principle in cosmology*, PhD thesis, University of Oslo, Oslo (1999).
- [84] F. Jensen, *Introduction to computational chemistry*, John Wiley & Sons, Chichester, England (1999).
- [85] M. J. D. Powell, *The Computer Journal*, **7**, 155 (1964).
- [86] Y. Waseda, *The Structure of Non-Crystalline Materials*, McGraw-Hill Inc., New York (1980).
- [87] C. Kittel, *Introduction to Solid State Physics*, Seventh Edition, John Wiley & Sons, New York (1996).
- [88] N. W. Ashcroft, N. D. Mermin, *Solid State Physics*, Saunders College, Philadelphia (1976).
- [89] H. R. Schober, W. Petry, *Material Science and Technology*, edited by R. W. Cahn, P. Haasen, E. J. Kramer, Vol-1, VCH, Weinheim (1991).
- [90] W. A. Phillips, *Amorphous Solids, Low-Temperature Properties*, Topics in Current Physics Vol-3, Springer-Verlag, Berlin (1981).
- [91] P. W. Anderson, B. I. Halperin, A. M. Varma, *Philos. Mag.*, **25**, 1 (1972).
- [92] W. A. Phillips, *Low Temp. Phys.*, **7**, 351 (1972).
- [93] U. Buchenau, M. Prager, N. Nucker, A. J. Dianoux, N. Ahmed, W. A. Phillips, *Phys. Rev. B*, **34**, 5665 (1986).
- [94] V. G. Karpov, M. I. Klinger, F. N. Ignat'ev, *Sov. Phys.-JETP*, **57**, 439 (1983).
- [95] U. Buchenau, Y. M. Galperin, V. L. Gurevich, D. A. Parshin, M. A. Ramos, H. R. Schober, *Phys. Rev. B*, **46**, 2798 (1992).
- [96] H. R. Schober, C. Oligschleger, *Nukleonika*, **39**, No. 1-2, 185 (1994).
- [97] U. Buchenau, Y. M. Galperin, V. L. Gurevich, H. R. Schober, *Phys. Rev. B*, **43**, 5039 (1991).

- [98] H. R. Schober, B. B. Laird, *Phys. Rev. B*, **44**, 6746 (1991).
- [99] A. Szabo, N. S. Ostlund, *Modern Quantum Chemistry*, Dover Publications, New York (1996).
- [100] I. N. Levine, *Quantum Chemistry*, Prentice hall, NJ (2000).
- [101] P. Knowles, M. Sch"utz, H.-J. Werner, *Modern Methods and Algorithms of Quantum Chemistry*, NIC Series, Vol. 1 (2000).
- [102] C. Møller, M. S. Plesset, *Phys. Rev.*, **46**, 618 (1934).
- [103] T. D. Crawford, H. F. Schaefer III, *Reviews in Computational Chemistry Vol-14*, VCH publishers, New York (2000).
- [104] G. D. Purvis III, R. J. Bartlett, *J. Chem. Phys.*, **76**, 1910 (1982).
- [105] G. E. Scuseria, C. L. Janssen, H. F. Schaefer III, *J. Chem. Phys.*, **89**, 7382 (1988).
- [106] K. Raghavachari, G. W. Trucks, J. A. Pople, M. Head-Gordon, *Chem. Phys. Lett.*, **157**, 479 (1989).
- [107] R. G. Parr, W. Yang, *Density-Functional Theory of Atoms and Molecules*, Oxford University Press, NY (1989).
- [108] P. Hohenberg, W. Kohn, *Phys. Rev.*, **136**, B864 (1964).
- [109] W. Kohn, L. J. Sham, *Phys. Rev.*, **140**, A1133 (1965).
- [110] P. Fulde, *Electron Correlations in Molecules and Solids*, Springer Series in Solid State Science, Springer-Verlag, Berlin (1995).
- [111] C. Pisani, *Quantum-Mechanical Ab-initio Calculation of the Properties of Crystalline Materials*, Lecture Notes in Chemistry Vol. 67, Springer-Verlag, Berlin (1996).
- [112] C. Edmiston, K. Ruedenberg, *Rev. Mod. Phys.*, **35**, 457 (1963).
- [113] C. Edmiston, K. Ruedenberg, *J. Chem. Phys.*, **43**, S97 (1965).
- [114] S. F. Boys, *Rev. Mod. Phys.*, **32**, 296 (1960).
- [115] J. M. Foster, S. F. Boys, *Rev. Mod. Phys.*, **32**, 300 (1960).
- [116] W. von Niessen, *J. Chem. Phys.*, **56**, 4290 (1972).
- [117] J. Pipek, P. G. Mezey, *J. Chem. Phys.*, **90**, 4916 (1989).

- [118] V. R. Saunders, R. Dovesi, C. Roetti, M. Causá, N. M. Harrison, R. Orlando, C. M. Zicovich-Wilson, *CRYSTAL98 User's Manual*, University of Torino, Torino (1998).
- [119] V. R. Saunders, R. Dovesi, C. Roetti, R. Orlando, C. M. Zicovich-Wilson, N. M. Harrison, K. Doll, B. Civalleri, I. Bush, *CRYSTAL2003 User's Manual*, University of Torino, Torino (2003).
- [120] R. Dovesi, R. Orlando, C. Roetti, C. Pisani, V. R. Saunders, *Phys. Stat. Sol. (b)*, **217**, 63 (2000).
- [121] A. Shukla, M. Dolg, H. Stoll, P. Fulde, *Chem. Phys. Lett.*, **262**, 213 (1996).
- [122] A. B. Mukhopadhyay (unpublished).
- [123] C. Oligschleger, B. Laird (unpublished).
- [124] G. J. Kramer, N. P. Farragher, B. W. H. van Beest, R. A. van Santen, *Phys. Rev. B.*, **43**, 5068 (1991).
- [125] G. J. Kramer, A. J. M de Man, R. A. van Santen, *J. Am. Chem. Soc.*, **113**, 6435 (1991).
- [126] K. Vollmayr, *Ph.D Thesis*, University of Mainz (1995).
- [127] K. Vollmayr, W. Kob, K. Binder, *Phys. Rev. B*, **54**, 15808 (1996).
- [128] D. H. Olson, G. T. Kokotailo, S. L. Lawton, W. M. Meier, *J. Phys. Chem.*, **85**, 2238 (1981).
- [129] S. L. Meisel, J. P. McCullough, C. H. Lechthaler, P. B. Weisz, *Chem. Technol.*, **6**, 86 (1976).
- [130] C. D. Chang, A. J. Silvestri, *J. Catal.*, **47**, 249 (1977).
- [131] K. Vollmayr, W. Kob, K. Binder, *J. Chem. Phys.*, **105**, 4714 (1996).
- [132] R. Fletcher, C. M. Reeves, *Comput. J.*, **7**, 149 (1964).
- [133] V. A. Weiss, A. Weiss, *Z. Anorg. Allg. Chem.*, **276**, 95 (1954).
- [134] P. B. Moore, *Amer. Mineral.*, **55**, 1146 (1970).
- [135] D. Ceresoli, M. Bernasconi, S. Iarlori, M. Parrinello, E. Tosatti, *Phys. Rev. Lett.*, **84**, 3887 (2000).
- [136] J. A. Tossell, G. V. Gibbs, *Amer. Mineral.*, **61**, 287 (1976).
- [137] J. A. Tossell, G. V. Gibbs, *J. Mol. Struc.*, **35**, 273 (1976).

- [138] R. Ahlrichs, M. Bär, M. Häser, H. Horn, C. Kölmel, *Chem. Phys. Lett.*, **162**, 165 (1989).
- [139] H.-J. Werner, P. J. Knowles with contributions from R.D. Amos, A. Berning, D.L. Cooper, M.J.O. Deegan, A.J. Dobbyn, F. Eckert, C. Hampel, G. Hetzer, T. Leininger, R. Lindh, A.W. Lloyd, W. Meyer, M.E. Mura, A. Nicklass, P. Palmieri, K. Peterson, R. Pitzer, P. Pulay, G. Rauhut, M. Sch"utz, H. Stoll, A.J. Stone, and T. Thorsteinsson, *MOLPRO ab initio electronic structure package, version 2000.1* (2000).
- [140] C. Hampel, K. Peterson, H.-J. Werner, *Chem. Phys. Lett.*, **190**, 1 (1992).
- [141] F. L. Galeener, G. Lucovsky, *Phys. Rev. Lett.*, **37**, 1474 (1976).
- [142] A. Pasquarello, R. Car, *Phys. Rev. Lett.*, **80**, 5145 (1998).
- [143] A. D. Becke, *J. Chem. Phys.*, **98**, 5648 (1993).
- [144] A. D. Becke, *Phys. Rev. A*, **38**, 3098 (1988).
- [145] J. P. Perdew, *Phys. Rev. B*, **33**, 8822 (1986).
- [146] T. H. Dunning, *J. Chem. Phys.*, **90**, 1007 (1989).
- [147] D. E. Woon and T. H. Dunning, *J. Chem. Phys.*, **98**, 1358 (1993).
- [148] C. P. Nicolaides, H. H. Kung, N. P. Makgoba, N. P. Sincadu, M. S. Scurrall, *Appl. Catal. A*, **223**, 29 (2002).
- [149] C. Oligschleger, *Phys. Rev. B*, **60**, 3182 (1999).
- [150] J. Horbach, W. Kob, *Phys. Rev. B*, **60**, 3169 (1999).
- [151] B. P. Feuston, S. H. Garofalini, *J. Chem. Phys.*, **89**, 5818 (1988).
- [152] Cerius² modeling software, <http://www.msi.com/cerius2>, Accelrys Inc., San Diego, CA (2001).
- [153] R. C. Weast, *CRC Handbook of Chemistry and Physics*, CRC Press, Cleveland, OH (2000).
- [154] E. C. Moloy, L. P. Davila, J. F. Shackelford, A. Navrotsky, *Micro. Meso. Mater.*, **54**, 1 (2002).
- [155] J. Xie, S. Kaliaguine, *Appl. Catal. A*, **148**, 415 (1997).
- [156] T. F. Soules, *J. Chem. Phys.*, **71**, 4570 (1979).
- [157] F. L. Galeener, *J. Non-Cryst. Sol.*, **49**, 53 (1982).

- [158] A. Saito, H. C. Foley, *Microporous Mater.*, **3**, 543 (1995).
- [159] A. B. Mukhopadhyay, C. Oligschleger, M. Dolg, *Phys. Rev. B*, **67**, 14106 (2003).
- [160] P. A. Jacobs, H. K. Bayer, J. Valyon, *Zeolites*, **1**, 161 (1981).
- [161] W. Jin, P. Vashishta, R. K. Kalia, J. P. Rino, *Phys. Rev. B*, **48**, 9359 (1993).
- [162] C. Oligschleger, J. C. Schön, *J. Phy.: Condens. Matter*, **9**, 1049 (1997).
- [163] W. Voigt, *Ann. Phys., Lpz.*, **33**, 573 (1889).
- [164] D. Beeman, R. Alben., *Adv. Phys.*, **26**, 339 (1977).
- [165] P. Vashishta, R. K. Kalia, J. P. Rino, *Phys. Rev. B*, **41**, 12197 (1990).
- [166] S. N. Taraskin, S. R. Elliott, *Phys. Rev. B*, **56**, 8605 (1997).
- [167] C. Oligschleger, H. R. Schober, *Phys. Rev. B*, **59**, 811 (1999).
- [168] B. B. Laird, H. R. Schober, *Phys. Rev. Lett.*, **66**, 636 (1991).
- [169] R. J. Bell, P. Dean, *Philos. Mag.*, **25**, 1381 (1972).
- [170] H. R. Schober, C. Oligschleger, *Phys. Rev. B*, **53**, 11469 (1996).
- [171] A. A. Maradudin, E. W. Montroll, G. H. Weiss, I. P. Ipatova, *Theory of Lattice Dynamics in the Harmonic Approximation, Solid State Physics Suppl.3*, Academic, New York (1971).
- [172] H. Jobic, K. S. Smirnov, D. Bougeard, *Chem. Phys. Lett.*, **344**, 147 (2001).
- [173] V. A. Ermoshin, K. S. Smirnov, D. Bougeard, *Chem. Phys.*, **202**, 53 (1996).
- [174] E. Courtens, M. Foret, B. Hehlen, R. Vacher, *Solid State Commun.*, **117**, 187 (2001).
- [175] S. N. Taraskin, S. R. Elliott, *Phys. Rev. B*, **59**, 8572 (1999).
- [176] J. C. Maxwell, *Phil. Mag.*, **27**, 294 (1864).
- [177] M. F. Thorpe, *J. Non-Crys. Solids*, **57**, 355 (1983).
- [178] M. T. Dove, M. J. Harris, A. C. Hannon, J. M. Parker, I. P. Swainson, M. Gambhir, *Phys. Rev. Lett.*, **78**, 1070 (1997).
- [179] K. D. Hammonds, V. Heine, M. T. Dove, *J. Phys. Chem. B*, **102**, 1759 (1998).
- [180] K. D. Hammonds, H. Deng, V. Heine, M. T. Dove, *Phys. Rev. Lett.*, **78**, 3701 (1997).

- [181] S. N. Taraskin, S. R. Elliot, *Europhys. Lett.*, **39**, 37 (1997).
- [182] M. Nakamura, M. Arai, Y. Inamura, T. Otomo, S. M. Bennington, *Phys. Rev. B*, **66**, 24203 (2002).
- [183] J. Boerio-Goates, R. Stevens, B. Lang, B. F. Woodfield, *J. Thermal Analysis and Calorimetry*, **69**, 773 (2002).
- [184] F. Finkemeier, W. von Niessen, *Phys. Rev. B*, **63**, 235204 (2001).
- [185] F. Finkemeier, W. von Niessen, *Phys. Rev. B*, **66**, 87202 (2002).
- [186] G. Carini, G. D'Angelo, G. Tripodo, A. Fontana, A. Leonardi, G. A. Saunders, A. Brodin, *Phys. Rev. B*, **52**, 9342 (1995).
- [187] A. B. Mukhopadhyay, C. Oligschleger, M. Dolg, *Phys. Rev. B*, **68**, 24205 (2003)
- [188] A. B. Mukhopadhyay, C. Oligschleger, M. Dolg, *Phys. Rev. B*, **69**, 12202 (2004).
- [189] B. Frick, D. Richter, *Science*, **267**, (1995)
- [190] W. W. Scott, R. K. MacCrone, *Phys. Rev. B*, **1**, 3515 (1970).
- [191] U. Buchenau, H. M. Zhou, N. Nucker, K. S. Gilroy, W. A. Phillips, *Phys. Rev. Lett.*, **60**, 1318. (1988).
- [192] U. Buchenau, *J. Phys.: Condens. Matter*, **13**, 7827 (2001).
- [193] K. A. Topp, D. G. Cahill, *Z. Phys. B*, **101**, 235 (1996).
- [194] H. A. Kramers, *Physica*, **7**, 284 (1940).
- [195] M. Goldstein, *J. Chem. Phys.*, **51**, 3728 (1969).
- [196] F. H. Stillinger, T. A. Weber, *Phys. Rev. A*, **28**, 2408 (1983).
- [197] R. Malek, N. Mousseau, *Phys. Rev. E*, **62**, 7723 (2000).
- [198] S. Büchner, A. Heuer, *Phys. Rev. E*, **60**, 6507 (1999).
- [199] A. Heuer, R. J. Silbey, *Phys. Rev. Lett.*, **70**, 3911 (1993).
- [200] R. Böhmer, K. L. Ngai, C. A. Angell, D. J. Plazek, *J. Chem. Phys.*, **99**, 4201 (1993).
- [201] M. D. Ediger, C. A. Angell, S. R. Nagel, *J. Phys. Chem.*, **100**, 13200 (1996).
- [202] D. Caprion, J. Matsui, H. R. Schober, *Phys. Rev. Lett.*, **85**, 4293 (2000).
- [203] R. Zorn, *J. Phys.: Condens. Matter*, **15**, R1025 (2003).

- [204] R. Richert, *J. Phys.: Condens. Matter*, **14**, R703 (2002).
- [205] A. Heuer, H. W. Spiess, *Phys. Rev. Lett.*, **82**, 1335 (1999).
- [206] A. Arbe, J. Colmenero, M. Monkenbusch, D. Richert, *Phys. Rev. Lett.*, **81**, 590 (1998).
- [207] D. Caprion, H. R. Schober, *Phys. Rev. B*, **62**, 3709 (2000).
- [208] W. Kob, H. C. Andersen, *Phys. Rev. E*, **51**, 4626 (1995).
- [209] K. L. Ngai, J. Habasaki, Y. Hiwatari, C. León, *J. Phys.: Condens. Matter*, **15**, S1607 (2003).
- [210] A. B. Mukhopadhyay, C. Oligschleger, M. Dolg, Manuscript Submitted.
- [211] S. M. Stishov, S. V. Popova, *Geochem.*, **10**, 923 (1961).
- [212] J. C. Mikkelsen, F. L. Galeener, *J. Non-Crys. Solids*, **37**, 71 (1980).
- [213] C. M. Chiang, B. R. Zegarski, L. H. Dubois, *J. Phys. Chem.*, **97**, 6948 (1993).
- [214] P. D. Maniar, A. Navrotsky, *J. Non-Crys. Solids*, **120**, 20 (1990).
- [215] B. C. Bunker, D. M. Haaland, K. J. Ward, T. A. Michalske, J. S. Binkley, C. F. Melius, C. A. Balfe, *Surf. Sci.*, **210**, 406 (1989).
- [216] M. O'Keeffe, G. V. Gibbs, *J. Chem. Phys.*, **81**, 876 (1984).
- [217] M. O'Keeffe, G. V. Gibbs, *J. Phys. Chem.*, **89**, 4574 (1985).
- [218] F. Kudo, S. Nagase, *J. Am. Chem. Soc.*, **107**, 2589 (1984).
- [219] M. Yu, S. Kalvoda, M. Dolg, *Chem. Phys.*, **224**, 121 (1997).
- [220] B. Paulus, P. Fulde, H. Stoll, *Phys. Rev. B*, **54**, 2556 (1996).
- [221] D. R. Hamann, *Phys. Rev. B*, **55**, 14784 (1997).
- [222] T. Uchino, Y. Kitagawa, T. Yoko, *Phys. Rev. B*, **61**, 234 (2000).
- [223] S. T. Bromley, M. A. Zwijnenburg, Th. Maschmeyer, *Phys. Rev. Lett.*, **90**, 35502 (2003).
- [224] A. Abdurahman, A. Shukla, M. Dolg, *Phys. Rev. B*, **65**, 115106 (2002).
- [225] H. Stoll, *Phys. Rev. B*, **46**, 6700 (1991).
- [226] H. Stoll, *J. Chem. Phys.*, **97**, 8449 (1992).

- [227] B. Paulus, P. Fulde, H. Stoll, *Phys. Rev. B*, **51**, 10572 (1995).
- [228] K. Doll, M. Dolg, H. Stoll, *Phys. Rev. B*, **54**, 13529 (1996).
- [229] K. Doll, M. Dolg, P. Fulde, H. Stoll, *Phys. Rev. B*, **55**, 10282 (1997).
- [230] J. P. Perdew, Y. Wang, *Phys. Rev. B*, **45**, 13244 (1992).
- [231] W. J. Hehre, R. Ditchfield, J. A. Pople, *J. Chem. Phys.*, **56**, 2257 (1972).
- [232] M. M. Francl, W. J. Pietro, W. J. Hehre, J. S. Binkley, M. S. Gordon, D. J. DeFrees, J. A. Pople, *J. Chem. Phys.*, **77**, 3654 (1982).
- [233] M. J. O. Deegan, P. J. Knowles, *Chem. Phys. Lett.*, **227**, 321 (1994).
- [234] M. J. Fink, K. J. Haller, R. West, J. Michl, *J. Am. Chem. Soc.*, **106**, 822 (1984).
- [235] L. Levien, C. T. Previtt, D. J. Weidner, *Amer. Mineral.*, **65**, 920 (1980).
- [236] B. Civalleri, C. M. Zicovich-Wilson, P. Ugliengo, V. R. Saunders, R. Dovesi, *Chem. Phys. Lett.*, **292**, 394 (1998).
- [237] K. Doll, M. Dolg, P. Fulde, H. Stoll, *Phys. Rev. B*, **52**, 4842 (1995).
- [238] D. M. Teter, G. V. Gibbs, M. B. Boisen, D. C. Allan, M. P. Teter, *Phys. Rev. B*, **52**, 8064 (1995).
- [239] A. B. Mukhopadhyay, M. Dolg, C. Oligschleger, *J. Chem. Phys.*, **120**, 8734 (2004).
- [240] Y. Oumi, H. Yamano, M. Kubo, R. Vetrivel, A. Miyamoto, *Catal. Today*, **23**, 417 (1995).
- [241] A. Redondo., P. J. Hay, *J. Phys. Chem.*, **93**, 11754 (1993).
- [242] A. E. Alvarado-Swaisgood, M. K. Barr, P. J. Hay, A. Redondo., *J. Phys. Chem.*, **95**, 10031 (1991).
- [243] M. Sierka, J. Sauer, *J. Phys. Chem. B*, **105**, 1603 (2001).
- [244] S. Humbel, S. Sieber, K. Morokuma, *J. Chem. Phys.*, **105**, 1959 (1996).
- [245] M. Sierka, J. Sauer, *J. Chem. Phys.*, **112**, 6983 (2000).

Abstract

Results of molecular dynamics simulations on structural, vibrational and relaxational properties of zeolite ZSM-5 based amorphous solids are presented. The effects of extent of amorphization, measured by an energetic criterion, on properties like distribution of coordination numbers, internal surface area, ring statistics and effective pore size are studied. Ring statistics indicates that upon amorphization not only rings with larger size break down to give rings with smaller size, but that for intermediate degree of amorphization also larger rings are generated.

The vibrational density of states was determined for different extents of amorphization. The vibrational modes are analyzed by projecting them on those of the SiO_4 and Si-O-Si subunits and individual frequency-dependent contributions of stretching, bending and rotation are discussed. Analysis of low-frequency spectrum show that for higher crystallinity the intensity of the boson peak decreases upon amorphization, whereas the opposite behavior is observed for forms with lower crystallinity. These effects are explained in the framework of Maxwell counting of floppy modes. The modes associated with the boson peak for these materials are found to be mainly optic in nature.

Relaxations were studied for temperatures below the critical temperature. At low temperatures the relaxations comprise mainly one-dimensional chains of atoms. The dimensionality of the relaxing centers increases with the temperature due to side branching. The possibility of having reversible jumps decreases with increasing temperature due to a strong drop in the potential energy during aging. There exist very prominent peaks in the van Hove correlation functions as a manifestation of the hopping processes. The dynamics of the oxygen atoms is found to be more heterogeneous than those of the silicon atoms.

Ab initio many-body calculations on the strain energy of W-silica, taken as a model system for edge-sharing tetrahedral SiO_2 -systems with respect to corner-sharing ones as in α -quartz was performed. Correlation contributions are found to play an important role to determine the stability of edge-sharing units. Our calculation reveal that edge-sharing SiO_4 tetrahedra in (partially) amorphous silicate systems are possible at a modest energetic expense.

Kurzzusammenfassung

In der vorliegenden Arbeit werden Ergebnisse von "Molecular-Dynamics"-Simulationen an Struktur-, Schwingungs- und Relaxationseigenschaften von, auf Zeolith ZSM-5 basierenden, amorphen Festkörpern aufgezeigt. Die Effekte des Ausmaßes der Amorphisierung, welche über ein Energiekriterium festgelegt wird, werden an Eigenschaften, wie der Verteilung der Koordinationszahlen, der internen Oberfläche, der Ringstatistik und der effektiven Porengröße untersucht. Die Ringstatistik deutet darauf hin, dass sich während der Amorphisierung nicht nur große Ringe zu kleineren reduzieren, sondern dass auch auf der Zwischenstufe der Amorphisierung größere Ringe gebildet werden.

Die Zustandsdichten der Schwingungen wurden für verschiedene Ausmaße der Amorphisierung bestimmt. Die Schwingungsmoden wurden analysiert, indem sie auf jene der SiO_4 und Si-O-Si Untereinheiten projiziert wurden. Desweiteren werden individuelle, frequenzabhängige Beiträge der Streckung, Beugung und Rotation diskutiert. Analysen von niedrig-frequenten Spektren zeigen, dass bei höherer Kristallinität die Intensität des Boson-Peaks mit der Amorphisierung abnimmt, während das gegensätzliche Verhalten bei Formen mit niedrigerer Kristallinität zu beobachten ist. Diese Effekte werden im Rahmen von Maxwells Zählung der schwachen Moden erklärt. Es stellte sich heraus, dass die Moden, die mit dem Boson-Peak assoziiert sind, hauptsächlich optischer Natur sind.

Relaxationen wurden für Temperaturen unterhalb der kritischen Temperatur untersucht. Bei niedrigen Temperaturen umfassen die Relaxationen hauptsächlich eindimensionale Atomketten. Die Dimensionalität der Relaxationszentren steigt mit der Temperatur aufgrund von Seitenverknüpfungen an. Die Möglichkeit des Auftretens von reversiblen Sprüngen nimmt mit zunehmender Temperatur aufgrund eines starken Abfalls der potentiellen Energie während des Alterns ab. Es existieren sehr auffallende Peaks in den van Hove Korrelationsfunktionen als Beweis für den Sprungprozeß. Es konnte gezeigt werden, dass die Dynamik der Sauerstoffatome heterogener ist als die der Siliciumatome.

Es wurden ab initio "many-body" Berechnungen der Spannungsenergie von W-Silica, welches als Modellsystem für kanten- verknüpfte tetraedrische SiO_2 -Systeme hinsichtlich ecken-verknüpfter (wie im α -Quarz) benutzt wurde, durchgeführt. Es stellte sich heraus, dass die Korrelationsbeiträge eine wichtige Rolle bei der Bestimmung der Stabilität von kanten-verknüpften Einheiten spielen. Die während dieser

Arbeit durchgeführten Berechnungen zeigen, dass kanten-verknüpfte SiO_4 -Tetraeder in (teilweise) amorphen SiO_4 -Systemen schon mit einem geringen energetischen Aufwand erhalten werden können.

List of Publications

1. A. B. Mukhopadhyay, C. Oligschleger, M. Dolg,
Molecular dynamics investigation of structural properties of a zeolite ZSM-5 based amorphous material,
Physical Review B, **67**, 014106-1 - 014106-11 (2003).
2. A. B. Mukhopadhyay, C. Oligschleger, M. Dolg,
Molecular dynamics investigation of vibrational properties of zeolite ZSM-5 based amorphous material,
Physical Review B, **68**, 024205-1 - 024205-10 (2003).
3. A. B. Mukhopadhyay, C. Oligschleger, M. Dolg,
Low-frequency vibrational excitations in zeolite ZSM-5 and its partially crystalline derivatives,
Physical Review B, **69**, 012202-1 - 012202-4 (2004).
4. A. B. Mukhopadhyay, M. Dolg, C. Oligschleger,
Ab initio many-body investigation of structure and stability of two-fold rings in silicates,
The Journal of Chemical Physics, **120**, 8734-8739 (2004).
5. A. B. Mukhopadhyay, C. Oligschleger, M. Dolg,
Molecular dynamics investigation of relaxations in zeolite ZSM-5 based amorphous material,
Manuscript submitted.
6. A. B. Mukhopadhyay, C. Oligschleger, M. Dolg,
Static and dynamic properties of amorphous material derived from zeolite ZSM-5,
Accepted in *Journal of Non-Crystalline Solids* as a proceedings in CONCIM 2003.

Lebenslauf

Name:	Atashi Basu Mukhopadhyay
Geburtstag:	31.05.1975
Geburtsort:	Kanchrapara, Indien
Familiensand:	Verheiratet

Ausbildung:	
Promotion:	Von Sommer Semester 2001- Oct. 2004 Institut für Theoretische Chemie, Universität zu Köln, Deutschland
Betreuer:	Prof. Dr. M. Dolg
Titel meiner Dissertation:	" <i>Theoretical Investigation of Static and Dynamic Properties of Zeolite ZSM-5 Based Amorphous Material</i> "

Junior Research Fellow:	Jan. 2000- Mar. 2001 National Chemical Laboratory, Pune, India
----------------------------	--

Post Graduate Teacher:	June 1998- Dec. 1999 M.C.M. D.A.V. Centenary Public School, Pathankot, India
---------------------------	--

M.Sc. (Diplom):	1996 -1998 Department of Chemistry, Pondicherry Central University, India
Betreuer:	Dr. G. N. Sastry
Titel meiner Diplom Arbeit:	" <i>Parameters Controlling the Electron Transfer and Substitution Reactivities between Anion Radicals and Alkyl Halides. A Semi-Empirical SCF Study</i> "

B.Sc. Ed:	1992-1996 (4-year integrated course) Bachelor of Science and Education, Regional Institute of Education, Mysore University, India
-----------	--

Erklärung

Ich versichere, dass ich die von mir vorgelegte Dissertation selbstständig angefertigt, die benutzten Quellen und Hilfsmittel vollständig angegeben und die Stellen der Arbeit - einschließlich Tabellen, Karten und Abbildungen -, die anderen Werken im Wortlaut oder dem Sinn nach entnommen sind, in jedem Einzelfall als Entlehnung kenntlich gemacht habe; dass diese Dissertation noch keiner anderen Fakultät oder Universität zur Prüfung vorgelegen hat; dass sie - abgesehen von unten angegebenen Teilpublikationen - noch nicht veröffentlicht worden ist sowie, dass ich eine solche Veröffentlichung vor Abschluss des Promotionsverfahrens nicht vornehmen werde. Die Bestimmungen dieser Promotionsordnung sind mir bekannt. Die von mir vorgelegte Dissertation ist von Prof. Dr. M. Dolg betreut worden.

Köln, den 26.4.2004

